Doctoral Thesis

Thermodynamic and kinetic modification for $LiBH_4$ and its composite with MgH_2

（$LiBH_4$ および MgH_2 との複合化材料の熱力学的および動力学的改良）

Mechanical Science and Engineering
Graduate School of Engineering
Hiroshima University
September 2020

Pratibha Pal

This thesis is dedicated to my father for his unconditional love, support and patient.

Acknowledgment

Firstly, I would like to thank Almighty God, for giving me strength and power in my doctoral course life.

I am blessed to work and would like to express my sincere gratitude to my supervisor **Prof. Dr. Takayuki Ichikawa** for his guidance, timely support, suggestions and encouragements throughout the doctoral life. I am blessed to do work under his supervision. He is not only an outstanding supervisor, a great team leader but also a kind human being.

I would also like to express my special thanks to **Assoc. Prof. Dr. Ankur Jain** for his continuous support beyond the limits and guidance throughout my doctoral course. I am pleased to have him as a mentor who knows how to mold raw clay and morph into meaningful thing from it. He always demonstrated a positive attitude and acts as a catalyst for me not only in professional career but in personal as well.

I want to express my sincere thanks to **Prof. Dr. Yoshitsugu Kojima** for his valuable suggestions during my work and a lot of interesting talks at diverse topics. I am also thankful to **Assoc. Prof. Dr. Hiroki Miyaoka** for his valuable time for discussion, suggestions, constructive criticism, and support throughout the work.

I am also thankful to Dr. Tengfei Zhang, Dr. Jean Pierre Bonnet for their valuable and critical discussions time to time which worked for me a source of encouragement.

I wish to express my sincere gratitude to Assist. Prof. Rini Singh and Assist. Prof. Kana Machi for their kind support in my doctoral course life.

I express my heartiest thanks to my seniors and colleagues - Mr. Tomoyuki Ichikawa, Dr. Rajesh Jangir, Dr. Suganthamalar Selvaraj, Dr. Keita Nakajima, Mr. Hironori Kawai, Ms. Guo Fangqin, Mr. Keita Shinzato, Mr. Fernando Cano Banda, Mr. Hiroyuki Gi, who made this journey really interesting and helped me in all ways.

I would like to express my special thanks to Ms. Misao Mukouda, Ms. Saori Inagaki and Ms. Hikaru Yamamoto for their kind support in my doctoral course life.

It is my privilege to acknowledge all the faculty members and staff of Faculty of engineering,

Hiroshima University for their continuous support and kind availability at all the time.

I am also thankful to my colleagues and friends Dr. Pooja Kumari (Research Fellow, University of Birmingham), Dr. Bulbul Jha, Ms. Khushboo Sharma (MNIT, Jaipur), for their co-operation and making this journey memorable. A special thanks to Dr. Amol Singh (NSRRC Hsinchu, Taiwan), Mr. Jignesh Patel for always being with me in all situations and to give me a lot of moral support during this journey.

I am very thankful to Assist. Prof. Dr. Shiv Kumar (Hiroshima synchrotron center, Hiroshima University), without whom I couldn’t be able to find such a wonderful PhD group and guide.

My deepest sense of gratitude goes to my parents and my family who always stood by me during hard times, who taught me basic lessons of gratitude and bringing me up by moral lessons, with which I become a scholar and decent human being. I take this opportunity to thank all those whose name may not be mentioned here but who supported me at different point of times through their wishes, blessings and kindness.

Last but not the least, I would like to thanks to my boyfriend Dr. Dayanand Kumar (Research scholar, NTU Singapore) for his constant encouragement and patient. He has always been a great source of motivation and his support in many ways cannot be expressed in words.

Abstract

The present study was focused on to lower the decomposition temperature of $LiBH_4$ and its composite system $2LiBH_4$-MgH_2 by tuning their thermodynamics and kinetics. According to the issues associated with $LiBH_4$ (hard thermodynamics) and $2LiBH_4$-MgH_2 (sluggish kinetics), the thesis was structured with two objectives.

First objective was to focus on the $2LiBH_4$-MgH_2 composite, where the thermodynamics of $LiBH_4$ was modified by the addition of MgH_2 but this composite system possess serious kinetic issues. In this work, KH was added as catalyst to the $2LiBH_4$-MgH_2 system in order to enhance the kinetics. A reduction in the temperature was observed for the first hydrogen desorption reaction, but no effect could be seen in the second dehydrogenation. However, an interesting phenomenon of eutectic melting was observed during the thermal heating of this system. By addition of 5 mol% KH, the melting point was shifted to lower temperature, which was continuously decreased with increase in the amount of KH from 0 to 55 mol%. For 55 mol% KH i.e. at eutectic composition $0.45(2LiBH_4$-$MgH_2)$-$0.55KH$ the lowest melting temperature was observed as *79°C*. Eutectic melting is an interesting phenomenon and happens if two or more components sustain their liquid state below the melting points of their pure components. In this work, kinetic enhancement was achieved due to the occurrence of eutectic melting on adding KH as additive. The enhanced ionic mobility must be the driving force to desorb hydrogen at lower temperature in comparison of $2LiBH_4$-MgH_2 composite, thus caused a kinetic enhancement on addition of KH. Reduced melting point for some complex hydrogen storage systems behaves as eutectic melts and can be utilized for refueling of vehicles. A pseudo-binary phase diagram between the $2LiBH_4$-MgH_2 composite

and KH was discussed and was explained in terms of degree of freedom.

The second objective of the thesis was to modify the thermodynamics of pure $LiBH_4$ by the addition of Bi_2X_3 chalcogenides and study their decomposition properties. This work was initiated with a curiosity during an electrochemical experiment on Bi_2X_3 chalcogenides as anode materials for all-solid-state Li-ion battery in a recent work by our group. $LiBH_4$ was used as solid electrolyte in the cell with Bi_2Te_3 nanostructures as anode material. An interesting issue of cell opening during the charging – discharging motivated us to investigate the effect of Bi_2X_3 (X = S, Se and Te) addition on the decomposition properties of $LiBH_4$. An efficient destabilization of $LiBH_4$ could be achieved by addition of chalcogenides (Bi_2S_3, Bi_2Se_3 and Bi_2Te_3), which could tune the thermodynamic properties of $LiBH_4$ decomposition by alloying with Li. The hydrogen desorption temperature of $LiBH_4$ was reduced to below 150 ℃ by the addition of bulk Bi_2X_3. The detailed mechanism was established for the reaction of $LiBH_4$ with the Bi_2Te_3 (similar reaction steps were found for other two composites as well, i.e. $LiBH_4$-50wt%Bi_2Se_3 and LiBH4-50wt%Bi_2S_3) using several techniques and was proposed as follows:

$$38\mathrm{LiBH_4} + \mathrm{Bi_2}Te_3 \rightarrow \mathrm{Li_2}Te + 25\mathrm{LiBH_4} + 7LiH + 2\mathrm{Bi} + 12B + 22.5\mathrm{H_2}$$

$$\rightarrow 2\mathrm{Li_3Bi} + 17\mathrm{LiBH_4} + 2LiH + 8B + 15\mathrm{H_2}$$

$$\rightarrow 13\mathrm{LiH} + 4\mathrm{Li} + 17\mathrm{B} + 27.5\mathrm{H_2}$$

A further reduction in the decomposition temperature was achieved using nanostructured Bi_2X_3, which must be due to kinetic enhancement due to better solid-solid contact between $LiBH_4$ and Bi_2X_3 that promotes a faster reaction between the components.

All the work was compiled in Chapter 1 to 6. Chapter 1, describes the introduction of the field, need of research and associated challenges. Based on the background discussed in chapter 1, the objectives are described in chapter 2, which comprises the aim of the thesis and motivation behind the research work. All the methods and materials adopted for the preparation as well as characterization of composite materials used in this work are covered in chapter 3. Chapter 4 is the explanation of our first objective i.e. improving the kinetics of $2LiBH_4$-MgH_2 system by the addition of potassium hydride (KH) as a catalyst. The results on the destabilization of $LiBH_4$ by the infusion of Bi_2X_3 (X = S, Se, Te) are presented in chapter 5. At last, chapter 6 summarize the results and suggest overall conclusion of the thesis and propose the future direction of research.

Table of Contents

Chapter-1: Introduction 1

1-1 Hydrogen as Energy Carrier 1

1-2 Properties of Hydrogen 3

1-2-1 Hydrogen Isotopes 3

1-2-2 Hydrogen Molecule 3

1-2-3 Equation of State 4

1-3 Hydrogen Storage 5

1-3-1 Storing hydrogen as a gas 6

1-3-2 Liquid hydrogen 7

1-3-3 Hydrogen Storage in Solid-State Materials 7

1-4 Interaction of Hydrogen with Solids 8

1-4-1 Thermodynamics of Hydrogen Absorption/Desorption 10

1-4-2 Kinetics of hydrogen absorption and desorption 12

1-5 How to tune thermodynamics and kinetics of hydrogen absorption /desorption 15

1-5-1 Thermodynamic Alteration 15

1-5-2 Kinetic Alteration 16

KH as excellent catalyst for metal hydrogen system 16

1-6 Solid state hydrogen storage materials 18

1-6-1 Metal hydrides 20

1-6-2 Complex hydride 20

1-7 $LiBH_4$ as promising material for hydrogen storage 22

1-8 $2LiBH_4$ - MgH_2 System...23

1-9 $LiBH_4$ as solid electrolyte and its use for Bi_2X_3 anode materials in all-solid-state Li-ion battery...26

Chapter-2: Purpose of thesis.. 39

Chapter-3: Materials and Methods.. 42

3-1 Sample preparation 42

3-1-1 Materials 42

3-1-2 Mechanical ball milling method...42

3-1-3 Synthesis of nanostructures..44

3-2 Characterization techniques...46

3-2-1 X-ray Diffraction Spectroscopy (XRD)..46

3-2-2 Thermal analysis for gas desorption 48

3-2-2-1 Thermogravimetry – Differential thermal analysis (TG-DTA).....48

3-2-2-2 Thermal Desorption Mass Spectroscopy (TDMS)........................49

3-2-2-3 Differential scanning calorimetry (DSC) 50

3-2-4 Transmission Electron Microscopy (TEM).....................................51

3-2-5 Scanning Electron Microscopy (SEM) 52

Chapter-4: Improveming the kinetics of 2LiBH4-MgH2 system by the addition of potassium hydride (KH) as a catalyst...................................... 70

4-1 Introduction..70

4-2 Effect of 5 mol% KH addition on the $2LiBH_4$-MgH_2 system 71

4-3 Effect of varying KH content on the $2LiBH_4$-MgH_2 system 73

4-4 Phase diagram of x($2LiBH_4$-MgH_2) - (1-x)KH system 74

4-5 Structural observations after milling and heating 75

4-6 Summary 76

Chapter-5: Destabilization of LiBH4 by the infusion of Bi2X3 (X = S, Se, Te): Structural and Morphological Investigation 84

5-1 Introduction...84

5-2 Dehydrogenation of $LiBH_4$ – bulk Bi_2X_3 composites...........................84

5-3 Nanostructures characterizations: SEM and TEM analysis...............86

5-4 Effect of nanostructured Bi_2X_3 on decomposition properties of $LiBH_4$ 87

5-5 XRD analysis of $LiBH_4$ – 50wt% Bi_2X_3 composites at different decomposition steps 88

5-6 In-situ TEM observation of $LiBH_4$-nano Bi_2X_3 composites.................91

5-7 Discussion and reaction mechanism establishment.............................93

5-8 Summary 96

Chapter-6: Conclusions and Future work 117

References 119

List of Figures

Figure 1-1: Energy consumption in between 2018-2050 28

Figure 1-2: Schematic representation of hydrogen or protium (H), deuterium (D) and tritium 29

Figure 1-3: Ortho and para hydrogen 30

Figure 1-4: (T)Phase diagram of hydrogen; liquid hydrogen only exists between the solidus line and the line from the triple point at 21.2 K and the critical point at 32 K 31

Figure 1-5: Potential energy diagram for interaction of hydrogen with metal surfaces 32

Figure 1-6: Pressure–Composition–Temperature diagram (PCT isotherms). Inset: van't Hoff plot 33

Figure 1-7: Energy barrier for hydrogen adsorption and desorption 34

Figure 1-8: Diffusion coefficients of hydrogen isotopes in some bcc metals 35

Figure 1-9: Temperature dependences of H_2 and NH_3 release from the potassium-modified (—) and the pristine samples (- - - -) 36

Figure 1-10: Free energy per mol of H_2 as a function of temperature and the standard enthalpy of a reaction of the hydride system $2LiBH_4 + MgH_2$ 37

Figure 1-11: Schematic of destabilization process of a hydride MH using third element A 38

Figure 3-1: Rotating (planetary) ball mill 54

Figure 3-2: Schematic for the synthesis of Bi_2S_3 nanoflowers 55

Figure 3-3: Schematic for the synthesis of Bi_2Se_3 nanoflowers 56

Figure 3-4: Schematic for the synthesis of Bi_2Te_3 nanoflowers 57

Figure 3-5: Diffraction of X-ray from lattice planes in crystal 58

Figure 3-6: Picture of Rigaku-RINT 2500 XRD equipment 59

Figure 3-7: Sample for XRD measurement 59

Figure 3-8: Schematic of TG-DTA apparatus 60

Figure 3-9: (a) Rigaku, TG8120 connected to a mass spectrometer (MS, Anelva, M-QA200TS) glove box, (b) TG-DTA instrument inside the glove box 61

Figure 3-10: Schematic of heat flux type DSC apparatus 62

Figure 3-11: Image of Q10 PDSC, TA instruments DSC apparatus 63

Figure 3-12: Generated signals when a high-energy beam of electrons interacts with a thin specimen 64

Figure 3-13: (a) Left: bright-field (BF) mode. (b) Right: “dirty” dark-field (d-DF) mode 65

Figure 3-14: Interactions between electrons and a sample 66

Figure 3-15: Emission of secondary electron, backscattered electron and characteristic X-ray 67

Figure 3-16: Schematic diagram of a scanning electron microscope 68

Figure 3-17: Images of the SEM instrument JEOL JSM 6380 (left); other two images belongs to transfer stick and sample stage 69

Figure 4-1: DTA (upper panel) and TG analysis (lower panel) of $2LiBH_4$-MgH_2 (dashed lines) and $2LiBH_4$-MgH_2 - 5%KH (solid lines) 77

Figure 4-2: DSC profile of pure $LiBH_4$-MgH_2 (green color) and on the addition of 5 mol% KH in $LiBH_4$-MgH_2 78

Figure 4-3: DSC curves for pure $2LiBH_4$-MgH_2 (first from upwards) and remaining with the increasing percentage of potassium hydride 79

Figure 4-4: DSC profiles of selected samples 80

Figure 4-5: Phase diagram of x($2LiBH_4$-MgH_2)-(1-x)KH system 81

Figure 4-6: XRD patterns of selected samples after milling 82

Figure 4-7: XRD patterns of selected samples after heating 83

Figure 5-1: TG-DTA and MS profile of milled (a) $LiBH_4$ – 50wt% bulk Bi_2S_3 97

Figure 5-2: TG-DTA and MS profile of milled (b) $LiBH_4$ – 50wt% bulk Bi_2Se_3 98

Figure 5-3: TG-DTA and MS profile of milled (c) $LiBH_4$ – 50wt% bulk Bi_2Te_3 99

Figure 5-4: FE-SEM & TEM images of Bi_2S_3 nanoflowers (a & b), SAED & HRTEM images of nanoflowers (c & d) 100

Figure 5-5: TEM & FE-SEM images of Bi_2Se_3 nanosheets (a & b), SAED & HRTEM images of Bi_2Se_3 nanosheets (c & d) 101

Figure 5-6: FE-SEM & TEM images of Bi_2Te_3 nanosheets (a & b), SAED & HRTEM images of Bi_2Te_3 nanosheets (c & d) 102

Figure 5-7: (a) TG and (b) MS profiles of milled samples; (i) $LiBH_4$ – 50 wt% Bi_2S_3 nanoflowers (ii) $LiBH_4$ – 50 wt% Bi_2Se_3 nanosheets (iii) $LiBH_4$– 50 wt% Bi_2Te_3 nanosheets 103

Figure 5-7: (c) and (d) are MS profile for the comparison of nanostructures and bulk Bi_2X_3 samples mixed $LiBH_4$ for dehydrogenation properties 104

Figure 5-7: (e) is MS profile for the comparison of nanostructures and bulk Bi_2X_3 samples mixed $LiBH_4$ for dehydrogenation properties 105

Figure 5-8: XRD profile of samples after heated to various temperatures with the same heating rate (a) $LiBH_4$ – 50 wt% bulk Bi_2S_3 106

Figure 5-9: XRD profile of samples after heated to various temperatures with the same heating rate (b) $LiBH_4$ – 50 wt% bulk Bi_2Se_3 107

Figure 5-10: XRD profile of samples after heated to various temperatures with the same heating rate (c) $LiBH_4$-50 wt% bulk Bi_2Te_3 108

Figure 5-11: DTA profile of $LiBH_4$-50wt% Bi_2S_3 composite with heating (downwards; endo) and cooling (upwards; exo) profiles 109

Figure 5-12: TG-DTA and MS profile of $12LiBH_4$- Bi_2S_3 sample 110

Figure 5-13: TEM images (associated SADP) of $LiBH_4$ - 50% Bi_2S_3 nanostructures (a) after milling at room temperature (b) after heating at 50℃ (c) after heating at 100℃ (d) after heating at 150℃ (e) after heating at 200℃(Image a to image e, measurements are on spot 1) 111

Figure 5-14: TEM Micrograph of $LiBH_4$-50% Bi_2S_3 composite after milling and heating at different temperatures. EDS profile was obtained from the position shown by the start point of arrow 112

Figure 5-15: TEM images (associated SADP) of (a) $LiBH_4$ - 50% Bi_2Se_3 nanostructures at room temperature on spot 1 (b) $LiBH_4$ - 50% Bi_2Se_3 nanostructures at room temperature after heating on spot 2 113

Figure 5-16: TEM Micrograph of $LiBH_4$-50% Bi_2Se_3 composite after milling and heating at 450°C. EDS profile was obtained from the position shown by the start point of arrow 114

Figure 5-17: TEM images (associated SADP) of (a) $LiBH_4$ - 50% Bi_2Te_3 nanostructures at room temperature on spot 1 (b) $LiBH_4$ - 50% Bi_2Te_3 nanostructures at room temperature after heating on spot 2 115

Figure 5-18: TEM Micrograph of $LiBH_4$-50% Bi_2Te_3 composite after milling and heating at different temperatures. EDS profile was obtained from the position shown by the start point of arrow 116

Chapter-1

Introduction

1-1 Hydrogen as Energy Carrier

World's energy consumption has been increasing continuously from past several years. The highest energy consumption comes from the developing countries e.g. China attained an annual growth rate of 3.7% in energy consumption since 2012. Not only the developing countries, but also the developed countries are not far behind to consume energy. As an example, United States was placed on second position in terms of energy consumption which reached to a high record 2.3 Gtoe (giga tonne of oil equivalent) in 2018, up 3.5% from 2017 [1]. According to International Energy Outlook 2019, the U.S. Energy Information Administration (EIA) predicted that world energy expenditure will increase by approx. 50% between 2018 and 2050, see fig. 1-1 [2]. In the last century the population has raised by a factor of six, whereas consumption of energy has risen by a factor of 80 [3].

More than 1.0×10^{14} kWh/year (80%) energy needs are being fulfilled by fossil fuels like petroleum, coal, and natural gas. Our dependency on fossil fuels and depleting sources of fossil fuels are the serious problems of concern. In addition, harmful green-house gases such as carbon dioxide (CO_2) and nitrogen oxide (NO_x) are increasing in the environment due to excess use of fossil fuels. To reduce CO_2 emission from environment we need to develop an ecofriendly fuel which can be used in zero emission vehicles or thermal power plant. Renewable energy sources are the best alternative of the conventional fossil fuels which can reduce our dependency on fossil fuels. Renewable energy sources such as solar, wind, hydroelectric, ocean energy and hydrogen energy are environment friendly, which can be the possible solutions of above-mentioned issues. However, the renewable energy sources fluctuate and depend on the places. Hydrogen is necessary to make a balance between supply and demand which is well-known as energy carrier in today's world due to the following features:

1. Hydrogen is one of the most abundant elements on the planet; but unfortunately, only less than 1% is available in molecular form, the immense part is chemically bound in form of water (H_2O) and some of it is bound as volatile hydrocarbons.
2. The hydrogen atom is enticing because it consists of a proton and an electron, i.e. unlike other elements of periodic table, hydrogen has the maximum ratio of number of valence electrons to the protons (and neutrons). In case of hydrogen, the energy gain per electron is 13.6 eV that is too high. The chemical energy per mass of hydrogen (39.4 $\text{kWh}\cdot\text{kg}^{-1}$) is three times greater than that of other chemical fuels, e.g. liquid hydrocarbons (13.1 $\text{kWh}\cdot\text{kg}^{-1}$). This means - the energy content of 0.33 kg of hydrogen can be compared with the energy content of 1 kg of oil [4].
3. The production of hydrogen is simple by using primary energy sources like solar power, hydroelectric, wind power and ocean energy without emitting any pollutants like CO_2 at the time of fossil fuel combustion or usage.
4. Hydrogen is the energy carrier not the primary source of energy, it can be converted as electric energy by using fuel cell. No pollutants are emitted from hydrogen while using in fuel cell, water is the only product from fuel cell. Hydrogen can be used directly in internal combustion (IC) engines as well.

1-2 Properties of Hydrogen

1-2-1 Hydrogen Isotopes

Hydrogen, the first element of periodic table, has the atomic number 1 and the electron configuration $1s^1$. Fig. 1-2 shows the schematic representation of hydrogen isotopes. Red color shows proton associated with blue color neutron inside the nucleus and black colored electron moving around the nucleus. Isotopes of hydrogen are classified as *protium (H)*, *Deuterium (D)* and *Tritium (T)*. *Protium (H)* has an atomic weight of 1.0078 (1 proton and 1 electron). In 1932, Urey came across with the preparation of *Deuterium (D)* a stable isotope, with 2.0140 atomic weight (1 proton, 1 neutron and 1 electron). Tritium was discovered after two years as an unstable isotope with an atomic weight of 3.0161 (1 proton, 2 neutrons and 1 electron) [5].

1-2-2 Hydrogen Molecule

A hydrogen molecule holds two atoms with spinning nuclei of both the atoms. Ortho and Para are recognized as the two types of hydrogen, classified on the basis of spin of the nuclei.

The molecule having spin of both nuclei in the same direction are termed as ortho hydrogen molecules whereas, the inverse direction of spin of both nuclei represent the para hydrogen, see Fig. 1-3. The amount of both type of hydrogen is dependent on temperature:

- At 20 K, hydrogen contains more stable form i.e. predominantly para (singlet) hydrogen (99.8%).
- The ratio of ortho and para hydrogen is 1:1 at the liquified temperature of air (~80K).
- At 25°C (room temperature), the ratio of ortho to para hydrogen is 3:1.

- Even at elevated temperatures, the ratio of ortho to para hydrogen cannot be exceeded than 3:1.

1-2-3 Equation of State

An equation which relates the pressure, temperature, and density of a substance is called the equation of state. The equation of state (EOS), defines the essential thermodynamic properties of hydrogen i.e., pressure and temperature which are the functional parameters of the volume V (p, T). The Gibbs energy G (p, T) and entropy S (p, T) can be acquired by integration [6]:

$$G(p, T) = G(p_0, T) + \int_{p_0}^{p} V\,dp \;\ldots\ldots\ldots\ldots(1\text{-}1)$$

$$S(p, T) = S(p_0, T) - \int_{p_0}^{p} \left(\frac{\partial V}{\partial T}\right)_p dp \;\ldots\ldots\ldots\ldots(1\text{-}2)$$

By substituting ideal-gas values for G (p_0,T) and S (p_0,T) for the reference isobar (p_0 =0 .1MPa), other thermodynamic quantities can be estimated.

The enthalpy is expressed by:

$$H(p, T) = G(p, T) + TS(p, T) \;\ldots\ldots\ldots\ldots(1\text{-}3)$$

at low gas density, a real gas tends to act like an ideal gas and follows the ideal gas law:

$$p \cdot V = n \cdot R \cdot T \;\ldots\ldots\ldots\ldots\ldots\ldots\ldots\ldots(1\text{-}4)$$

where, p is the absolute pressure, V the volume, n belongs to the number of gas molecules and R is the gas constant (8.314Jmol^{-1} K^{-1}). In case of a real gas, however, the gas molecules hold a certain volume – the “excluded volume” b – and the molecules are bound by Van der Waals force (dipole interaction), which is expressed by the interaction strength a. Therefore, for model gases Van der Waals equation is written as:

$$(p + \frac{a.(n^2)}{V^2})\ \{V\text{-}b(n)\} = n\cdot R\cdot T\ldots\ldots(1\text{-}5)$$

where, $a(H_2) = 2.476\times10^{-2}$ m^6 Pa mol^{-2} and $b(H_2) = 2.661\times10^{-5}$ m^3 mol^{-1}

The pressure as a function of the volume for a model gas is formulated as [6],[7]:

$$p\,(V) = \frac{n.R.T}{V-n.b} - a.\frac{n^2}{V^2}\quad\ldots\ldots\ldots\ldots\ (1\text{-}6)$$

All the thermodynamic quantities can be obtained once the EOS is known [7].

There are several aspects which are needed to address in order to establish hydrogen economy. Efficient hydrogen storage is one of these issues. The next section describes the various storage methods of hydrogen.

1-3 Hydrogen Storage

Hydrogen storage is an important issue to consider while accounting the hydrogen as fuel. The energy density of hydrogen [120 (LHV)-142 (HHV) MJ/kg] is almost 3 times of the conventional fuels (natural gas: 43 MJ/kg and gasoline 44.4 MJ/kg). Less volumetric density of hydrogen is the main issue of storage. The volumetric energy density of liquid hydrogen (8.4 MJ/L) is less than half that of the other conventional fuels (natural gas 17.8 MJ/L, gasoline 31.1 MJ/L) [8]. The target of hydrogen storage is to scale down the huge volume of hydrogen gas i.e. to pack hydrogen as closely as possible. For this purpose, the volumetric density should be highest by using smallest amount of storing material. Fig. 1-4 shows the phase diagram of the hydrogen molecule H_2. At lower temperatures (at 11K), hydrogen is a solid with a density of 70.6 kg·m^{-3}, and at higher temperatures (at 273K) it is a gas with a density of 0.089886 kg·m^{-3} at atmospheric pressure. Hydrogen is in liquid form in a small zone between the triple and critical points with a density of 70.8 kg·m^{-3} at 20K. To get high density of hydrogen, several works have been accomplished to compress the gas and reduce the temperature under the critical point. Following factors should be kept in mind when planning to compact hydrogen: ease of technology, choice of material, refueling time, handling, cost, safety aspects, high gravimetric and volumetric density at ambient temperature and atmospheric pressure [9],[10],[11]. DOE targets for hydrogen storage materials for onboard vehicles has been proposed time to time [12]. There is plenty of hope because of the space shuttle program where hydrogen was used successfully by NASA [8]. Continuous efforts have been carried out by several government agencies, non-profitable organizations and academicians. Several methods have been investigated by researchers and scientists across the world to store hydrogen for onboard use [9],[10],[11],[13].

1-3-1 Storing hydrogen as a gas

Storing hydrogen in molecular form is possible, only in gas or liquid form. Storing hydrogen under pressure is an oldest technique and has been used for many years. At present, gaseous pressure vessels are the most common way to store hydrogen. Pressure vessels are used for onboard hydrogen storage, commercially in FCV's as Toyota Mirai and the Honda Clarity. There are several reasons related to properties of materials and the operating costs, due to which hydrogen gas are not stored in bulk at pressures more than 15-20 MPa. Due to the limitations of storage pressure, the available density of hydrogen is also limited i.e. 7.8 kg/m^3 at 10 MPa and 20°C. Small density of hydrogen means an enormous storage specific volume and thus, a massive speculated cost. The first fuel cell vehicle utilized on board storage vessel with 70 MPa pressure, but the overall cost was high due to the maintenance of high pressure and the use of high-quality materials, like carbon fiber. Consequently, the use of these high pressure vessels are not contemplated feasible for large stationary usage [14],[15]. Apart from the large salt cavity storages underground, the search of some other alternative storage become necessity due to unavailability of geological sights everywhere across the world. One such alternative is to store hydrogen in a metal container. Corrosion is another main issue when storage system is underground thus special coating is needed against corrosion which is itself a task with high cost [14],[16].

1-3-2 Liquid hydrogen

There is conventional hydrogen liquefaction process which follows the three steps: compression, cooling and expansion. Hydrogen has extremely low boiling point (−253°C at 0.1 MPa) and hydrogen in gaseous form doesn't cool down throughout the throttling operation (i.e., adiabatic, isenthalpic expansion) for temperatures more than around −73°C. We need liquid nitrogen evaporation for precooling in the process of liquefaction. The first liquefaction of hydrogen was reported by Sir James Dewar in 1898 [17]. High cost of liquefaction is an important factor to be noted. Liquid hydrogen storage offers almost double capacity if we compare with the gaseous hydrogen storage, but the volumetric capacity is less for onboard vehicles according to the target of DOE. At present, the largest liquefaction plant capacity in US is about 70,000 kg/day and the smallest liquefaction plant has a capacity of about 6,000 kg/day [18].

1-3-3 Hydrogen Storage in Solid-State Materials

Apart from gas and liquid storage techniques here is an interesting technique to store hydrogen that is to store in solid state materials (intermetallic and complex hydrides). There is no chance of over pressure which is dangerous in case of compressed hydrogen storage, no need of extensive energy that is required for liquid hydrogen and moreover, this technology is associated with large volumetric capacities. This is the safest technique because of relatively low operating pressures [19]. Scientists in this field, focused towards this third potential solution for hydrogen storage. Several metals have capabilities due to their specific properties that can help to absorb hydrogen in their metal lattice. Hydrogen storage materials can be classified according to physisorption and chemisorption properties. If hydrogen is stored as physically (by weak van der waals forces) bounded hydrogen on to a metal surface, it is known as physiosorbed. On the other hand, if hydrogen is bound chemically on the metal surface (e.g. metal hydride and complex hydride), it is known as chemisorbed hydrogen and can be released by heating at certain temperature. The next section describes the details about interaction of hydrogen with solid-state materials as well as their thermodynamic and kinetic aspects.

1-4 Interaction of Hydrogen with Solids

Molecular or atomic hydrogen interacts with the surface layer of the host metal and make a solid solution and metal hydrides by the process of adsorption/absorption. A metal–hydrogen reaction can be written as eq 1-7:

$$M + \frac{x}{2} H_2 \rightarrow MH_x \text{............(1-7)}$$

Hydrogen interaction with the metal surface can be understood by the potential energy diagram as shown in Fig. 1-5. Far from the metal surface the molecular hydrogen and atomic hydrogen are set apart by the heat of dissociation E_D = 218 kJmol^{-1} H (4.746eV). The potential energy curve for hydrogen approaching a solid surface typically shows two energy minima with different depths; one at greater distance from the metal adsorbent (E_{PHYS} = -5 kJ/mol H) corresponds to physical adsorption (shown as dotted line) and the other at smaller distances (E_{CHEM} = -50 kJ/mol H) corresponds to chemisorption (shown as solid line). The first minima appear due to two different interactions when molecular hydrogen (gas) approaching to metal surface. The first interaction is attractive interaction i.e. weak Van der Waals force, while the other is repulsive terms, resulting into a shallow minimum at a distance of approx. 1 molecular distance of hydrogen. In physisorption the gas is adsorbed to the metal surface in its molecular state and not in atomic form. As we already discussed the attraction is due to weak forces in physisorption thus it normally occurs at low temperatures. Since there is no existence of activation energy barrier in physisorption, the process doesn't have the kinetic issues. When hydrogen reach closer to the surface, the adsorbed hydrogen molecule dissociates in atomic state at the metal surface by transferring an electron between the metal and hydrogen and becomes chemisorbed. In this process, hydrogen molecule needs to cross an activation barrier for dissociation which depends on the material properties. If there are no activation energy barriers between the hydrogen molecule and material surface, the molecule proceeds towards the surface without any trouble and dissociates into metal atoms straight forward. On the other hand, if the activation energy is high, the reactants need to be activated, either by heating or by adding some additives which can work as catalyst for the reaction. For the dissociation of H–H bond, the total energy needed is, the energy required to form metal hydride i.e. ΔH_{M-H} and activation energy i.e. E_A. Usually, at high temperature if the barrier is higher and the potential well is smaller then, less stable hydride will be formulated. On the other hand, in case of small activation barrier and deep potential well, a stable hydride will form with fast kinetics [20],[21],[22].

1-4-1 Thermodynamics of Hydrogen Absorption/Desorption

The thermodynamic features can be explained by Pressure–Composition isotherms (PCI) at different temperatures, see fig. 1-6. Absorption process of hydrogen into the material begins with the formation of solid solution (α phase) and when the utmost solid solution is gained, a hydride phase (β phase) starts to form. At certain condition, the α phase and β phase exists together and the isotherm shows a flat plateau. The length of plateau determines the quantity of hydrogen stored in the metal. In β phase region, the hydrogen pressure increases sharply with the hydrogen concentration. The two-phase region vanishes at the critical temperature beyond which α phase changes to β phase continuously. Metal hydride formation can be explained according to Gibbs phase rule:

$$f = c - p + 2 \text{...........(1-8)}$$

Where, f = degree of freedom, c = number of components (metal and hydrogen), p = number of phases (α, β and hydrogen gas)

At plateau there is just one degree of freedom exists. Therefore, a rise in hydrogen concentration takes place with the depletion of α-phase at a constant pressure. When α-phase is completely diminished, an additional degree of freedom is gained, and the hydrogen concentration increases (β-phase) with the rising pressure of hydrogen. More stable hydrides ($\Delta H_f \ll 0$) need elevated temperatures than that of less stable hydrides ($\Delta H_f < 0$) to attain a definite plateau pressure [21]. Gibbs free energy ΔG works as propulsion for the metal hydride formation at a certain temperature and pressure. The negative Gibbs free energy -ΔG

suggest the thermodynamic feasibility of a reaction even if the sluggish kinetics due to high activation barrier hinders the reaction to occur. Since ΔH is negative for hydriding reaction ($\Delta H^\circ < 0$), at low temperature, the large value of ΔH keeps ΔG negative during hydrogen absorption. However, at elevated temperatures, - $T\Delta S$ become larger than ΔH , resulting ΔG to be positive. This makes dehydrogenation process thermodynamically favorable. This explains why the hydrides in general need to be heated above 200°C for dehydrogenation reaction [23].

For the simple reaction, $M + H_2 \rightarrow MH_2$

ΔG is then approximated by:

$$\triangle G = \triangle G^o + RT \int_{Po}^{P} \frac{dP}{P} \ldots\ldots\ldots\ldots\ldots (1\text{-}9)$$

where, $\triangle G^o$ is the molar free energy at the reference state, P is the hydrogen pressure, Po is atmospheric pressure, R is gas constant and T is temperature

$$\Delta G^o = \Delta H^\circ - T\Delta S^\circ \ldots\ldots\ldots\ldots\ldots (1\text{-}10)$$

Since ΔG is zero at equilibrium, combining above two equations gives the relation between the equilibrium pressure (P) and temperature (T), which is known as Van't Hoff equation:

$$\ln\left(\frac{P}{p_0}\right) = -\frac{\Delta H^\circ}{RT} + \frac{\Delta S^\circ}{RT} \ldots\ldots\ldots\ldots\ldots (1\text{-}11)$$

where, ΔH° and ΔS° are the changes in enthalpy and entropy, respectively. In the hydrogenation process, the entropy change originate from the conversion of gaseous hydrogen to solid hydrogen and its value is roughly equal to the standard entropy of hydrogen ($\Delta S^\circ = 130\, J\, K^{-1} mol^{-1}$) and hence entropy of formation $\left(\Delta S_f \sim 130\, J\, K^{-1} mol^{-1}\right)$ for all metal-hydrogen system. ΔS_f for metal hydrides accompany to an important heat evolution

$\Delta Q = T.\Delta S°$, (exothermic reaction) during the hydrogen absorption and vice versa in desorption (endothermic reaction) of metal hydride. Hydrogen desorption below the room temperature can get heat from environment itself. Whereas, if the desorption occurs beyond the room temperature, the heat needs to provide from an outer source which may be the burning of the hydrogen, at necessary temperature.

Enthalpy can specify the stability of metal hydride bond. The hydride enthalpy can be calculated by the slope of the straight line gained by plotting $\ln(P_{H2})$ versus 1/T. The decomposition temperature for $P = p_0 = 0.1$ MPa (usually), $T_{dec} = \frac{\Delta H°}{\Delta S°}$ for $P = p_0$. To reach an equilibrium pressure of 0.1 MPa at 300 K, ΔH should amount to 39.2 $kJmol^{-1}H_2$. The stability of metal hydrides is usually presented in the form of van't Hoff plots. The enthalpy of formation for the most stable hydrides are $\Delta H_f = -226\ kJmol^{-1}H_2$ i.e. H_oH_2. For the least stable hydride like $FeH_{0.5}$, $NiH_{0.5}$, $MoH_{0.5}$ the enthalpy of formations are $\Delta H_f = +20\ kJ\ mol^{-1}H_2$, $\Delta H_f = +20\ kJmol^{-1}H_2$ and $\Delta H_f = +92kJmol^{-1}H_2$ respectively [22],[24].

1-4-2 Kinetics of hydrogen absorption and desorption

The rate of reaction cannot be obtained without the understanding of the hydrogen absorption and desorption kinetics. The thermodynamic properties acquired from PCT measurements can only give explanation about the driving force for the transformations, but it cannot provide information on the speed of reaction. Activation barrier needs to overcome when it comes to kinetic improvements. Fig. 1-7 shows a diagram of the energy barrier for the hydrogenation/dehydrogenation reaction.

The activation energy of reaction is estimated by the Arrhenius equation and the Kissinger equation:

$$\mathrm{K(T)} = A\exp\frac{-E_A}{RT}\ \text{(Arrhenius) [25]..............(1-12)}$$

$$ln\frac{\beta}{T_P^2} = ln\frac{AR}{E_A} - \frac{E_A}{RT_P}\quad \text{(Kissinger) [25]...........(1-13)}$$

where, E_A is activation energy, K(T) is rate constant, R and T are gas constant and temperature respectively, β is heating rate, T_P is peak temperature

Due to the existence of energy barrier for absorption (E_A), sometime the reaction can't proceed at low pressure and/or temperature even though the thermodynamics is favorable. This activation barrier is needed to overcome in order to enhance the kinetics of the reaction. The high activation energy for desorption (E_D) itself is huge for the process, which shows the elevated temperature requirement for the desorption of hydrides [23],[25].

As we already discussed about physisorption and chemisorption, let us discuss the steps involved in the process of metal hydride formation.

1. Physisorption of molecular hydrogen on metal surface
2. Dissociation of molecular hydrogen into atomic hydrogen and chemisorption on metal surface
3. Diffusion of hydrogen in the bulk metal
4. Solid solution (α phase) formation
5. Hydride formation (β phase formation)

As shown in fig. 1-5 E_A is the activation barrier in the chemisorption on the metal surface. Activation barrier slowdowns the process of dissociative adsorption and desorption. In dissociation step, the hydrogen atom is highly mobile and is interactive with metal surface. Further, chemisorbed atoms can penetrate in the sub-surface of metal and then diffuses into the interstitial sites of the metal lattice. The kinetics in the bulk is strongly influenced by mobility of atomic hydrogen. Fukai Y., [7] explains about the trapping phenomenon, according to him hydrogen atom can be trapped at interstitial sites of some impurities and it can jump to the neighbor sites by obtaining a heat energy from the phonon in the metal by diffusion [7]. Thus, the mechanism of diffusion is dependent on temperature. Diffusivity (D) can be explained by:

$$D = D_0 exp\left(-\frac{E_A}{KT}\right)..............(1\text{-}14)$$

Where, D_0 is a pre exponential factor which depends on the properties of metals and E_A is the activation energy of diffusion in the bulk material.

Fig. 1-8 shows some selective bcc metals and their hydrogen diffusion coefficients [7]. This fig. consists of experimental data which represents by the straight lines belong to Arrhenius plots in a fixed range of temperature. The Arrhenius plot always forming straight lines (Fig. 1-8) is an indication that the diffusion process is dominated by a single energy barrier, regardless of whether H atoms occupy between two different sites.

In the metal hydride formation process, the absorption reaction kinetics is mainly governed by the diffusion, nucleation and growth or movement of interface between the hydride and the metal.

1-5 How to tune thermodynamics and kinetics of hydrogen absorption /desorption

1-5-1 Thermodynamic Alteration

There are a lot of hydrides which have good thermodynamics which is helpful in taking and releasing the hydrogen at ambient conditions. But search is still continuing to have a combination of good kinetics and suitable thermodynamics of hydrides which can have better gravimetric capacity and can compete with 70 MPa compressed vessel in terms of weight. Several hydrides, borohydrides and complex hydrides such as LiH, MgH_2 and $LiBH_4$ have high gravimetric density but cannot desorb hydrogen at appropriate temperature or pressure due to thermodynamic constraints. To overcome this thermodynamic issue, usually a third element/additive or reactive hydride composites can be introduced. By the addition of these additives one can alter the enthalpy of reaction and hence improve the thermodynamics. To understand this more precisely, we can take an example of metal hydride system which desorb hydrogen to achieve its dehydrogenated state M with enthalpy X, see fig. 1-11. One can achieve more stable state i.e. MA_n than pure metal M by alloying with element A having a formation energy Y, which in turn reduce the enthalpy equals to X-Y for a transition between $MA_n + H_2$ (dehydrogenated state) and $MH_2 + nA$ (hydrogenated state). Thus, metal hydride system MH could be destabilized efficiently [26]. $LiBH_4$ has high gravimetric capacity 18.5 wt% but it releases H_2 at a temperature around 450°C. The addition of dual cation borohydrides $MLi_{m-n}(BH_4)m$ (M = Zn, Al, Zr) and MCl_x in $LiBH_4$ by ball milling was introduced by Li et al. [27]. They found that these double-cation borohydrides were easy to decompose, and the method was effective to adjust the thermodynamic stabilities of metal borohydrides. Some researchers found that combining the borohydride with metal hydride

(MgH_2) or complex hydrides (Mg_2NiH_4) was also effective technique to improve the dehydrogenation properties of metal borohydrides like $LiBH_4$ [28]. There is always an aspiration to search an efficient hydrogen storage material having superior thermodynamics.

1-5-2 Kinetic Alteration

Various routes have been proposed for decreasing the activation barrier and increasing the kinetics of hydrogen absorption/desorption, e.g. nano scaling and use of catalyst. Nano-scaling is an efficient way to lower the activation barrier through the creation of fresh and large surface, decreased diffusion distance for H atoms, however, agglomeration and difficult preparation of nano-sized material create bottleneck to adopt this method for practical/industrial use. On looking for the alternative approach, the use of catalysts plays a vital role to overcome the activation energy barrier in metal–hydrogen reaction. Catalyst can enhance the rate of reaction without changing the thermodynamics of Metal hydride system. Amount of catalyst is important in sample, i.e. to maintain the overall gravimetric capacity of the active sample, minimum amount of catalyst is possibly good. Highly dispersive catalyst has the high efficiency to boost up the reaction. Some researchers reported that alloying is one of the methods to alter the kinetics of reaction but in actual alloying change the thermodynamics, not the kinetics.

KH as excellent catalyst for metal hydrogen system

A breakthrough discovery of potassium hydride as catalyst was achieved by Wang et al., to stimulate $Mg(NH_2)_2/2LiH$ system. They proposed that potassium diffused into the imide or amide phases and then combined with nitrogen. Due to which the N-H bonds were diminished, that directly affected the dehydrogenation of the system and enhanced it. The hydrogen desorption peak was shifted for $Mg(NH_2)_2$/LiH system, to the lower temperature 132ºC by the addition of KH from 186ºC (without KH), as shown in fig. 1-9 [29]. This discovery attracted the researchers towards this magical catalyst. Many researchers worked on the mechanism of Li–Mg–N–H reaction with KH. In 2011, Teng et al. [30] proposed a new mechanism that the dehydrogenation improvement was occurred because of the reaction of KH with NH_3 which produced KNH_2 and then KNH_2 again reacted with LiH to regenerate KH. This process continued in loop and hence enhanced the decomposition of $Mg(NH_2)_2$/LiH system through the pseudo-catalytic effect of potassium hydride. The hydrogen desorption kinetics of LiH–NH_3 system was drastically improved by the inclusion of a little amount of KH and heating up to 100ºC [30]. Later in 2012, Durojaiye et al. compared the two systems $LiNH_2$ + MgH_2 and $2LiNH_2$ + MgH_2 and found that the ($2LiNH_2$ + MgH_2) system had a lesser decomposition temperature and a rapid kinetics. They concluded that KH was efficient as catalyst to increase the hydrogen desorption rates of ($2LiNH_2$ + MgH_2) system but it doesn't have any influence on the ($LiNH_2$ + MgH_2) system. The activation energy was decreased to 87 kJ/mol H_2 (for $1.9LiNH_2$ + MgH_2+0.1KH) from 119 kJ/mol H_2 for $2LiNH_2$ + MgH_2 system [31]. Recently, $LiNH_2$–LiH system was investigated for the effect of KH as catalyst and the hydrogen release temperature was reduced by approx. 30°C. The activation energy of the 5 mol% KH-added sample i.e. $LiNH_2$–LiH–0.05KH sample was found 90.4 kJ mol^{-1}, lowered by ~13% than undoped $LiNH_2$–LiH (103.1 kJ mol^{-1}) system. Dong et al. claimed reactivity of KH with NH_3 as a root cause for the enhancement of the desorption kinetics. Also, KH acted as a catalyst to accelerate the liberation of hydrogen by cyclic reactions [32]. Hence, we could understand the role of catalyst to improve the kinetics in hydrogen storage systems. Apart from nano-sizing, use of appropriate catalyst like potassium hydride (KH) can tune several systems kinetically. Many other systems need to be modified and, in this context, the effect of KH as a magical catalyst can be explored to reduce the activation barrier and advancement of research in hydrogen storage field.

1-6 Solid state hydrogen storage materials

The US Department of Energy (DOE) set the targets as long-term vision for hydrogen-storage applications accounting handling and storage cost as well as environmental parameters [33]. These targets for hydrogen storage systems are given in Table 1-1.

Table 1-1: The US DOE hydrogen storage targets for automobile applications [33],[34]

Year	**2006**	**2015**	**2020**
Gravimetric capacity	2kWhkg^{-1}system (6wt% hydrogen)	3kWhkg^{-1}system (9wt% hydrogen)	1.5kWhkg^{-1}system (4.5wt% hydrogen)
Volumetric capacity	0.045kgH$_2$L^{-1} system	0.081kgH$_2$L^{-1} system	0.030kgH$_2$L^{-1} system
Cost	US$4/kWh	US$2/kWh	US$10/kWh

These data clearly indicate the importance of both gravimetric and volumetric capacity of the storing media, as the storing media of hydrogen should not be large and bulky or shouldn’t occupy too much volume. Cycling property is as well significant so that the storage can be frequently cycled. Charging time is also important to consider and must not be longer than 3–5 minutes.

The hydrogen storage materials can be classified on the basis of binding nature of hydrogen:

physically bound hydrogen, chemically bound hydrogen (e.g. metal hydrides and complex hydrides). In the first type of storage materials, hydrogen is attached to the surface through weak van der waals interactions. Porous materials that lies in this category, are activated carbon, carbon materials having high surface area, zeolites and metal–organic frameworks (MOFs) [33]. Even though hydrogen physisorption process is weak exothermic, thus a heat management problem at the time of refueling occurs, that requires liquid nitrogen additionally to maintain the temperature at 77K. These reasons make porous materials unattractive for automobile on-board storage, but room temperature and high-pressure systems are still considered. However, they attracted the attention because of their reduced cost in comparison of liquid hydrogen for tanks and availability of compatible sizes.

Metal hydrides have larger storage density (6.5 H atoms/cm^3 for MgH_2) in comparison to the hydrogen gas (0.99H atoms/cm^3) or liquid hydrogen (4.2H atoms/cm^3),also attractive while considering the safety points [35]. Thus, solid state hydride is considered as safe with high energy density for onboard vehicular applications. An efficient storage material needs the following properties:

- High energy density i.e. high hydrogen content per unit mass and volume
- Reduced temperature and pressure for dissociation
- Decreased heat of formation to reduce the required energy for dehydrogenation
- Good reversibility
- Less activation barrier i.e. good kinetics
- Reduced cost and good safety features

Enormous efforts were put for optimizing the conditions and to improve the various materials used for hydrogen storage. MgH_2, FeTi, $LaNi_5$ and $MmNi_5$ are some commonly studied metal hydrides/materials. These storage materials are classified in 2 categories based on their simplicity and bonding nature, which will be explained in the subsequent section.

1-6-1 Metal hydrides

Metal hydrides consist of metal and hydrogen by forming a single type bonding (covalent, ionic or metallic) between them. These materials showed great potentials in the field of hydrogen storage. Metal hydrides have wide variety of class and can be classified as intermetallic compounds (AB_5, AB, AB_2, A_2B and AB_3-type alloys), where A is the element with good hydrogen affinity, while B is the metal with no or low affinity with hydrogen just to tune the hydrogenation properties of base metal. MgH_2 has been considered as an efficient metal hydride which contains a high H_2 storage capacity i.e. 7.7wt% with adequate reversibility and an additional benefit of small cost of magnesium. However, it needs high decomposition temperature of 300°C at 0.1 MPa pressure with the disadvantage of slow absorption and desorption kinetics. Most of the magnesium-based materials have an excellent cyclic stability, but the problem of high temperature and poor kinetics still remains to restrict its use for on-board vehicles [35],[36]. $LaNi_5$ is another popular material which has been studied widely across the world. In comparison of MgH_2, the intermetallic compound shows better storage characteristics, but the problem is associated with the gravimetric amount of stored hydrogen which is very low. At moderate temperature the hydrogen storage capacity of $LaNi_5$ doesn't exceed than 1.4wt% [37],[38].

1-6-2 Complex hydride

Due to the low hydrogen content of conventional metal hydrides, several hydrides termed as complex hydrides were developed by using light elements. Some typical example of these complex hydrides include alanates (sodium, potassium, lithium and calcium alanates), borohydrides (lithium, zinc, sodium and calcium borohydrides), amides (lithium amide), metal ammine complexes, chemical hydrides and Mg-based alloys [39]. Complex hydrides are salt like materials in which hydrogen is covalently bound to the central atoms and this unit is attached with the cation through ionic bonding. Generally, the complex hydrides can be represented as $A_xMe_yH_z$, where A is preferentially occupied by elements of the 1st and 2nd groups of the periodic table and Me is commonly employed by boron, aluminum or nitrogen. An extreme interest has been grown in light weight complex hydrides such as alanates $[AlH_4]^-$, amides $[NH_2]^-$, imides and borohydrides $[BH_4]^-$. The term alanates also known as aluminohydrides belongs to the compounds having hydrogen and aluminum associated with metal. Solium aluminium hydride ($NaAlH_4$) has been considered the most popular candidate of the alanates family along with some more like $LiAlH_4$, $Mg(AlH_4)_2$, $KAlH_4$, Na_2LiAlH_6, $Ca(AlH_4)_2$, K_2NaAlH_6. Imides and amides are also considered potential complex hydride due to their excessive storage density and lesser operating temperature, but these are legging due to their sluggish kinetics which limit them to be used practically onboard. Borohydrides (tetrahydroborate), are the noteworthy types of complex hydrides which are formed through covalently bonded hydrogen to the central atoms in the $[BH_4]^-$ complex anion. They are recognized because of their higher gravimetric and volumetric hydrogen capacity. Borohydrides comprises of general formula $M(BH_4)_n$ (M = Mn, Zn, Al, Be, Y, Dy, Gd, Zr, Rb, Cs; n = 1, 2, 3, 4; B is boron and H belongs to hydrogen) and some of popular are $NaBH_4$,

$LiBH_4$, $Mg(BH_4)_2$, $Ca(BH_4)_2$, $Zn(BH_4)_2$ [36]. Since the purpose of this thesis is related to thermodynamic and kinetic tuning of $LiBH_4$, the next section describes this system in detail.

1-7 $LiBH_4$ as promising material for hydrogen storage

$LiBH_4$ has been studied as a hydrogen storage medium due to its high gravimetric (18.5 wt%) and volumetric (121 kgH_2/m^3) capacities. However, the hydrogen accommodated in the lithium borohydride is not completely available for the reason that its decomposition provided the evolution of LiH and unbound boron, and approx. 13.8wt% hydrogen is liberated from 380°C to 680°C temperature, under atmospheric pressure. Due to the adverse thermodynamics and slow kinetics, lithium borohydride can release hydrogen only above its melting peak (~280°C). Several routes have been discussed to boost up the kinetics and thermodynamic properties of dehydrogenation of $LiBH_4$. According to safety point of views, complex hydrides are difficult to handle even though they have high energy density. Also, because of the high stability of elements composed by the decomposition of complex hydride, there is problem of refueling on board vehicles with hydrogen. Nonetheless, such kind of issues can be settled up by the improvement in thermodynamics by the addition of a new element (cation/anion substitution, additives) into the storage material.

The same holds true for $LiBH_4$ also. In a recent study an innovative technology high-energy ball milling with in-situ aerosol spraying (named BMAS) was found a good way to improve the MgH_2 added $LiBH_4$ not only kinetically but thermodynamically as well [40]. Puszkiel et al. reviewed various methods to enhance the destabilization properties of $LiBH_4$ like insertion of metal i.e. Mg, Ni, Al, Ca etc and metal hydride i.e. MgH_2, NaH, CaH_2 and nanoconfinement [41]. Stabilizing the dehydrogenated state could reduce the enthalpy of dehydrogenation and hence could increase the equilibrium hydrogen pressure. This approach could be used to boost the thermodynamic properties of many hydrogen storage materials. There is still a craving to improve the destabilization properties of $LiBH_4$ in such a way that it can be used practically onboard vehicles. Nanoconfinement or the addition of catalysts can also be used for thermodynamic destabilization [42],[39]. An effective approach was proposed by Reilly and Wiswall [43] in 1967, that the stability of a borohydride could be lowered by combining it with a suitable reaction metal (such as aluminum, magnesium or titanium). The main disadvantage of this approach was the reduced gravimetric hydrogen storage capacity due to the additional weight of the metal. Instead of the metal doping the use of an appropriate hydride could maintain a high hydrogen storage capacity with the formation of fully reversible systems under moderate temperature and hydrogen pressure conditions. Such systems are called Reactive Hydride Composites (RHC). Reactive Hydride Composite systems are not only based on borohydrides in fact, one of the first reported RHC was the $LiNH_2$–LiH system [44],[45]. In case of borohydrides, the RHC approach attracted a lot of attention, after the encouraging experimental results about the $LiBH_4$–MgH_2 system published by Barkhordarian et al. [46] and Vajo et al. [47]. The enthalpy of the destabilization reaction with a capacity of approx. 8-10 wt % was reduced by 25 kJ/mol H_2 in comparison of pure $LiBH_4$. This system was reported to desorb hydrogen at 225°C at equilibrium pressure of 1 bar, thus showed nice destabilization of $LiBH_4$ using MgH_2, however the sorption kinetics still remained an issue [48]. This interesting system is described in the subsequent section.

1-8 $2LiBH_4$ - MgH_2 System

According to Puszkiel et al. [41], the reaction for the destabilization of the $LiBH_4$ system by the inclusion of MgH_2 is as follows:

$$MgH_2(s) + 2LiBH_4(s) \leftrightarrows MgB_2(s) + 2LiH(s) + 4H_2(g) \ldots\ldots \text{ (1-15)}$$

The theoretical reaction enthalpy was decreased to 46 kJ mol^{-1} H_2 than that of individual for MgH_2 and $LiBH_4$ 76 kJ mol^{-1} H_2 and 67 kJ mol^{-1} H_2 respectively [48]. Destabilizing both hydrides (MgH_2 and $LiBH_4$) by the RHC concept was predicted to reduce the desorption temperature till 40°C under 0.1MPa of H_2 due to the low enthalpy value. The reaction is exothermic and MgB_2 is the formation product according to the reaction (1-15). MgH_2:2$LiBH_4$ -RHC system has the theoretical gravimetric capacity of 11.4 wt%. Fig. 1-10 indicates the free energy and the standard enthalpy of reaction per mol of H_2 emerging from the united destabilization of $LiBH_4$ and MgH_2 [41]. In 2005, Vajo et al. [48] first published a work about the destabilization of MgH_2:2$LiBH_4$-RHC system, and Barkohrdarian et al. [46] also initiated the concept of RHC in 2006-07. The MgH_2:2$LiBH_4$-RHC system was found different from the metal-hydrogen systems in terms of entropy values, this phenomenon was found to be related with the $[BH_4]^-$ cluster configuration upon hydrogen interaction. In order to understand MgH_2:2$LiBH_4$-RHC system, investigations into reaction route considering factors like temperatures, pressures, and stoichiometric compositions were executed by many researchers. The findings were fascinated on the hydrogen release steps (pathways). In 2007, Bösenberg et al. [49] firstly discussed the hydrogenation/dehydrogenation reaction steps of MgH_2:2$LiBH_4$-RHC system. On hydrogenation of MgB_2 + 2LiH system, lithium borohydride and magnesium borohydride were promptly formed in one reaction step at quite moderate conditions, 250–300°C temperature and 5 MPa of hydrogen pressure. A two steps process has been noticed during this process: first, the dehydrogenation of MgH_2 and after that the decomposition of $LiBH_4$. This system was decomposed into the MgB_2 and lithium hydride with the liberation of hydrogen gas. This two-stage reaction pathway revealed kinetic limitations, resulting the elevated dehydrogenation temperatures more than 400°C and below 0.3-0.5 MPa of hydrogen pressure. The thermodynamic and kinetic studies to check the reversibility of the MgH_2:$2LiBH_4$-RHC system by the addition of $TiCl_3$ was reported by Pinkerton et al [50]. In their work, a phase diagram was established for the desorption process from vacuum to 0.5 MPa pressure and from 250°C to 500°C temperature. Thermodynamically and kinetically $LiBH_4$ prefer to decompose into LiH and amorphous boron whereas MgH_2 decompose to Mg and H_2, at pressure less than 3 bar and temperature more than 400°C. Under the certain conditions i.e. from 280°Cto 450°C and pressures between 0.3 and 0.5 MPa MgH_2 and $LiBH_4$ were decomposed separately, however, the generation of MgB_2 and LiH was encouraged as ultimate outcomes. The findings were on the track and matched with the outcomes reported by Bösenberg et al [49]. Nakagawa et al. also reported their investigations on the consequence of the hydrogen backpressure on the hydrogen release of MgH_2:$2LiBH_4$-RHC [51]. They confirmed the presence of free boron and metallic Mg upon dehydrogenation under an inert gas atmosphere. MgH_2:$2LiBH_4$-RHC system represented sluggish kinetic behavior, needed long time for the hydrogen uptake and release. To understand the reaction mechanism of MgH_2:$2LiBH_4$-RHC system, several additives were enrolled by many researchers to speed up its kinetics. Despite of the fact the hydrogen storage properties of MgH_2:$2LiBH_4$-RHC system were noticeably revamped, the need of temperature more than 350°C is still a vital hinderance for a feasible use [41].

1-9 $LiBH_4$ as solid electrolyte and its use for Bi_2X_3 anode materials in all-solid-state Li-ion battery

Apart from the hydrogen storage field, $LiBH_4$ has also attracted attention because of its high ionic conductivity [52]. It was proposed to be used as solid-state electrolyte in battery applications for the first time by Takahashi et al.[53]. The cell was made of anode material Li, electrolyte $LiBH_4$ and cathode as $LiCoO_2$. Even if $LiBH_4$ showed excellent compatibility with Li-electrodes, a resistance was found at the interface because of the reaction between $LiBH_4$ and $LiCoO_2$. To overcome this issue, a layer linking electrolyte and cathode material was developed which reduced the resistance and allowed the discharge capacity of 89 mAh g^{-1} at a constant current density of 0.05 mA cm^{-2}. They concluded that a complex borohydride $LiBH_4$ may be used as an excellent electrolyte with oxide-based electrodes [53]. After this, many other researchers used $LiBH_4$ as solid electrolyte because it has high conductivity at elevated temperatures i.e. more than 120°C. [54],[55],[56]. Recently our group demonstrated that $LiBH_4$ can be used as solid electrolyte for Li-ion batteries and Bi_2Te_3 nanostructures prepared by wet chemical method as anode material. Excellent discharge capacities of 550.5 $mAhg^{-1}$ & 539.6 $mAhg^{-1}$ were achieved for nanoparticles and nanosheets. These capacities were found higher than 401 $mAhg^{-1}$ i.e. the theoretical capacity of Bi_2Te_3 nanostructures. Singh et al., discussed the possible reasons of the higher capacity than the theoretical one. They mentioned that one of the possibilities is the side reaction between Li-ions, acetylene black and oxide phase as well at the time of the charging of battery. Another possible reason was the existence of non-reacted elemental bismuth and tellurium that could take part in battery experiment. They mentioned the theoretical capacities as 384.7 $mAhg^{-1}$ and 420 $mAhg^{-1}$ respectively and not so high in case of elemental Bi and Te phases.

Therefore, the strong possibility was the side reaction of Li-ions with the acetylene black and with oxide phase. Fortunately, this was matched with the obtained high theoretical capacity of Bi_2O_3 and TeO_2 i.e. 690.2 $mAhg^{-1}$ and 1007.5 $mAhg^{-1}$ respectively [57]. To further examine the compatibility of $LiBH_4$ with Bi_2Te_3, Kumari et al., [58] synthesized the Bi_2Te_3 nanosheets by the solvothermal method and performed the electrochemical reaction between the Bi_2Te_3 nanosheets and Li-ion while using lithium borohydride as a solid electrolyte. The first discharge and charge capacities were found to be 555 $mAhg^{-1}$ & 1290 $mAhg^{-1}$ for Bi_2Te_3 nanosheets as anode material. In the time of the charging-discharging experiment, an unexpected but spectacular gas liberation was analyzed, which followed by an opening of the battery. This motivated us to think of the role of chalcogenides (Bi_2X_3, X= S, Se and Te) materials in the role of destabilization agent for $LiBH_4$ and formed as one of the motivation of this work.

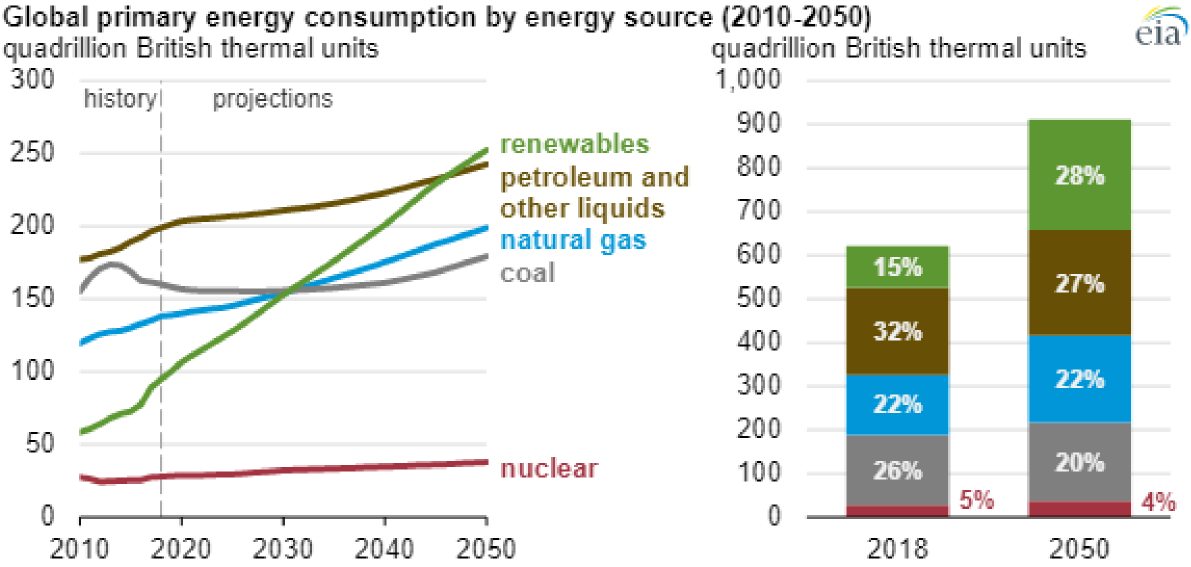

Fig. 1-1: Energy consumption in between 2018-2050 [2]

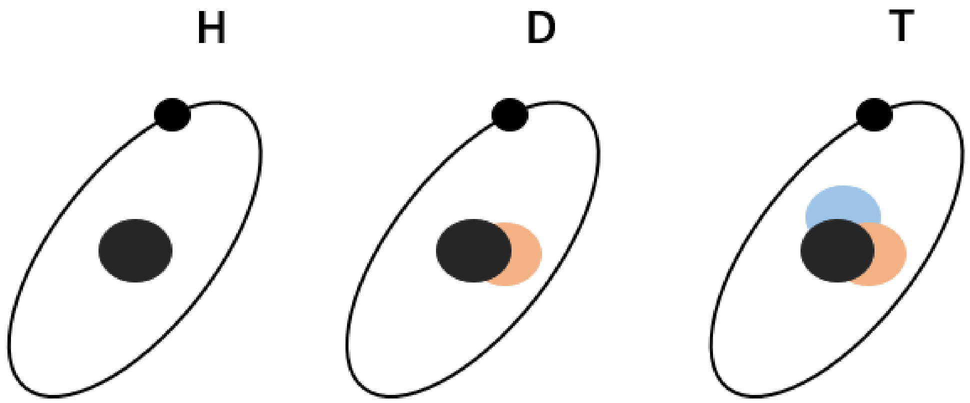

Fig. 1-2: Schematic representation of hydrogen or protium (H), deuterium (D) and tritium (T)

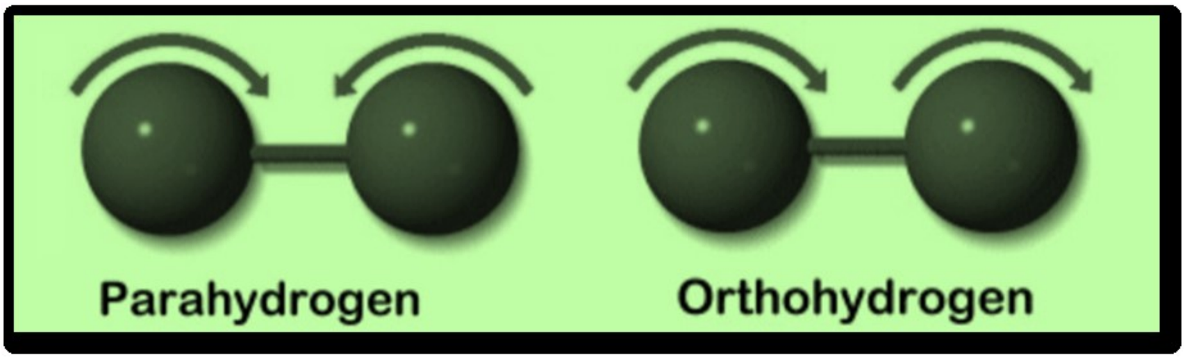

Fig. 1-3: Ortho and para hydrogen

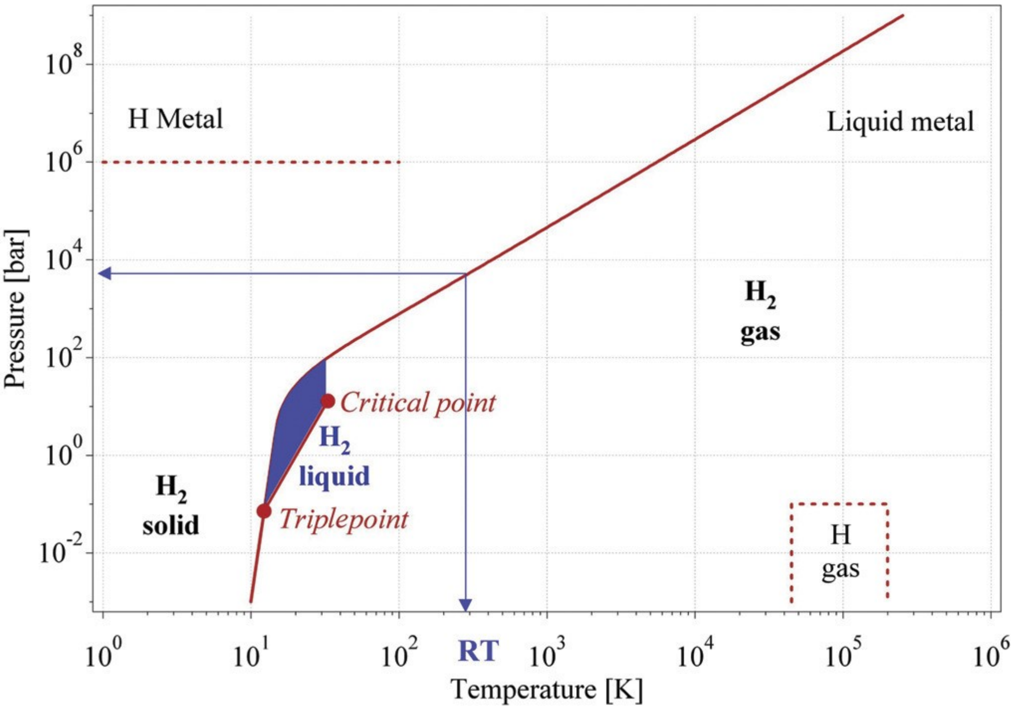

Fig. 1-4: Phase diagram of hydrogen; liquid hydrogen only exists between the solidus line and the line from the triple point at 21.2 K and the critical point at 32 K [9]

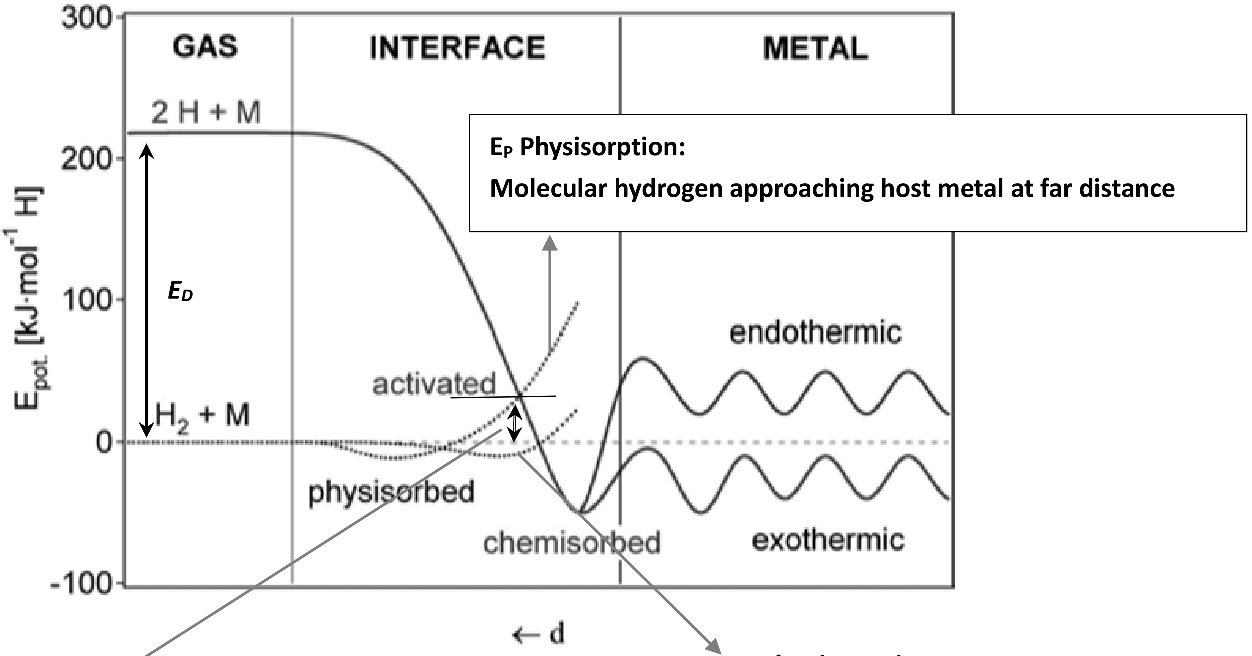

E_P Physisorption:
Molecular hydrogen approaching host metal at far distance

E_A Activation barrier: need energy to break the hydrogen bond in chemisorption

E_P Physisorption:
Molecular hydrogen approaching host metal near the surface

Fig. 1-5: Potential energy diagram for interaction of hydrogen with metal surfaces [9]

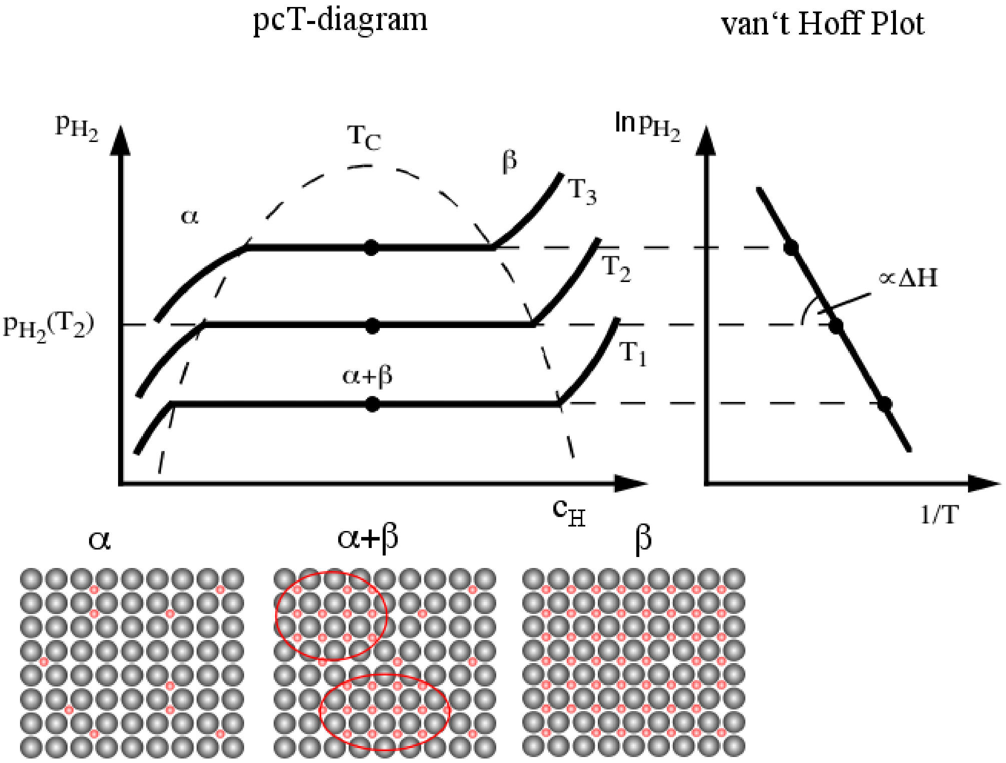

Fig. 1-6: Pressure–Composition–Temperature diagram (PCT isotherms). Inset: van't Hoff plot [59]

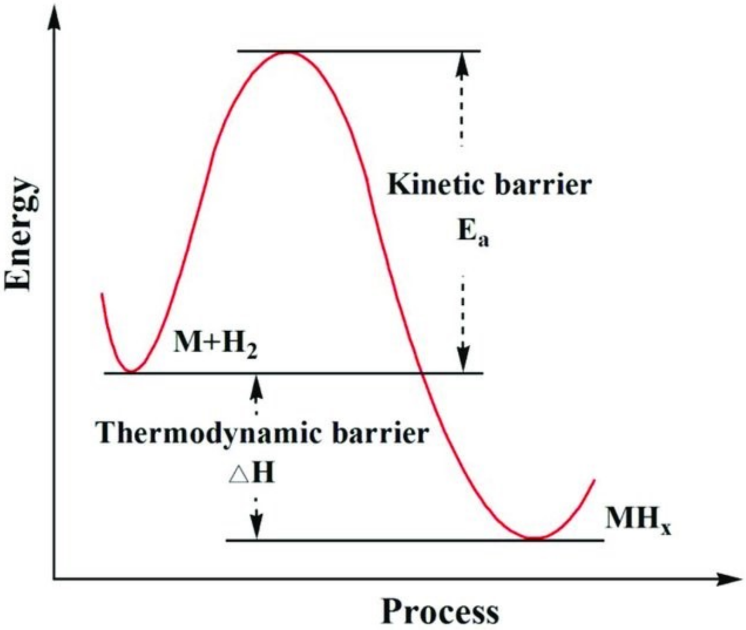

Fig. 1-7: Energy barrier for hydrogen de-/hydrogenation reaction of metal hydride [60]

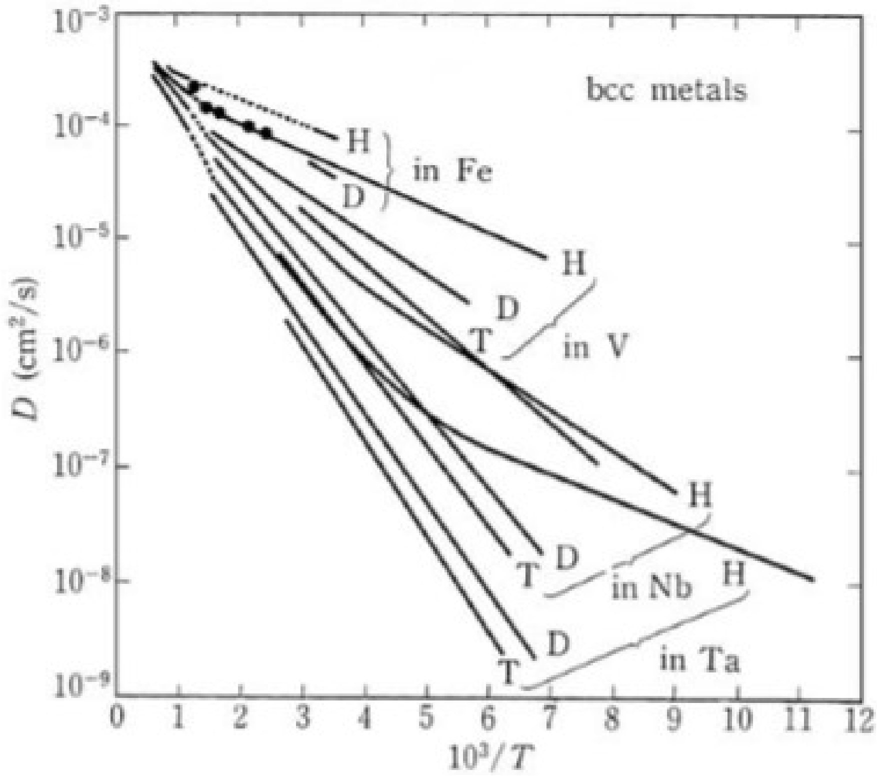

Fig. 1-8: Diffusion coefficients of hydrogen isotopes in some bcc metals [7]

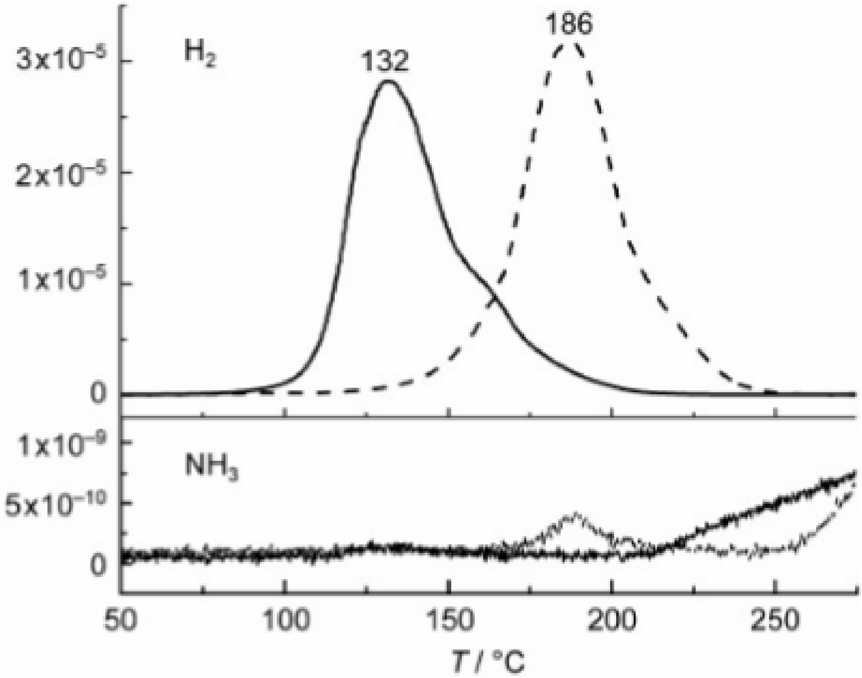

Fig. 1-9: Temperature dependences of H_2 and NH_3 release from the potassium-modified (—) and the pristine samples (- - - -) [29]

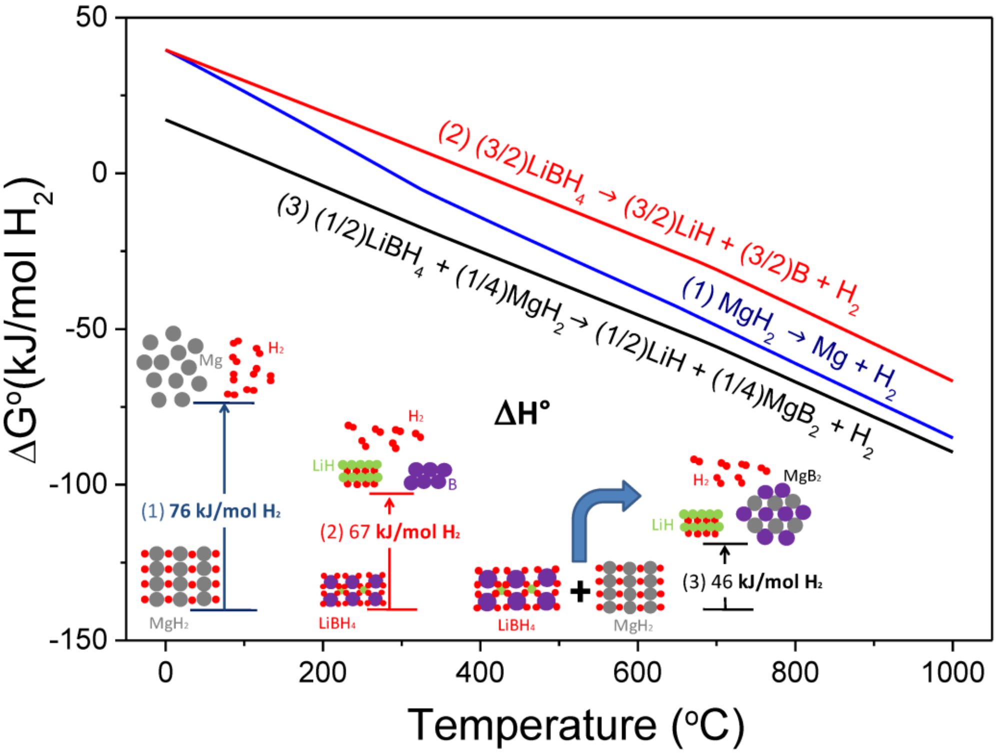

Fig. 1-10: Free energy per mol of H_2 as a function of temperature and the standard enthalpy of a reaction of the hydride system $2LiBH_4 + MgH_2$ [41]

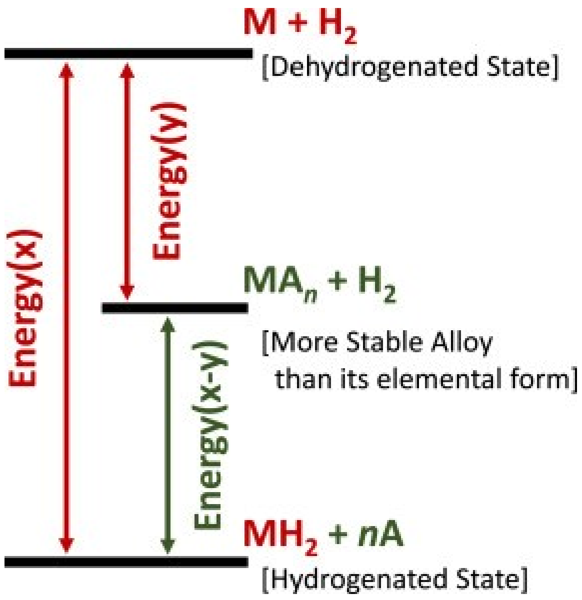

Fig. 1-11: Schematic of destabilization process of a hydride MH using third element A [26]

Chapter-2

Purpose of thesis

Hydrogen has high gravimetric energy density; however, it suffers from the low volumetric density. This has led the research community to develop efficient storage system for hydrogen. By the time, metal borohydrides and their composites have become attractive contender for stationary as well as transportation applications. $LiBH_4$ is one of the appropriate lightweight complex hydrides because it has high gravimetric (18.5 wt% H_2) and volumetric (121 g H_2/L) densities. However, due to its high thermodynamic stability and slow kinetics, it releases hydrogen completely above 900ºC which makes it incompatible with proton-exchange membrane (PEM) fuel cells [61]. Researchers have proposed many solutions to lower the desorption temperature of $LiBH_4$ (thermodynamic alteration) and to enhance its dehydrogenation rate (kinetic alteration). In order to solve above two issues, there were two objectives of this thesis related to the thermodynamic as well as kinetic alteration of $LiBH_4$ related systems. The first objective was to improve the kinetics of $2LiBH_4$-MgH_2 system by adding a magical catalyst KH. The second objective was to destabilize $LiBH_4$ itself by the addition of Bi_2X_3 (X = S, Se, Te) chalcogenides as both the elements of these chalcogenides i.e Bi and X have quite nice alloying ability with Li, which might cause an effective destabilization. Following were the detailed objectives of this thesis:

Objective 1: Even though $2LiBH_4$-MgH_2 system is destabilized in comparison to $LiBH_4$, it still possesses serious kinetic problem. Thus, in order to improve the kinetics of $2LiBH_4$-MgH_2 system, the addition of potassium hydride (KH) as a catalyst was attempted.

Magical catalytic activities of potassium hydride [29] evoked us to give a trial on this well-known complex hydrogen storage $2LiBH_4$-MgH_2 system. Thus, the effect of KH addition was studied using thermogravimetry coupled with differential thermal analysis (TG-DTA) and differential scanning calorimetry (DSC) in this work. During the course of this investigation, a unique phenomenon of eutectic melting was observed and elaborated in detail in order to identify the eutectic composition and eutectic temperature.

Objective 2: Second objective was focused on the destabilization of $LiBH_4$ itself. The motivation of this study was emerged during our recent experiments on all-solid-state Li-ion batteries [58], where an unexpected cell opening was observed during charging-discharging measurement which interrupted the cell operation in very few cycles. That cell was made of three major layers i.e. electrode material (composite of Bi_2Te_3/$LiBH_4$/acetylene black), solid electrolyte ($LiBH_4$) and Li-foil. The cell opening was suspected to be caused by the gas evolution during heating and electrochemical cycling. Thus, the thermolysis of Bi_2Te_3 / $LiBH_4$ composite was preliminarily investigated using TG-MS and the hydrogen evolution was found to be initiated at less than 120°C [58], which indicated the reaction between Bi_2Te_3 and $LiBH_4$. Similar behavior was observed during the charging cycle of Bi_2S_3 and Bi_2Se_3 electrode composites [62],[63] where the charging capacity at second plateau was found larger than the theoretical capacity due to the unidentified thermochemical reaction. This unwanted reaction resisted the above materials to be used in full potential window, which in turn lowered the overall capacity. This motivated us to explore the effect of Bi_2X_3 (X= Te, Se and S) addition on the decomposition temperature of $LiBH_4$ systematically. Aiming on the above, $LiBH_4$-Bi_2X_3 composites were prepared by ball milling and the effect of Bi_2X_3

addition on the decomposition temperature of $LiBH_4$ with a focus on structural changes was analyzed using X-ray diffraction (XRD) and Transmission Electron Microscopy (TEM) in this work. In addition to enhance the kinetics further, Bi_2X_3 nanostructures were also prepared and their effect was also observed on the desorption properties of $LiBH_4$.

Chapter-3

Materials and Methods

This chapter describes the information of commercially purchased materials, procedures for the synthesis of required materials. For the basic understanding of materials properties and their role in practical use, it is necessary to learn and utilize the characterization techniques. Keeping this in mind, this chapter explained the basic principle and methodology of used techniques.

3-1 Sample preparation

3-1-1 Materials

Materials used in this work are shown in Table 3-1. $LiBH_4$ was used after heat treatment at 200°C for 24 h under dynamic vacuum to remove the solvent impurities. KH was washed several times by hexane in order to remove the mineral oil and dried under vacuum for several hours. MgH_2, Bi_2X_3 were used without any treatment. All samples were handled solely under inert gas conditions in an argon filled glovebox.

3-1-2 Mechanical ball milling method

Mechanical ball-milling method was employed to prepare $2LiBH_4$-MgH_2 composite, x($2LiBH_4$-MgH_2) composite mixed with 1-x mol% KH (x = 5, 10, 20, 30, 40, 50, 55, 60, 65, 70, 80, 90) catalyst, $LiBH_4$-bulk 50 wt% Bi_2S_3, $LiBH_4$-bulk 50 wt% Bi_2Se_3 and $LiBH_4$-bulk 50 wt% Bi_2Te_3. Mechanical ball-milling method can give physical energy to the sample and therefore this method is used widely for various applications like synthesis of alloys, borohydrides, complex hydrides, mechanochemical reaction, formation of small particles, induction of defects etc.

Table 3-1 General information of materials used

S. No.	Material	Purity, state	Company
1.	**Lithium borohydride ($LiBH_4$)**	95%, powder	Sigma Aldrich
2.	**Magnesium borohydride (MgH_2)**	98%, powder	Alfa Aesar
3.	**Potassium hydride (KH)**		
4.	**Bismuth sulfide (Bi_2S_3)**	Alfa Aesar	99.9%
5.	**Bismuth selenide (Bi_2Se_3)**	Alfa Aesar	99.99%
6.	**Bismuth telluride (Bi_2Te_3)**	Alfa Aesar	99.98%
7.	**Bismuth nitrate pentahydrate ($Bi(NO_3)_3.5H_2O$)**	Loba Chemie	99.99%
8.	**Thiourea (CH_4N_2S)**	CDH	97%
9.	**Triethanol amine ($(HOCH_2CH_2)3N$**	Emplura	99%
10.	**N,N-Dimethylformamide (DMF)**	Emplura	99%
11.	**Selenium powder (Se)**	Aldrich	> 99.99%
12.	**Hydrazine hydrate (N_2H_4)**	Fisher Scientific	99%
13.	**Tellurium Powder (Te)**	Aldrich	99%
14.	**Sodium ethylenediaminetetraacetate (Na_2-EDTA) ($C_{10}H_{14}N_2Na_2O_8.2H_2O$)**	Scientific	98%
15.	**Sodium hydroxide (NaOH)**	Fisher Scientific	97%
16.	**Sodium borohydride ($NaBH_4$)**	Loba Chemie	97%
17.	**Ethanol (C_2H_5OH)**	Analytical	99.9%
18.	**Bismuth chloride ($BiCl_3$)**	Aldrich	98%

In this work, planetary (rotating) type ball mill apparatus (Fritsch, P7) as shown in fig. 3-1 was used to synthesize the samples. The milling pot with the inner volume of about 30 cm^3 was specially designed and made of Cr steel. Steel (SUJ-2; high-carbon chromium bearing steel in conformity with JIS G 4805) balls with 7 mm in diameter or zirconium oxide (ZrO_2) balls with 8 mm diameter were chosen for ball milling depending on situation (material used). In case of our first objective (i.e. $2LiBH_4$-MgH_2 composite, $2LiBH_4$-MgH_2 composite mixed with x% KH) 20 balls of ZrO_2 were opted with batches of 500 mg sample weight. The milling was conducted for a total of 2 h with a 30 min pause after 1 h milling. The details of all the studied samples with compositions are given in Table 3-2. For the preparation of samples for the second objective, 50 wt% Bi_2S_3, Bi_2Se_3 and Bi_2Te_3 were separately mixed with heat treated $LiBH_4$ by mechanochemical treatment in a planetary ball mill under inert conditions (Ar atmosphere). A total of 300 mg sample was prepared using 10 pieces of steel balls. The milling was conducted at 400 rpm for a total of 2 h with 1 h milling followed by 30 min pause pattern. The composites of prepared nanostructured Bi_2X_3 with heated $LiBH_4$ were also prepared using ball milling in a similar way adopted for the bulk Bi_2X_3 based composites.

3-1-3 Synthesis of nanostructures

All the nanostructures i.e. Bi_2S_3 nanoflowers, Bi_2Se_3 nanosheets and Bi_2Te_3 nanosheets were synthesized using hydrothermal method.

Preparation of Bi_2S_3 nanoflowes

For the preparation of Bi_2S_3 nanoflowers, first 0.61gm high purity (99.99%) bismuth nitrate pentahydrate ($Bi(NO_3)_3.5H_2O$) and 0.25 gm thiourea (Tu) were mixed and dissolved in 60 ml deionized water and were stirred at 250 rpm for 1 h. The solution was then transferred to a sealed autoclave which was heated at 140°C. 2 h later on finishing the reaction it was cooled down to room temperature. Then black color precipitate was collected after filtration and washed by deionized water and ethanol for several times and dried at room temperature, see fig. 3-2.

Preparation of Bi_2Se_3 nanosheets

Bi_2Se_3 nanosheets were also synthesized by hydrothermal process. High purity (99.99%) 2.6 mmol bismuth nitrate pentahydrate ($Bi(NO_3)_3.5H_2O$) triturate was added in 5 ml of triethanol amine and was mixed using stirrer. After 15 min, 15 mmol of NaOH was dissolved in 20 mL DMF and 7.4 mmol of Se powder was also added in it under constant stirring. 0.8 ml hydrazine hydrate (reducing agent) was also added during constant stirring. After continuous stirring for 1.5 h, the mixture was transferred into a Teflon-lined autoclave with 80 ml DMF and heated at 150 ^{o}C for 2 h. The black color precipitate was collected after cooling autoclave at room temperature and washed off with deionized water. After washing with water, it was washed using ethanol several times and then finally dried in the oven at 60 ^{o}C for 12 h, before characterization see fig. 3-3.

Preparation of Bi_2Te_3 nanosheets

For the preparation of Bi_2Te_3 nanosheets, 75.67 mg bismuth chloride ($BiCl_3$ - 99.99% purity) was mixed with 45.93 mg tellurium (Te) and 1g sodium ethylenediaminetetraacetate (Na_2-EDTA). After that the mixture was poured in 60 ml distilled water and stirred at 250 rpm. After 10 min stirring, it was transferred into a teflon lined 100ml autoclave reactor. Reducing agents 0.8gm sodium hydroxide (NaOH) and 0.8gm sodium borohydride ($NaBH_4$) were also mixed to the autoclaved sample after 30 min stirring. Reactor autoclave was then sealed and kept for heating at 180 ^{o}C for 27 h. After the reaction completion autoclave was cooled to room temperature and remaining black color precipitate was filtered and washed by deionized water and then with ethanol for many times. At last it was ready to dry at room temperature before characterizations, see fig. 3-4.

Table 3-2 Sample composition and molar ratio of components

Sample	x($2LiBH_4$-MgH_2)	(1-x)KH	Molar ratio ($LiBH_4$-MgH_2-KH)
S0 (0% KH)	**1.0**	**0.0**	**2.00:1.00:0.0**
S1 (5% KH)	**0.95**	**0.05**	**1.90:0.95:0.05**
S2 (10% KH)	**0.90**	**0.10**	**1.80:0.90:0.10**
S3 (20% KH)	**0.80**	**0.20**	**1.60:0.80:0.20**
S4 (30% KH)	**0.70**	**0.30**	**1.40:0.70:0.30**
S5 (40% KH)	**0.60**	**0.40**	**1.20:0.60:0.40**
S6 (50% KH)	**0.50**	**0.50**	**1.00:0.50:0.50**
S7 (55% KH)	**0.45**	**0.55**	**0.90:0.45:0.55**
S8 (60% KH)	**0.40**	**0.60**	**0.80:0.40:0.60**
S9 (65% KH)	**0.35**	**0.65**	**0.70:0.35:0.65**
S10 (70% KH)	**0.30**	**0.70**	**0.60:0.30:0.70**
S11 (80% KH)	**0.20**	**0.80**	**0.40:0.20:0.80**
S12 (90% KH)	**0.10**	**0.90**	**0.20:0.10:0.90**

3-2 Characterization techniques

3-2-1 X-ray Diffraction Spectroscopy (XRD)

Principle

XRD is an important technique for the characterization of crystalline materials and to determine their structures. When electrically accelerated thermoelectrons are irradiated to the target material for the generation of X-rays, an electron from inner energy level (such as K shell) is ejected. Then an electron from outer shell fall into the vacant place to make a stable ground state with emitting X-rays. When the voltage of X-ray tube is increased to a certain critical level, sharp intensity peak appears at specified wavelength, superimposed continuous spectrum. Since the maxima (peak) is so narrow and since their wavelengths are characteristic of the target metal used, they are called characteristic lines. Each crystalline powder sample has its own characteristic X-ray pattern and used as fingerprint for its identification by X-ray. Copper is the most common target material for crystal diffraction, with CuK_α radiation = 1.5418Å. Other material used as target are Cr, Fe, Co and Mo for characteristic X-ray. As shown in fig. 3-5, the interaction of the incident rays with the sample produces the diffracted rays which have a path difference AB+BC. These diffracted X-rays undergone through a constructive interference when they satisfy Bragg's Law [64]:

$$n\lambda=2d \sin \theta$$

where, n = an integer determined by the order given,

λ = wavelength of incident X-rays,

d = spacing between planes in the atomic lattice and

θ = angle between the incident ray and scattering planes (diffraction angle).

Bragg's law relates the wavelength of electromagnetic radiation, the diffraction angle and the lattice spacing in a crystalline sample. The diffraction angle between the diffracted and incident beam i.e. 2θ is measured experimentally. The spacing between planes in the atomic lattice can be calculated according to the structures of the crystal, for example for cubic structure:

$$\frac{1}{d^2} = \frac{h^2 + k^2 + \ell^2}{a^2}$$

where, d is the spacing between adjacent (hkl) lattice planes

h, k and l are miller indices and a is lattice constant [65]

Procedure

Rigaku-RINT 2500 diffractometer equipped with CuKα radiation (as shown in fig. 3-6) was used in this work. All the samples were prepared in high purity Ar-filled glove box. The samples were set on glass plate spread with grease for high vacuum. All samples were covered by a polyimide sheet (Dupont-Toray Co. Ltd., Kapton) of 8μm thickness to protect them from air as shown in fig. 3-7. This technique was used for the structural characterization of all the samples after milling and heating treatment at different temperatures.

3-2-2 Thermal analysis for gas desorption

3-2-2-1 Thermogravimetry – Differential thermal analysis (TG-DTA)

Principle

TG-DTA is a thermal analysis technique as shown in fig. 3-8 and 3-9. Fig. 3-8 shows the schematic representation of thermo-balance (apparatus), where, SDTA stands for single differential thermal apparatus. The weight loss is detected during the desorption of gases as a function of temperature. Thermo sensors attached to the balance can detect the heat flow due to the gas desorption or phase transition of the sample. For the DTA measurement, an exothermic or endothermic reaction takes place during the programmed heating or cooling of the sample. In this process a phase transition of the sample, melting and desorption temperature can be detected. There were two pans equipped in the machine, one was used as reference pan and another holds the sample. In principle, the sample pan made of aluminum (Al) and alumina (Al_2O_3) can be available up to 500 and 900°C, respectively or sometimes platinum for higher temperature range. The choice of sample pan totally depends on the studied material and related reaction mechanism. On increasing temperature, the temperature difference ($\triangle$T) was observed by the thermocouple equipped with each holder. The TG-DTA apparatus used in this work was connected with thermal desorption mass spectroscopy which is explained in next section. The desorbed gases during heating in TG-DTA flowed through a capillary by flowing Ar as carrier gas, to the connected TDMS (thermal desorption mass spectroscopy) apparatus. Hence, the partial pressure of desorbed gases was continuously removed from the reaction area of TG-DTA to maintain zero partial pressure of desorbed gases throughout the reaction. In case of hydrogen storage materials, if the desorbed gas is only hydrogen then the weight loss will be corresponding to the capacity of hydrogen of the sample [66].

3-2-2-2 Thermal Desorption Mass Spectroscopy (TDMS)

Principle

In this work, thermal gases desorption properties of all the samples were examined by TG-DTA coupled with mass spectroscopy. This method enables the immediate determination of volatile reaction products: a small part of the gas which is formed on heating in the DTA furnace enters the ionization chamber of the mass spectrometer through a narrow capillary and a valve, where it can be investigated immediately. The gas molecule desorbed from the sample are ionized by confliction with electron beam in ionization part. Thus, the ionized gas molecules can be expressed as m/z, where, m is mass of sample molecules and z is charge number. A recorder shows the thermal effects as well as the composition of the gaseous reaction products in dependence on the heating temperature.

Procedure

The thermal properties of all the samples synthesized in this thesis were investigated by TG-DTA apparatus (Rigaku, TG8120) coupled with a mass spectrometer (MS, Anelva, M-QA200TS) which was installed inside the glove box to minimize an influence of exposing the samples to air see fig. 3-9. About 3 ~ 5 mg of the sample was put on a pan and set to the balance in the TG-DTA apparatus. This instrument was used in both objectives of this thesis to understand the reaction mechanism at different temperatures and phase change during the heating process. TG coupled with DTA and Mass spectroscopy was performed under an argon gas flow (300 ml/min), at the heating rate of 5°C/min. This technique was also helpful to analyze the released gases during different stage of reaction.

3-2-2-3 Differential scanning calorimetry (DSC)

Principle

Heat flux (enthalpy change) with exothermic or endothermic reactions are measured by the DSC (Differential scanning calorimetry). This technique is more effective than that of previous one i.e. TG-DTA as heat quantity of the corresponding reaction can be detected more sensitively than TG-DTA. Moreover, large amount of samples can be used for analyzation in case of DSC resulting in clear signals. The integrated area of peaks observed in DSC measurement theoretically corresponds to the heat of reaction. There are two types of DSC, one is power compensated type DSC and second is heat flux type DSC. Heat flux type of DSC was used in this work, see the schematic diagram in fig. 3-10 [66]. Enthalpy change and heat capacity change in the sample causes a difference of temperature between the sample and reference, which is recorded by DSC measurement. The DSC measurements are able to perform under open system (gas flow system) and closed system within the maximum pressure of 7MPa.

Procedure

The high pressurized DSC apparatus (Q10 PDSC, TA instruments) was installed in a glove box to avoid the contact with air and impurity, see fig. 3-11. About 3 mg sample was put on Al pan and set in furnace. The DSC measurements was carried out in the range of 30 to 500ºC with the heating rate 5ºC/min. Cooling was also recorded after completion of heating measurement. All the measurements were performed under 0.1 MPa Ar gas.

3-2-4 Transmission Electron Microscopy (TEM)

Principle

TEM (Transmission Electron Microscopy) is an important technique to characterize the microstructures and nanostructures in which electrons are radiated to the solid samples. The electrons interact with sample and get transmitted through it and strike a fluorescent screen to generate high resolution sample image. TEM works on the same principle as light microscope but instead of light a high energy electron beam is used to produce an image. As De-Broglie wavelength of the electrons is much smaller than that of photons so TEM can produce high resolution images. The detailed information about sample crystal structure can be detected by the TEM. Fig. 3-12 shows the interaction of incident electron beam with the specimen sample. Some electrons are scattered without losing their energy (elastic scattering) and some scattered with the partial loss of energy (inelastic scattering). Suppose a parallel electron beam interacts with the specimen, some of the electrons penetrate through the sample (transmitted) and others are diffracted at some angle. However, a diffraction pattern can be obtained when a film is set at the point of focal back plane and an electron microscope image can be produced when a film is set at the imaging plane see fig. 3-13. There are two modes in

TEM to construct an image, one is bright field image, and another is dark field mode image. When an unscattered (transmitted) electron is selected with the aperture and the scattered electron beam is restricted to pass through the back focal plane then a bright field image can be obtained because of the transmission of electrons and hence less electron accumulation. On the other hand, in dark field mode of image, a scattered beam is selected to pass through and unscattered electrons are restricted to the aperture. Therefore, in dark field mode, the area around the sample being examined appears light, rather than dark. Bright field images are the most common one obtained from the TEM [67].

Procedure

In this thesis work, TEM experiments were performed using 200 kV TEM (JEOL JEM 2010) to characterize nanostructured Bi_2X_3 (X = Te, Se, & S) samples and their composites with $LiBH_4$. In-situ study was performed to understand the reaction mechanism of these composites at different temperatures. A molybdenum grid was used to hold the spread sample and afterwards the sample was moved to TEM chamber. During the sample loading, plastic bag method was adopted to reduce the air contact for TEM samples [68].

3-2-5 Scanning Electron Microscopy (SEM)

Principle

When electron beam is focused on the sample, it interacts with the atoms and penetrate in the sample material. In case of SEM the interaction depends on volume of electrons in the sample. There are some specified modes of imaging in the SEM, i.e. secondary electron, back scattered and characteristics X-ray, see fig. 3-14 ejected by the primary beam from a shell. When primary electrons interact with the atoms of the specimen secondary electron are generated by the inelastic scattering. Due to the low energy (50 eV) these electrons are generated from only few nanometers inside the sample surface, thus giving the information about the surface morphology. In case of BSE (backscattered electrons), primary electron beam deviate due to the interaction with the nuclei of the sample atom and by the elastic scattering the BSE generated see fig. 3-15. For a sample, the volume of interaction depends on mean atomic number, density and beam energy. BSE have high energy and can penetrate deep within the sample. High atomic number elements can generate BSE more strongly than the less atomic number elements. For example Au have large nuclei ($z=79$) therefore providing more powerful effect to the path of the primary electron beam and developing the large deviations [69]. Secondary electrons are used to study the topology of the materials whereas characteristic X-rays are used to perform the elemental mapping of the samples. The electron beam can be generated by choosing an electron gun. Two types of electron gun are commonly used, i.e. thermoelectron and field emission (FE). The high resolution observation can be obtained using FE type gun. Fig. 3-16 shows the schematic diagram of SEM.

Procedure

In this thesis, prepared nanostructures (Bi_2S_3, Bi_2Se_3 and Bi_2Te_3) were characterized by the SEM instrument (Nova Nano FE-SEM 450 FEI). The accelerating voltage was used 15 kV for the instrument. JEOL JSM 6380 was used to observe the surface morphology of materials before and after heating (used instrument images are shown in fig. 3-17). The samples were prepared inside the glove box and transferred to the SEM apparatus by using Sample transfer stick as shown in fig. 3-17.

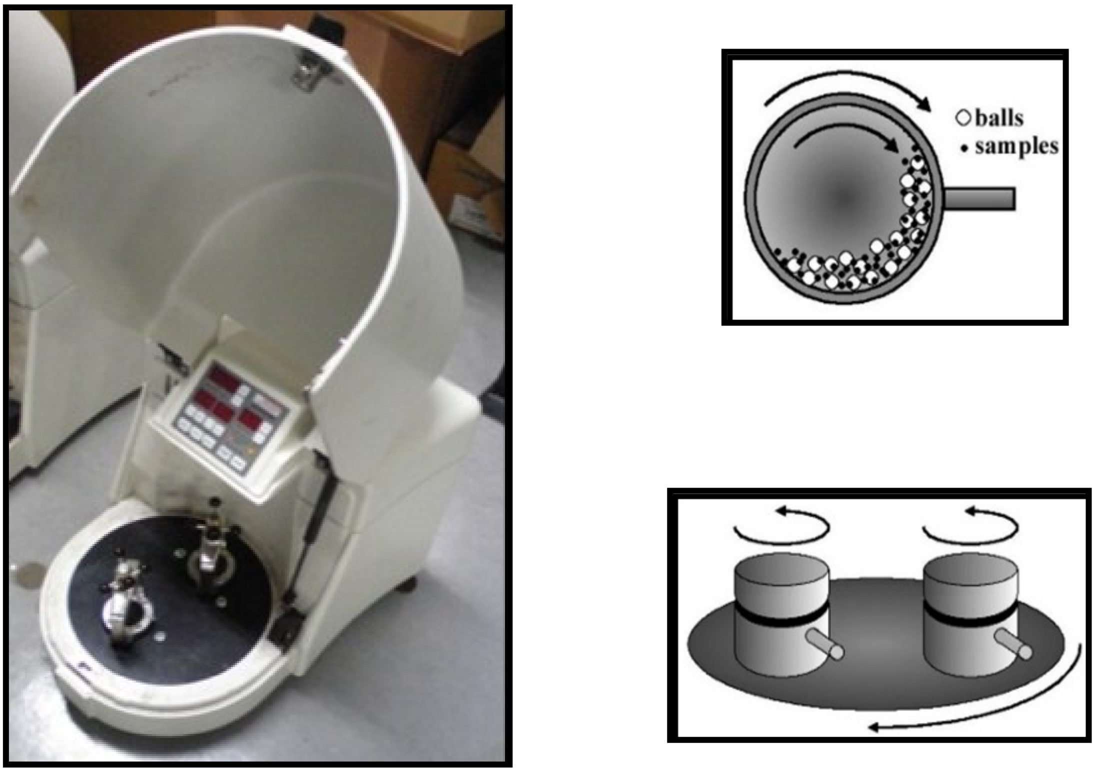

Fig. 3-1: Planetary ball mill

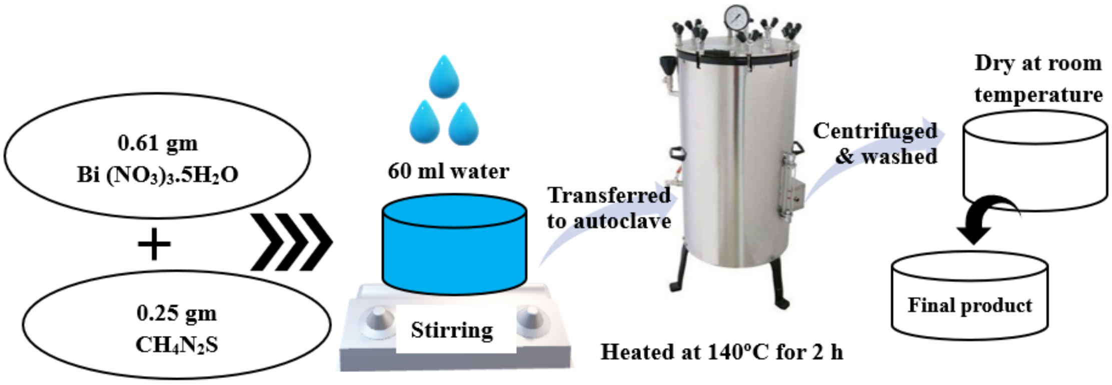

Fig. 3-2: Schematic for the synthesis of Bi_2S_3 nanoflowers

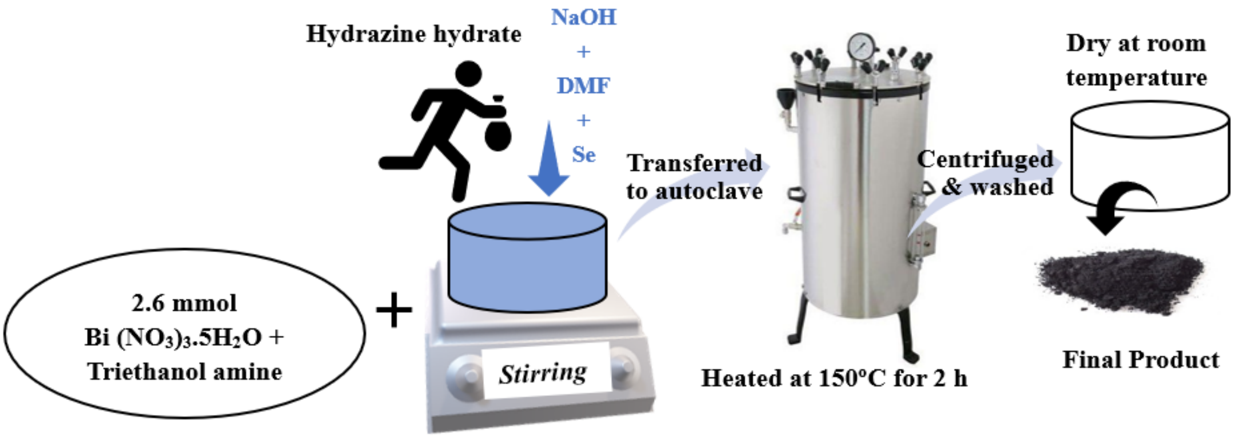

Fig. 3-3: Schematic for the synthesis of Bi_2Se_3 nanostructures

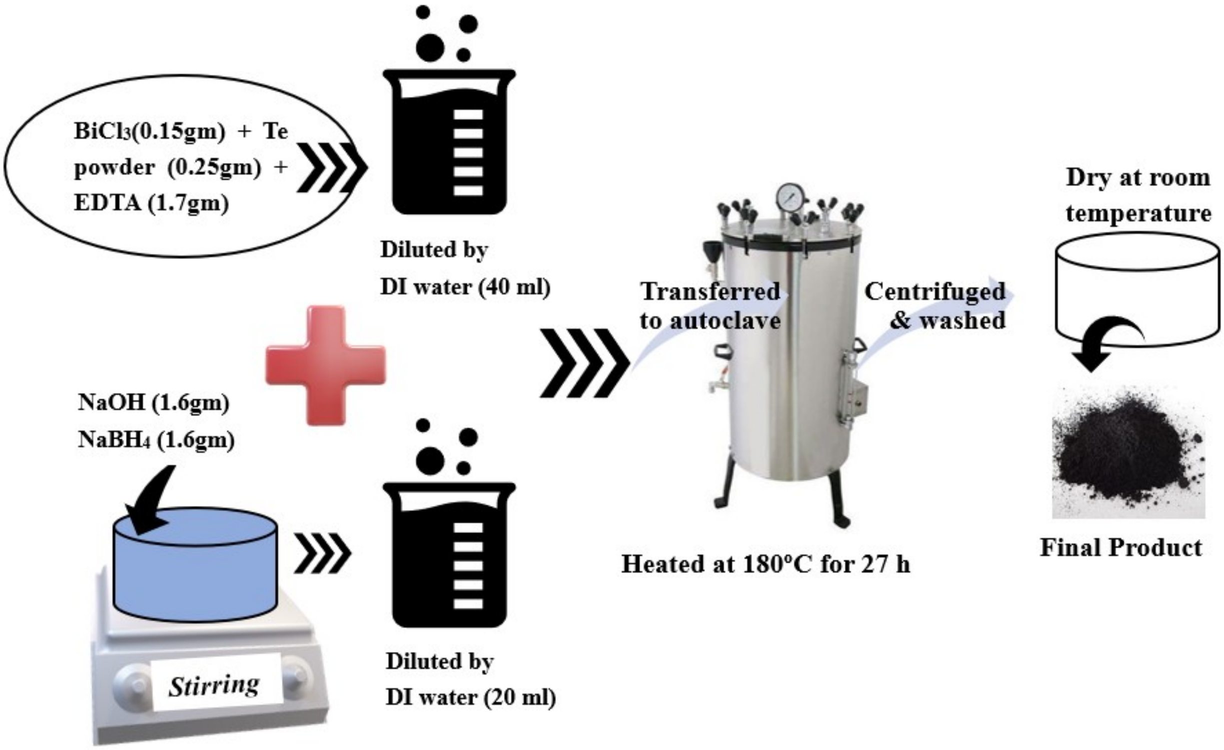

Fig. 3-4: Schematic for the synthesis of Bi_2Te_3 nanostructures

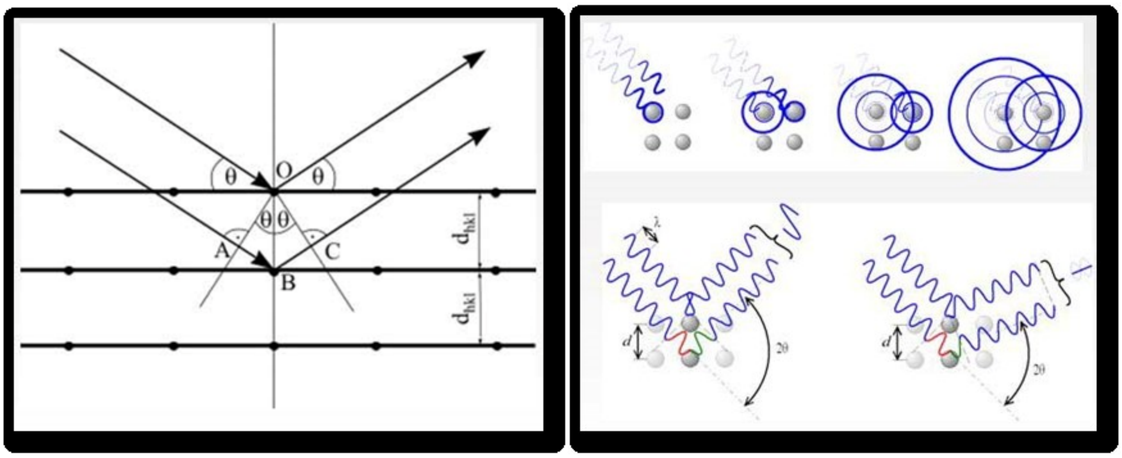

Fig. 3-5: Diffraction of X-ray from lattice planes in crystal [3-2, 3-3]

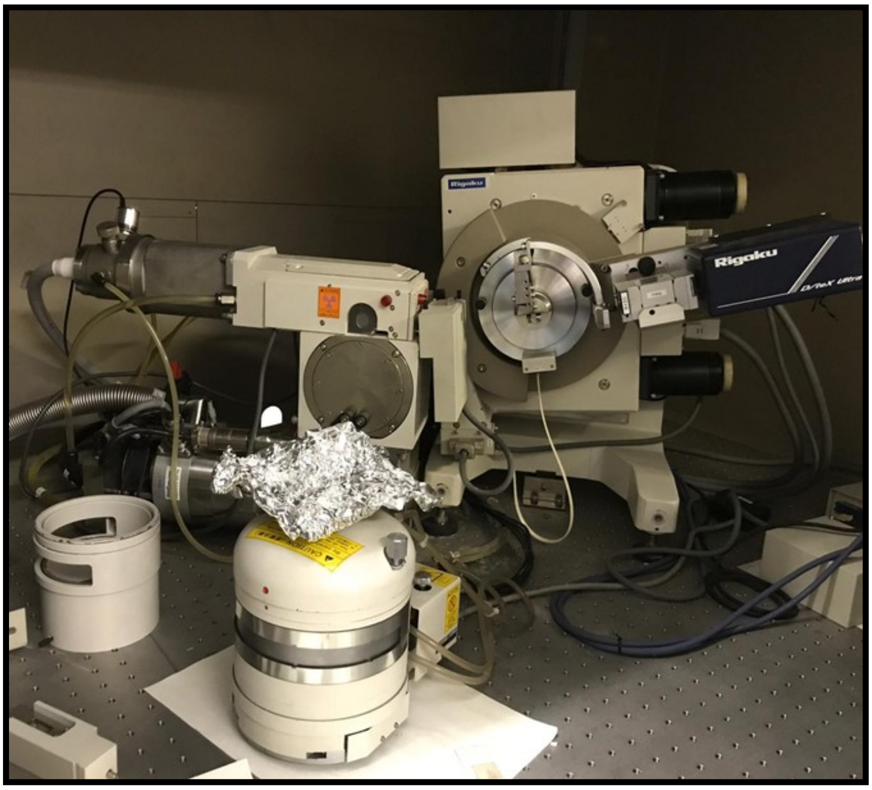

Fig. 3-6: Picture of Rigaku-RINT 2500 XRD equipment

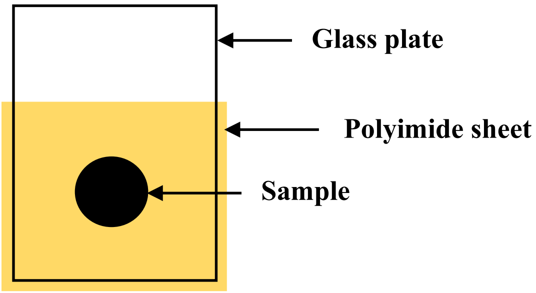

Fig. 3-7: Sample for XRD measurement

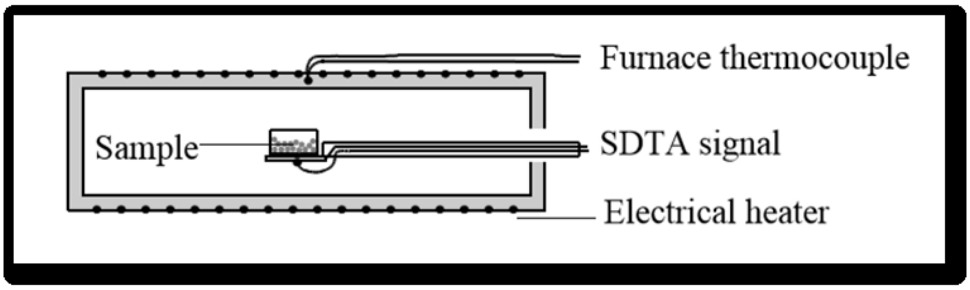

Fig. 3-8: Schematic of TG-DTA apparatus

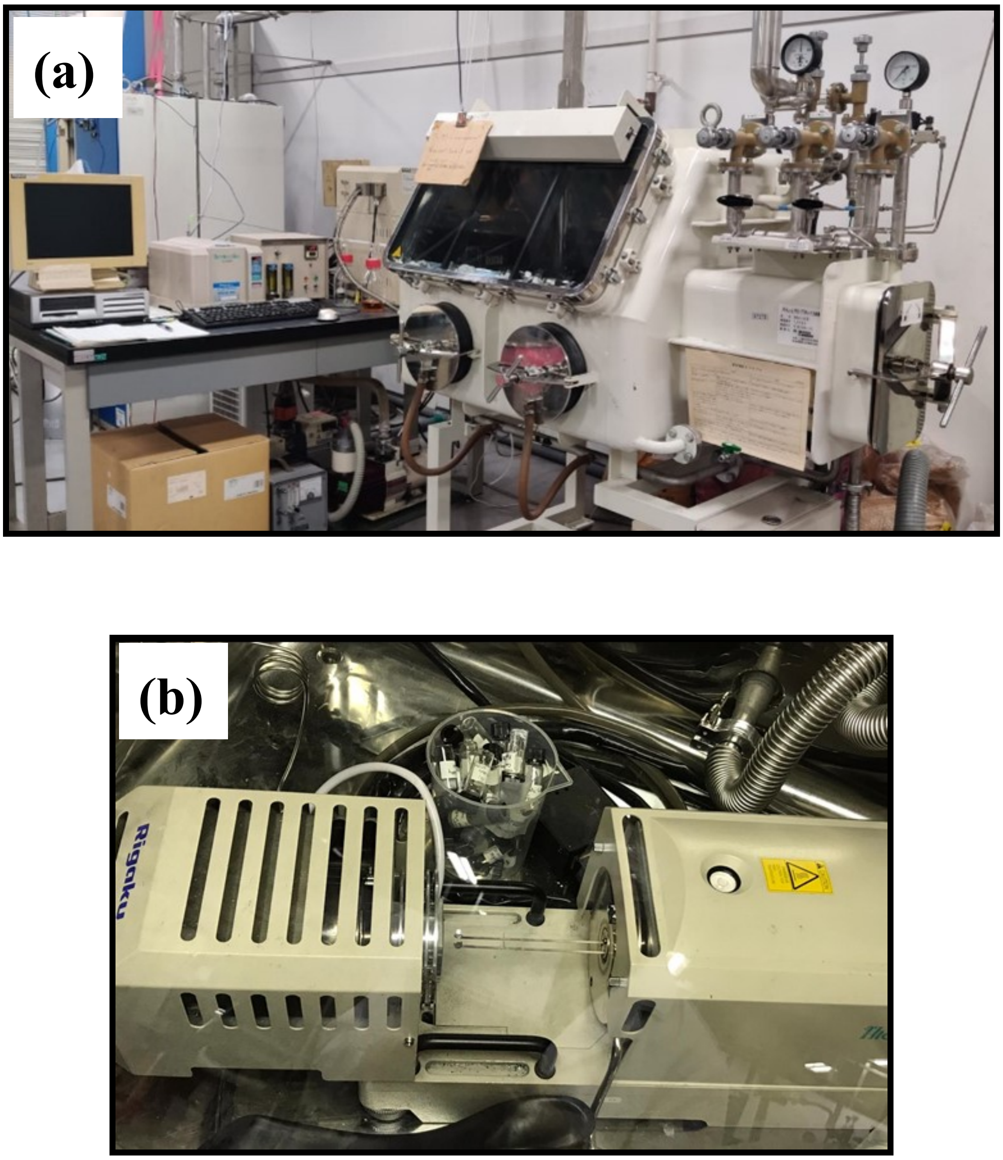

Fig. 3-9: (a) Rigaku, TG8120 connected to a mass spectrometer (MS, Anelva, M-QA200TS) glove box, (b) TG-DTA instrument inside the glove box

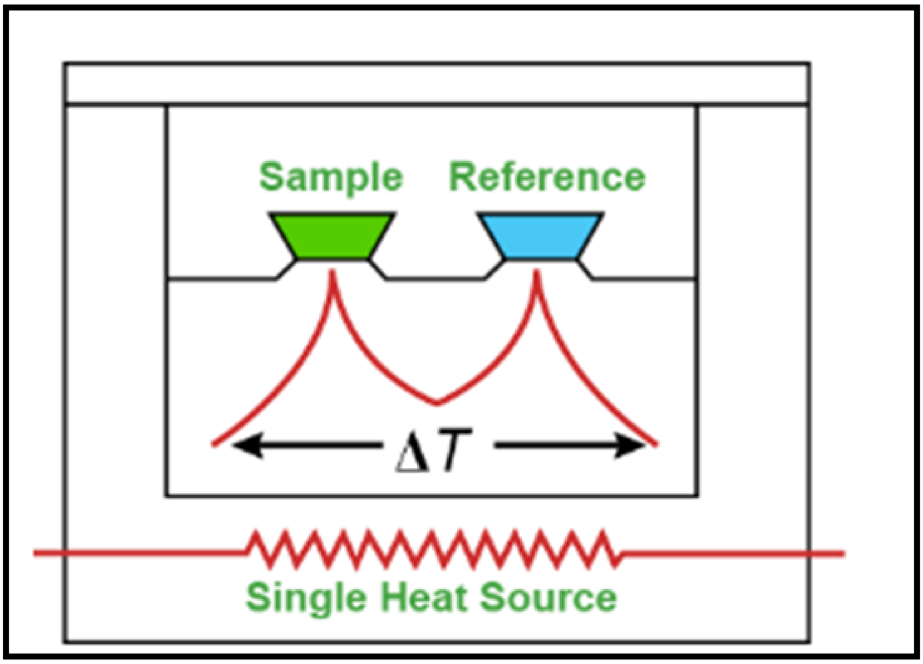

Fig. 3-10: Schematic of heat flux type DSC apparatus

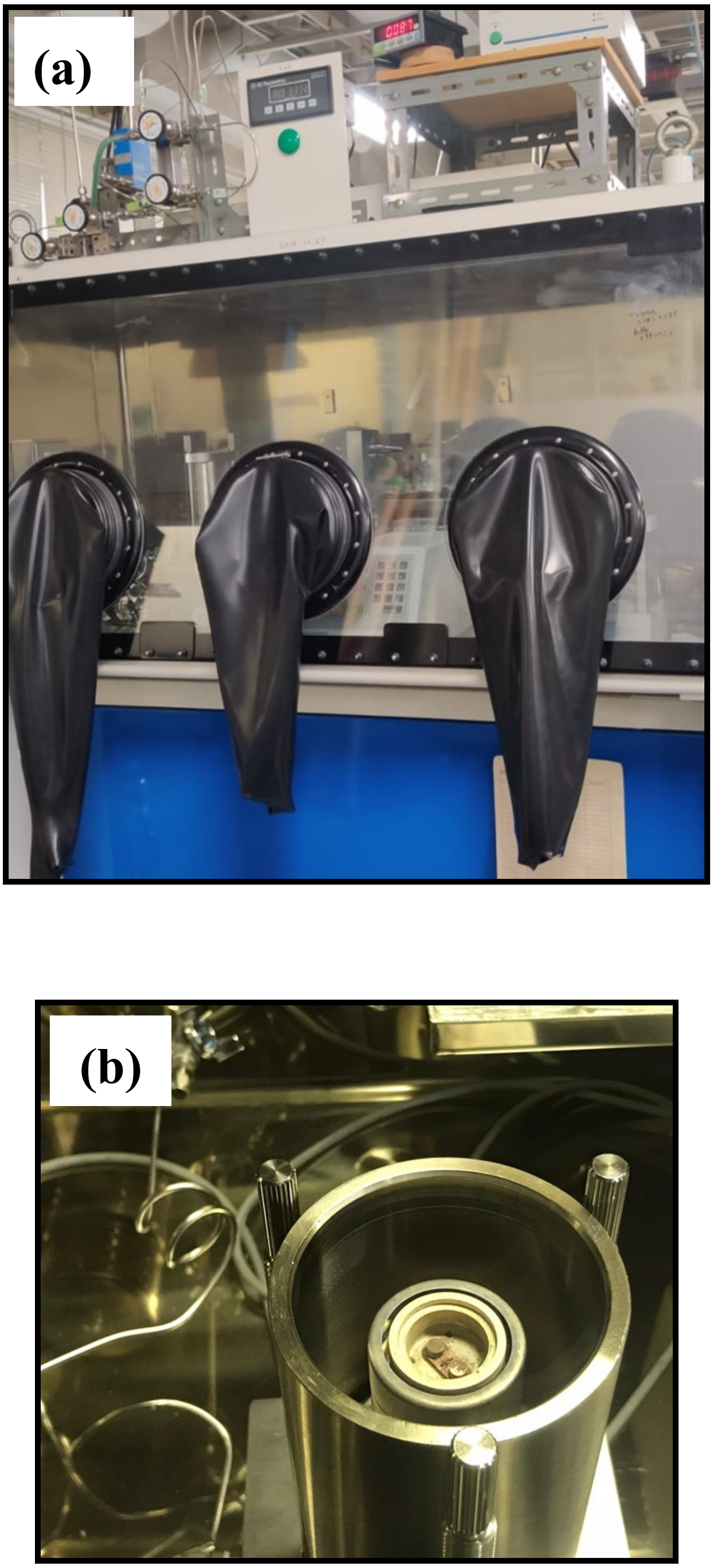

Fig. 3-11: Image of Q10 PDSC, TA instruments DSC apparatus (a) Closed DSC setup inside glove box (b) Open DSC instrument

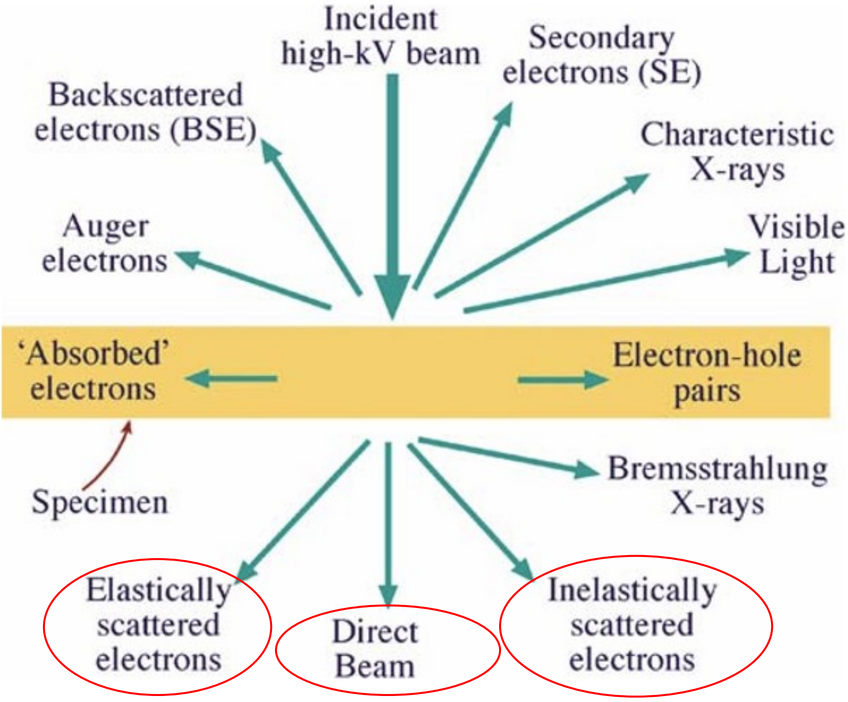

Fig. 3-12: Generated signals when a high-energy beam of electrons interacts with a thin specimen

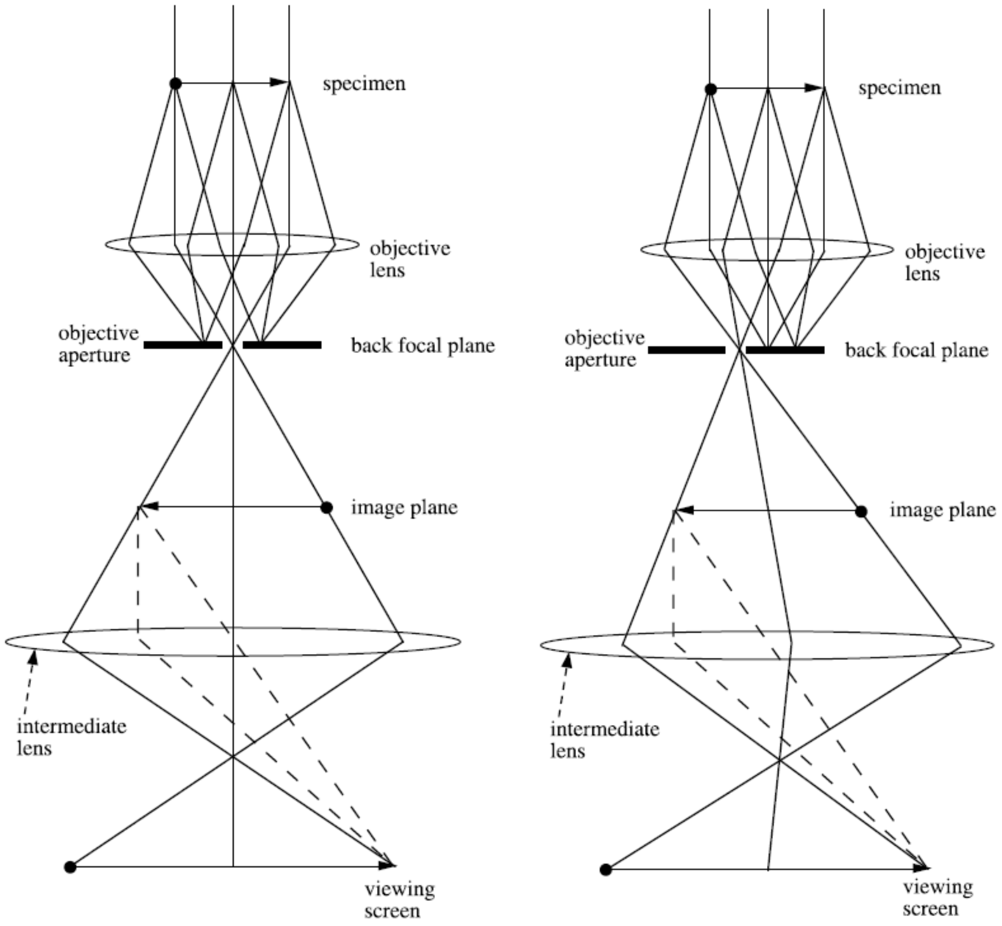

Fig. 3-13: (a) Left: bright-field (BF) mode. (b) Right: dark-field (DF) mode

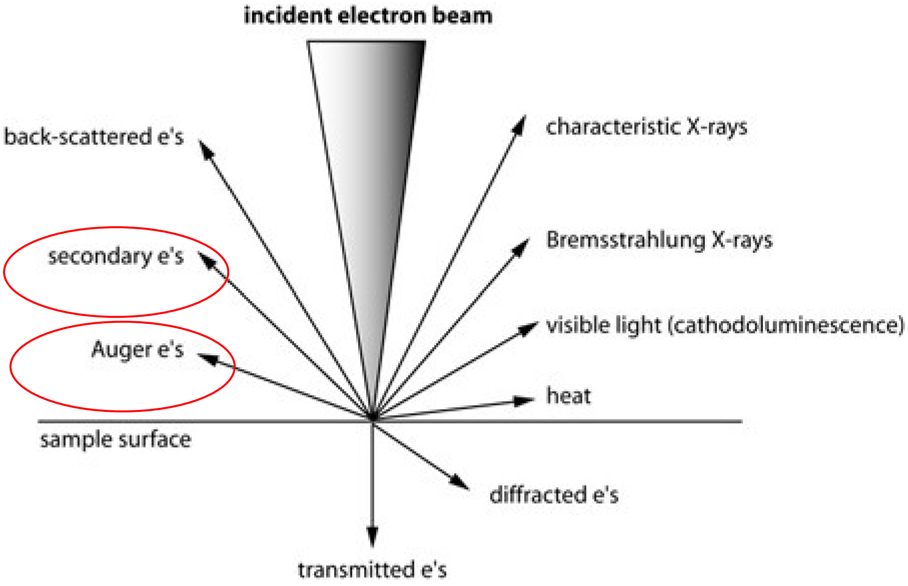

Fig. 3-14: Interactions between electrons and a sample [70]

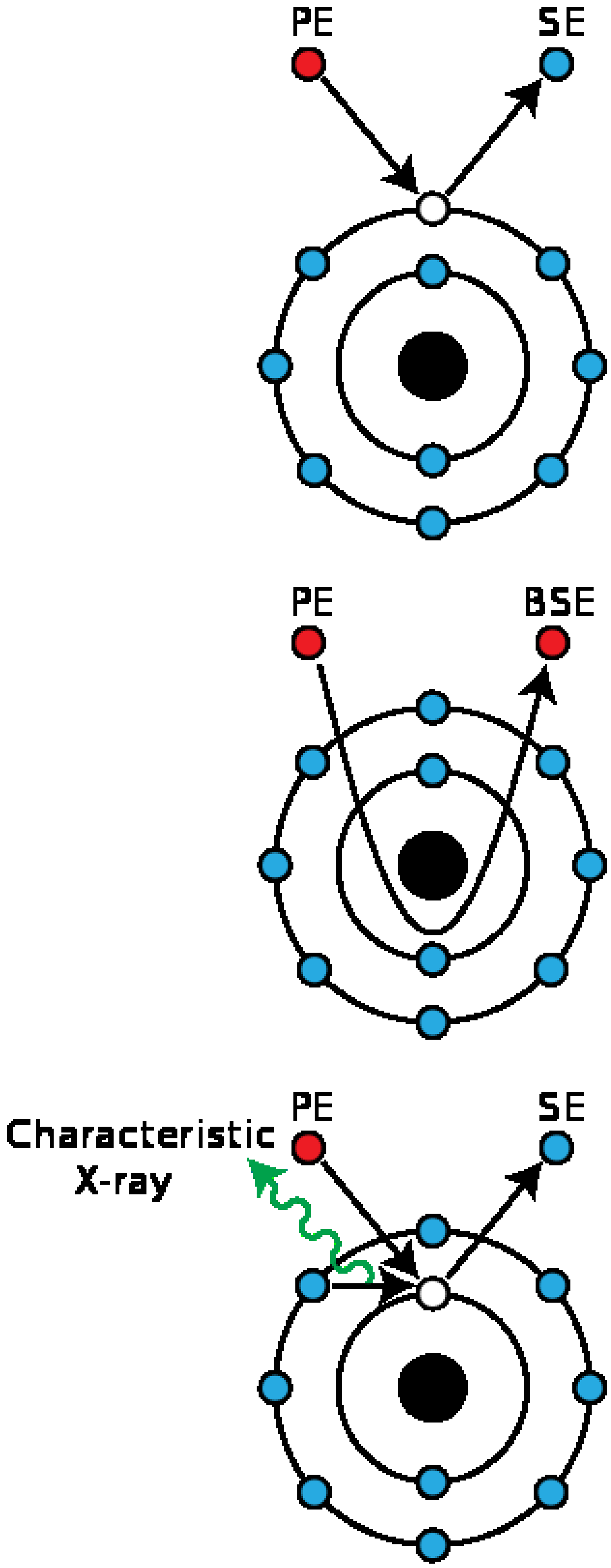

Fig. 3-15: Emission of secondary electron, backscattered electron and characteristic X-ray

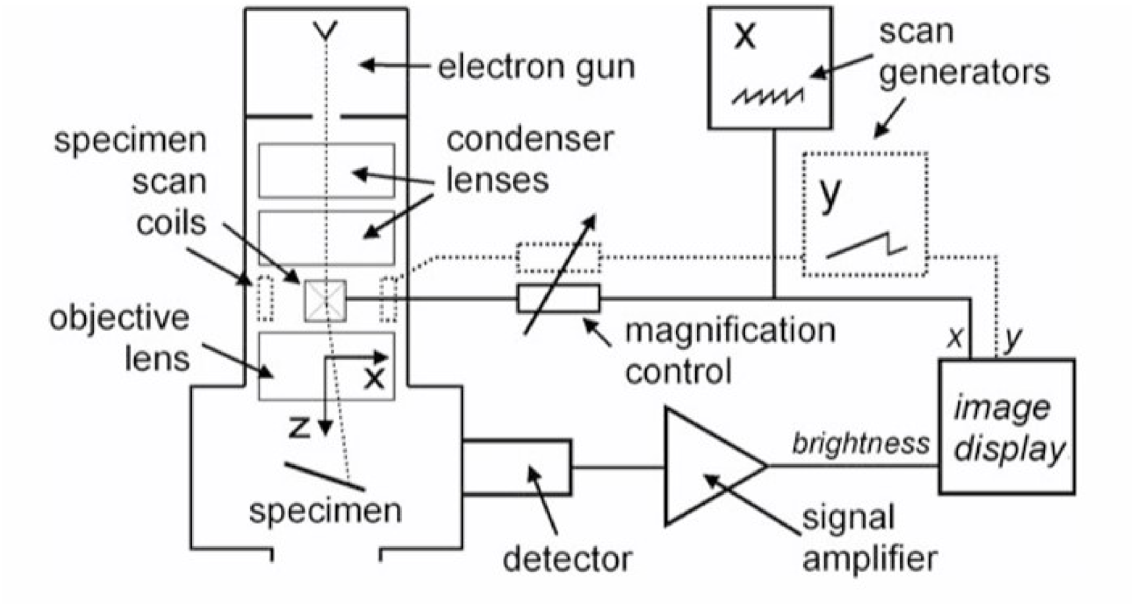

Fig. 3-16: Schematic diagram of a scanning electron microscope

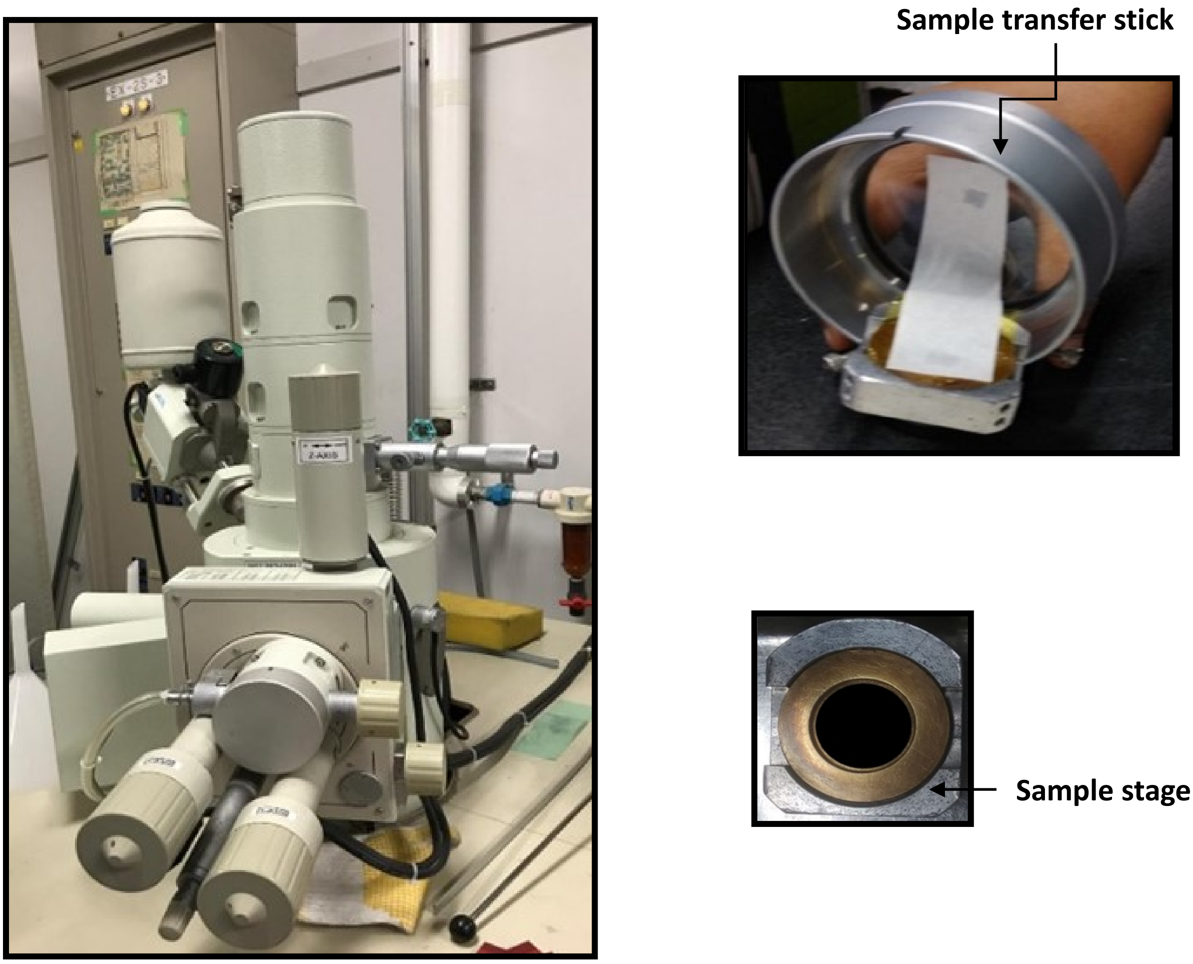

Fig. 3-17: Images of the SEM instrument JEOL JSM 6380 (left); other two images belongs to transfer stick and sample stage

Chapter-4

Improving the kinetics of $2LiBH_4$-MgH_2 system by the addition of potassium hydride (KH) as a catalyst

4-1 Introduction

As we discussed the storage systems in chapter-1 (section:1-8), $2LiBH_4$:MgH_2-RHC specially $2LiBH_4$ + MgH_2 system attracted our attention due to its suitable thermodynamics and sorption properties. To use this system practically, there is still a need to reduce the decomposition temperature which is still over 350°C due to kinetic constraints as reported by different researchers. Potassium hydride has been recognized as one of the magical catalyst, which was first introduced for the improvement of $Mg(NH_2)_2$ – LiH system by Wang et al [29] as discussed in chapter 1. Magical catalytic activities of potassium hydride evoked us to give a trial on the well-known complex hydrogen storage system i.e. $2LiBH_4$-MgH_2. Thus, the effect of KH addition was studied by thermogravimetry coupled with differential thermal analysis (TG-DTA) and differential scanning calorimetry (DSC) in this work. XRD analysis was also performed after milling and heating at 290°C for different compositions of KH in $2LiBH_4$-MgH_2 system.

In this chapter, a comparative study between the $2LiBH_4$-MgH_2 system and $2LiBH_4$-MgH_2 system with 5 mol% KH was presented using TG-DTA and DSC. The next section described the reactive composite $2LiBH_4$-MgH_2 system without KH and with increasing percentage of KH.

4-2 Effect of 5 mol% KH addition on the $2LiBH_4$-MgH_2 system

TG-DTA results of the composite $2LiBH_4$-MgH_2 with and without 5% KH are shown in fig. 4-1. Three endothermic peaks were found in the DTA profile for the $2LiBH_4$-MgH_2 without additives (shown by dashed line in upper panel of fig. 4-1). The first two peaks at 115°C and 285°C belongs to the structural phase transition and melting of $LiBH_4$ respectively. The weight loss was started around 340°C as observed from TG (lower panel, dashed line), which reflected the starting temperature of hydrogen desorption and the corresponding DTA peak was detected at 365°C. The second step decomposition was observed at more than 400°C, which is in line with the literature [61]. On the addition of 5 mol% KH, a shift in desorption temperature was observed for the first step with a peak temperature of 268°C (solid line), while no significant change was observed for the second step decomposition. In addition to it, an unusual but quite interesting phenomenon of shift in melting peak (285°C) was also observed in DTA curve for KH added $2LiBH_4$-MgH_2 system. It is well known that the melting cannot be affected by the use of additive, unless it forms a eutectic mixture. Another possibility can be associated with the occurrence of some unknown irreversible reaction. This observation prompted us to investigate the effect KH addition to this system in more detail. To investigate it more precisely, same samples were examined using DSC and the results are depicted in fig. 4-2. The reversible nature of peak around 285°C confirmed the melting (during heating) and solidification (during cooling), whereas a clear shift to the lower temperature was the testament of eutectic melting. In addition, a small endothermic event was also observed with peak temperature of 110°C, just before the phase transition temperature of

$LiBH_4$. This must be associated with the eutectic melting of eutectic composition. Although the phenomenon of eutectic melting is complicated, we can describe it simply as follows: the eutectic melting happens if two or more components sustain their liquid state below the melting points of their pure components. These eutectic melts can be utilized as media in which substances can dissolve with good solubility. Melting of complex systems like borohydrides and mixture of metal borohydride, hydride and halides can also increase reactivity and can improve kinetics for the release of hydrogen [71],[72]. Lowering melting point, metal borohydrides and complex systems which showed eutectic melting behavior, acted as ionic liquids and can be utilized for refueling of vehicles [73]. Deep eutectic $Mg(BH_4)_2/LiBH_4$ systems in complex borohydrides might behave as liquid in PEM fuel cell which is advantageous in hydrogen reversibility [71]. Many researchers have focused on lowering the eutectic melting points by using the combination of different complex hydride systems due to its excellent onboard application. Bimetallic mixtures have been found to have much lower melting points in comparison with monometallic borohydrides $M(BH_4)x$, where M = Li, Na, K, Mg or Ca [71],[72],[73]. For example, the bimetallic mixture of lithium and potassium borohydrides $0.725LiBH_4$-$0.275KBH_4$ have shown melting point T_m=105°C, which was much lower than the individual borohydride [61]. Similarly, $0.62LiBH_4$-$0.38NaBH_4$ system displayed the melting at 210-220°C [72],[73],[74], lower than the individual components. In case of composite $LiBH_4$-$Ca(BH_4)$ system, it exhibited eutectic melting at 200°C and a partial reversibility has been confirmed for the first time [75]. The $xLiBH_4$-$(1-x)Mg(BH_4)_2$, x = 0.5-0.6 system exhibited a reduced initial temperature of hydrogen release i.e. 180°C (T_m= 180°C) [76]. Thus, to investigate the anticipated similar phenomenon, a series of $2LiBH_4$-MgH_2 with increasing mole percentage of potassium hydride was prepared and was analyzed using differential scanning calorimetry (DSC) in a temperature range of room temperature to 500°C.

4-3 Effect of varying KH content on the $2LiBH_4$-MgH_2 system

Fig. 4-3 shows the DSC profile of samples up to 150°C. The onset temperature has been considered as melting temperature. The compositional details of the prepared samples are given in chapter 3 (Table 3-2). Sample S1 - S4 showed two very close peaks around 110-120°C and one peak in the temperature range 160-235°C. The endothermic peak in higher temperature range corresponded to the melting of the composite mixture and thus it was not very interesting, but the lower temperature peaks were of special interest and these could be assigned to the eutectic melting and phase transition respectively. With the increasing content of KH, the eutectic melting peak height was found to be increasing and shifting slightly to the lower temperature, whereas the peak corresponding to the phase transition was getting modest. The melting peak corresponding to the composite melting was also observed to be shifted to lower temperature. Finally, sample S5 shows only one peak that corresponds to the complete melting thus eliminating the peak corresponding to phase transition of $LiBH_4$, as it was irrelevant in the melted state. Fig. 4-4 shows DSC profiles of some selected samples to determine the lowest melting temperature. The lowest onset temperature was found as 79°C for sample S7 with a composition of $0.45(2LiBH_4$-$MgH_2)$-$0.55(KH)$.

4-4 Phase diagram of x($2LiBH_4$-MgH_2) - (1-x)KH system

All the data corresponding to melting of composite mixtures is plotted in fig. 4-5, which could serve as a phase diagram of x($2LiBH_4$-MgH_2)-(1-x)KH system. Since the melting was not observed for samples S10 - S12, the curve was connected by dashed line, whereas the other part was connected by solid line, which clearly shows the eutectic composition as 0.45($2LiBH_4$-MgH_2)-0.55KH. The line connecting to the melting point of KH and $LiBH_4$ is liquidus line above which both components lies in liquid phase, whereas the horizontal line through the eutectic composition is solidus line. Above the liquidus line both components will be in liquid phase however below the solidus line each composition will be in solid state. We can understand liquidus and solidus as the boundaries between the liquid region and double phase region and solid region and double phase region, respectively. At the eutectic melting point Tm, three phases will coexist i.e. KH in solid state and $2LiBH_4$-MgH_2 in solid state and x($2LiBH_4$-MgH_2)-(1-x)KH in liquid state.

At eutectic melting point:

According to Gibbs phase rule $F = C – P + N$

$N = 1$ (the diagram is plotted for fixed pressure, 1 atm)

$F = C– P + 1$

Number of components, $C = 2$ ($2LiBH_4$-MgH_2 and KH)

Number of phases, $P = 3$

(KH in solid state, $2LiBH_4$-MgH_2 in solid state and x($2LiBH_4$-MgH_2)-(1-x)KH in liquid state)

Degree of freedom $F = C – P + 1 = 2 – 3 + 1 = 0$

This means the point is invariant, i.e. degree of freedom for this point is zero. In this phase diagram, invariant is a point where 3 phases are in equilibrium ($x(2LiBH_4-MgH_2)-(1-x)KH$ in liquid state and KH in solid state, $2LiBH_4-MgH_2$ in solid). However, at the liquidus line let say some point is A (red color) see fig. 4-5 in phase diagram.

At point A:

C = 2

P = 2 (solid $2LiBH_4-MgH_2$ and liquid $2LiBH_4-MgH_2$)F = 1

Therefore, if we know the temperature, the component can be calculated automatically.

4-5 Structural observations after milling and heating

To confirm the above melting and non-occurrence of any other reaction, X-ray diffraction (XRD) was performed for all the samples after milling as well as after DSC experiment up to 290°C. The XRD profiles of selected samples are shown in fig. 4-6. The XRD profile after milling suggested the existence of MgH_2 and $LiBH_4$ phases, however, no peaks corresponding to KH were visible for any samples up to the sample having 70% KH (S10). In addition, some peaks could be indexed for KBH_4 phase for the samples having 60% KH or more (S8-S12). The formation of KBH_4 revealed that the reaction between $LiBH_4$ and KH and anion exchange took place during milling. The formation of amorphous KBH_4 can also be expected for other samples with less KH content. Another possibility of the absence of KBH_4 peaks in XRD of sample S1-S7 can be attributed to the presence of KBH_4 in very small amount, which was not in the detection limit of XRD. This speculation was confirmed from the XRD profile of sample S11 (80%KH), where the peaks corresponding to both phases i.e. KH as well as KBH_4 were present due to the excess amount of KH.

On the other side, for the samples after melting see fig. 4-7, KBH_4 peaks were clearly visible for the S1 sample with only 5% KH. It suggested the crystallization of KBH_4 phase during solidification. The peaks corresponding to MgH_2 along with KBH_4 were also visible in all the samples after heating at 290°C. In addition, the peaks corresponding to potassium hydride were also detected in samples S11 similar to the milled sample.

4-6 Summary

On combining the DSC and XRD data, it was concluded that the melting peak shift to the lower temperature was purely due to melting which arose probably due to the eutectic composition of $LiBH_4$-KBH_4 and no other side reaction took place during the heating range. Eutectic melting in $LiBH_4$- KBH_4 has already been investigated by L.B. Morten group in 2014 [74] and the lowest eutectic temperature was reported as 105°C. In our case we observed the lowest temperature as 79°C, which is different from the above, however, it might be associated with the different starting materials and/or different measuring method (TPPA in the above report, while DSC in this work). The effect of KH as a catalyst for the first decomposition step of the above system can also be understood on the basis of this eutectic melting. Since KH reacted with $LiBH_4$ during the milling process, it changed to KBH_4 which formed a eutectic composition with $LiBH_4$, thus reducing the melting temperature of the above system. The ionic mobility was enhanced due to the weakening of Li-B-H bonding in the molten state of $LiBH_4$, thus enhancing the sorption kinetics and reducing the decomposition temperature of first step reaction which corresponded to the $LiBH_4$ decomposition.

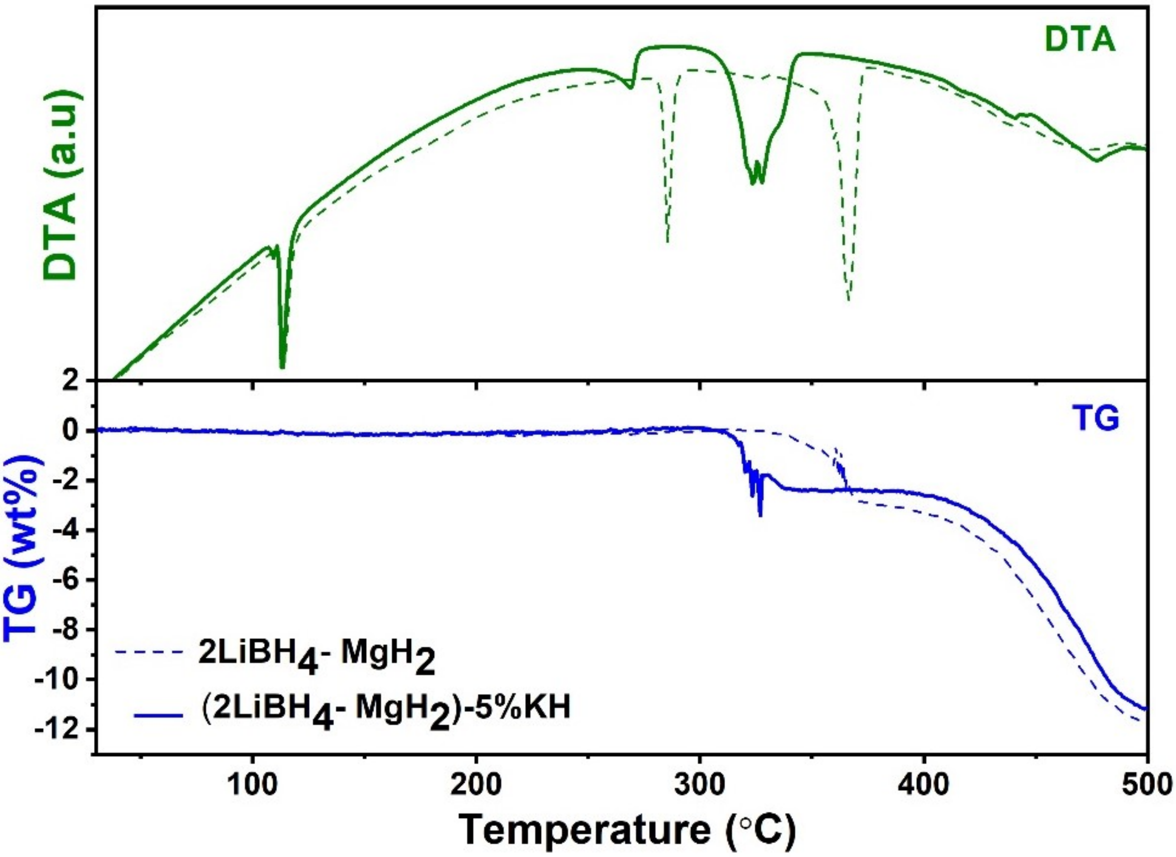

Fig. 4-1: DTA (upper panel) and TG analysis (lower panel) of $2LiBH_4$-MgH_2 (dashed lines) and $2LiBH_4$-MgH_2 - 5%KH (solid lines)

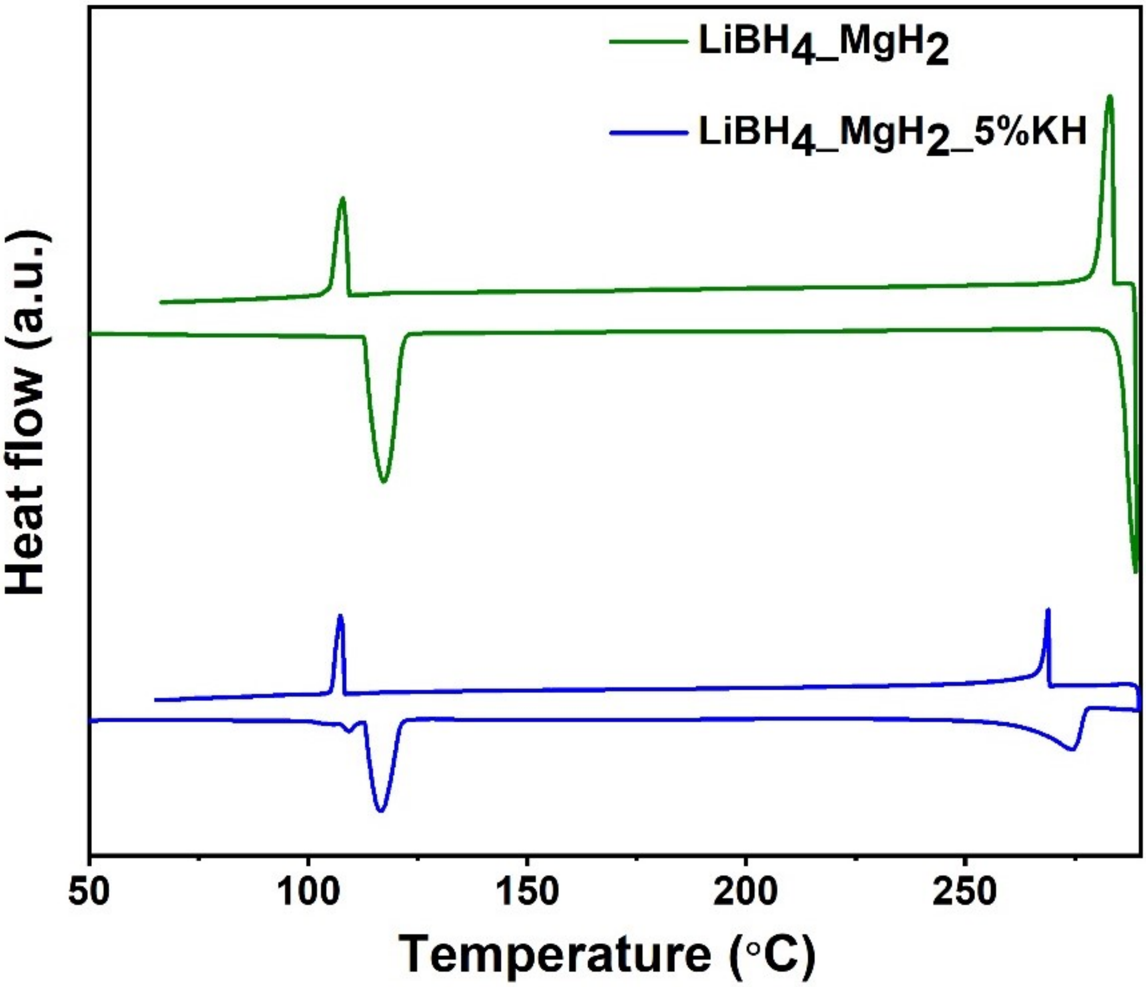

Fig. 4-2: DSC profile of pure (green color) and 5 mol% KH added $LiBH_4$-MgH_2

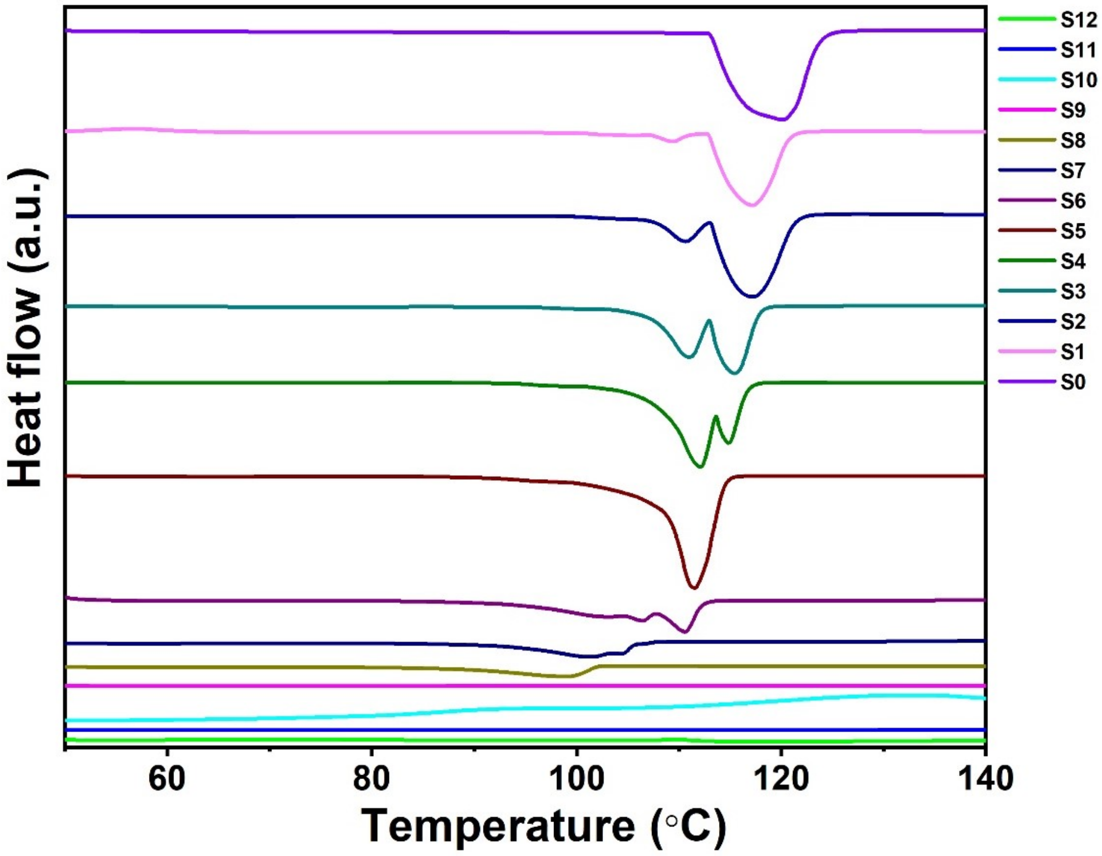

Fig. 4-3: DSC curves for pure $2LiBH_4$-MgH_2 (first from upwards) and with the different potassium hydride content. S0 is the sample $2LiBH_4+MgH_2$ without addition of KH i.e. 0% KH $2LiBH_4+MgH_2$, S1 is $2LiBH_4+MgH_2$ with 5mol%KH, S2 is $2LiBH_4+MgH_2$ with 10mol%KH, S3 is $2LiBH_4+MgH_2$ with 20mol%KH, S4 is $2LiBH_4+MgH_2$ with 30mol%KH, S5 is $2LiBH_4+MgH_2$ with 40mol%KH, S6 is $2LiBH_4+MgH_2$ with 50mol%KH, S7 is $2LiBH_4+MgH_2$ with 55mol%KH, S8 is $2LiBH_4+MgH_2$ with 60mol%KH, S9 is $2LiBH_4+MgH_2$ with 65mol%KH, S10 is $2LiBH_4+MgH_2$ with 70mol%KH, S11 is $2LiBH_4+MgH_2$ with 80mol%KH, S12 is $2LiBH_4+MgH_2$ with 90mol%KH (See the table 3-2 in chapter 3 for detailed information about samples from S0 to S12)

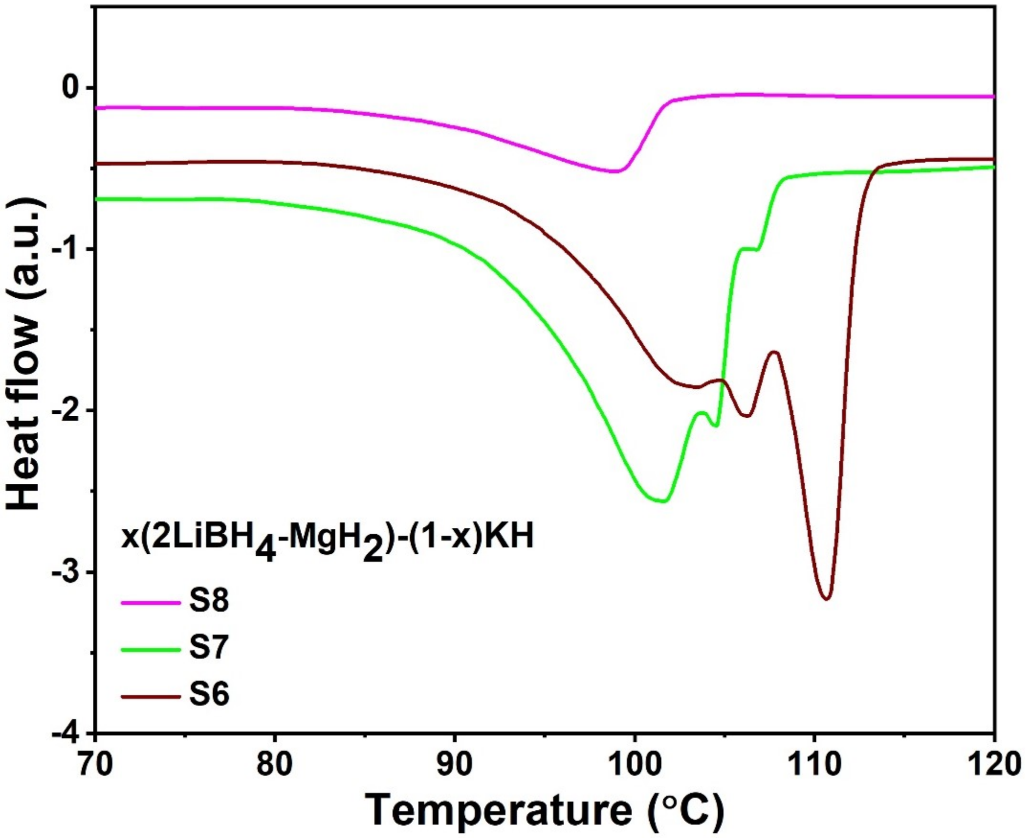

Fig. 4-4: DSC profiles of selected KH added $2LiBH_4$-MgH_2 samples. S6 is $2LiBH_4$+MgH_2 with 50mol%KH, S7 is $2LiBH_4$+MgH_2 with 55mol%KH, S8 is $2LiBH_4$+MgH_2 with 60mol%KH. Lowest melting onset peak was found for S7.

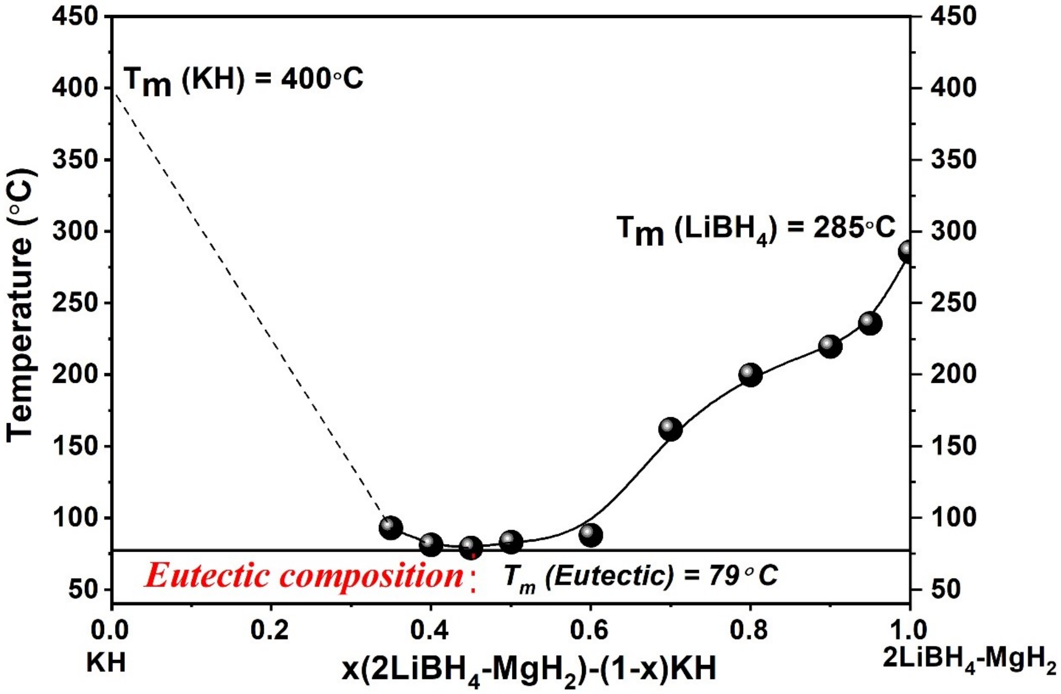

Fig. 4-5: Phase diagram of x(2$LiBH_4$-MgH_2)-(1-x)KH system

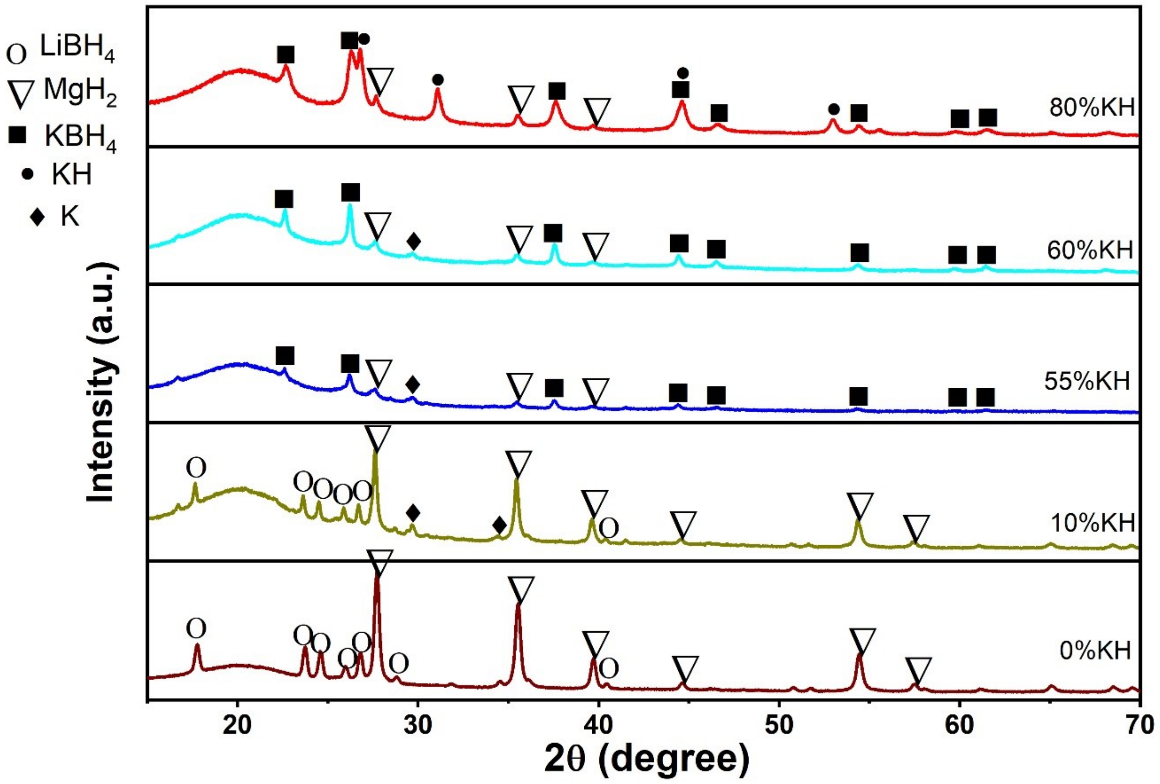

Fig. 4-6: XRD patterns of selected samples after milling

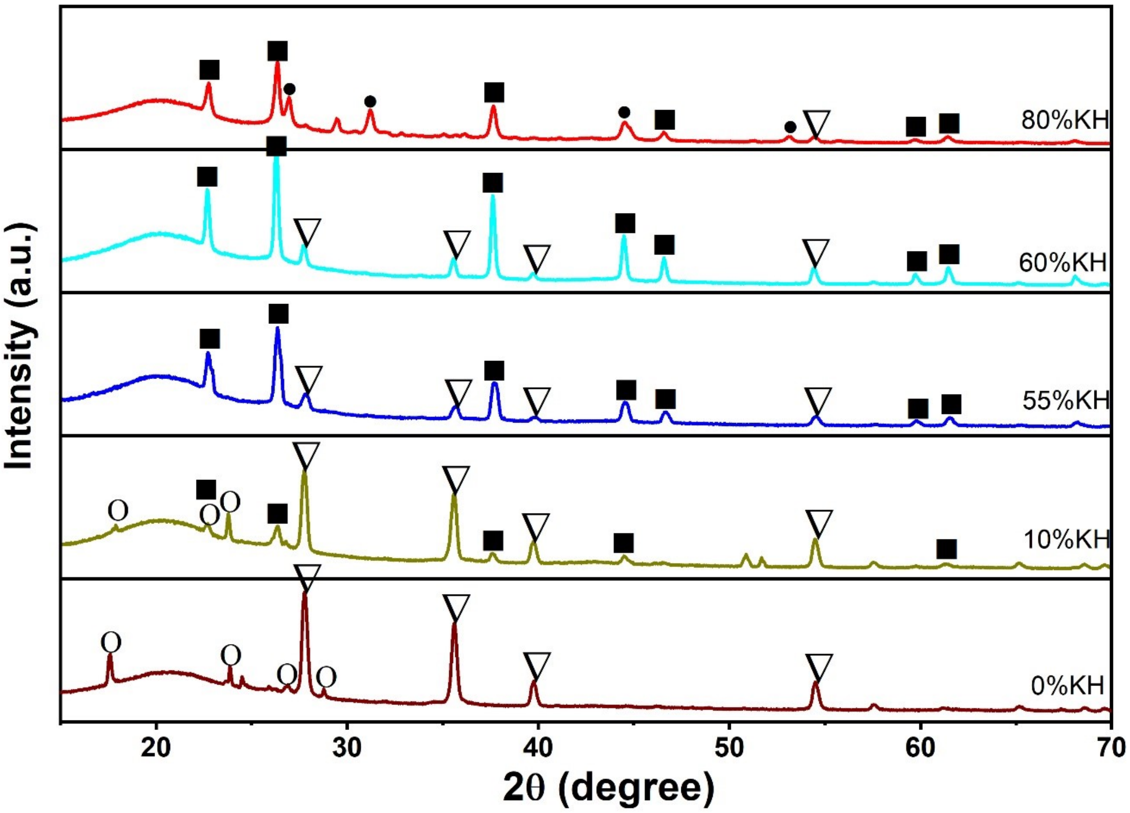

Fig. 4-7: XRD patterns of selected samples after heating

Chapter-5

Destabilization of $LiBH_4$ by the infusion of Bi_2X_3 (X = S, Se, Te): Structural and Morphological Investigation

5-1 Introduction

This chapter covers our second objective of this thesis, i.e. focus on decomposition properties of $LiBH_4$ by the addition of Bi_2X_3 chalcogenides. Structural and morphological characterizations like XRD and TEM have been performed for all the prepared bulk and nanostructures and their composites with $LiBH_4$ to understand the reaction mechanism. TG-DTA connected with MS was used to investigate the thermal profile of the bulk and nano Bi_2X_3 mixed $LiBH_4$. Finally, a reaction mechanism was established for these composites.

5-2 Dehydrogenation of $LiBH_4$ – bulk Bi_2X_3 composites

The TG-DTA and MS profiles with heating rate 5°C/min in fig. 5-1, 5-2 and 5-3, show the hydrogen desorption properties of heated $LiBH_4$ mixed with bulk commercial samples of Bi_2X_3 (X=S, Se and Te). DTA profiles of all three composites showed endothermic peaks at 117°C and 283°C corresponding to the phase transition and melting respectively. A tiny signal corresponding to diborane was also observed in all the mass spectra which is negligible to consider. The observations confirmed that the onset dehydrogenation temperature was significantly reduced from 450°C for pristine $LiBH_4$ to 75°C in case of $LiBH_4$ - 50wt% bulk Bi_2S_3. The MS profile of $LiBH_4$-Bi_2S_3 composite (fig. 5-1) suggested 3 major steps for decomposition with the onset temperature at 75°C, 340°C and 445°C. A weight loss of 7.2wt.% was observed in first step followed by 3.3 and 2.1% in second and third step respectively (TG profile in fig. 5-1). Fig. 5-2 shows the decomposition profile of $LiBH_4$ - 50wt% bulk Bi_2Se_3. The first step decomposition could be started at 145°C with weight loss of 3.7wt.%. The onset of second and third step was quite similar to that of Bi_2S_3 composite i.e. 340°C and 432°C respectively, however the ending temperature of second step was found slightly different. A total of 5.2wt% hydrogen was desorbed in these steps up to 500°C. The $LiBH_4$ - 50% bulk Bi_2Te_3 composite was also investigated by TG-MS to study the thermal behaviors of the sample (fig. 5-3). The hydrogen sorption could be started at 185°C and a total of 2.76 wt% hydrogen was released during first step reaction with a minute amount of B_2H_6, similar to other two cases. Second and third step reactions were observed to start at same temperature as of Bi_2S_3 and Bi_2Se_3 based composites. A total weight loss of 5.24% was observed in the second and third step of reaction up to 500°C. A total amount of 8 wt.% hydrogen was liberated from $LiBH_4$-50 wt% Bulk Bi_2Te_3. To understand the reaction mechanism of above, XRD analysis was performed at different temperatures according to MS profile. In addition, a fluctuation around 280°C (the melting point of $LiBH_4$) in all the TG profiles was visible, which might be associated to the buoyancy effect [77],[78],[33], commonly observed in borohydrides decomposition. Since the temperature of second and third peak for all the three composites was found same, these were believed to correspond the same type of reactions.

Although all the 3 composites showed a reduced decomposition temperature compared to $LiBH_4$, the onset temperature was still higher than it was observed in case of nano-Bi_2Te_3 [58]. This must be associated with the kinetic limitation. It is well known that nanomaterials and nanostructures affect the kinetics of hydrogen absorption and dissociation by decreasing the needed diffusion length or by increasing the diffusion rate [79].

5-3 Nanostructures characterizations: SEM and TEM analysis

To understand the effects of nanostructures on hydrogen desorption properties, we first characterized them by FESEM and TEM. The FESEM image as shown in fig. 5-4 (a) suggested that the Bi_2S_3 nanoflowers were grown in large quantity and consisted of nanorods like leaf structure. The diameter of nanorods was assigned in the range of 10-150 nm whereas length varied in the range of 150-400 nm. All samples were characterized by TEM also to validate the nanostructures which confirmed a flower like structure, as shown in fig. 5-4 (b). Fig. 5-4 (c) depicted the spot diffraction pattern recorded by SAED which indicated the polycrystalline structure of Bi_2S_3 nanoflowers. Fig. 5-4 (d) shows the HRTEM image of Bi_2S_3 nanoflowers, in which the HRTEM image of selected area indicated the d-spacing of 0.51nm corresponding to (120) plane of Bi_2S_3 structure. Fig. 5-5 shows the morphology of Bi_2Se_3 nanostructures. The nanosheets of Bi_2Se_3 are shown by TEM observation in Fig. 5-5 (a). The uniform sheets of 50-100 nm sizes were widely distributed over the surface as can be seen by FE-SEM image in Fig. 5-5 (b). The bright spots in Fig. 5-5 (c) indicated the crystallinity of sample by SAED pattern. Interplanar distance was depicted as 0.34 nm for the plane (012) of selected area in HRTEM image (fig. 5-5 d). Fig. 6 shows the morphological characterization for Bi_2Te_3 nanostructures. The high-resolution FE-SEM showed sheets like structures for Bi_2Te_3 as shown in fig. 5-6 (a). TEM experiment as shown in fig. 5-6 (b) also confirmed the sheets structures of as prepared sample of Bi_2Te_3. Selected area electron diffraction pattern clearly indicated the crystalline sample of Bi_2Te_3 see in fig. 5-6 (c) with an interplanar spacing as 0.21 nm (fig. 5-6 d) which corresponds to (113) plane of Bi_2Te_3 structure.

5-4 Effect of nanostructured Bi_2X_3 on decomposition properties of $LiBH_4$

Nanostructures have been defined as new art of energy storage which can give different routes and new opportunity in the field of solid - state hydrogen storage [80],[81],[82]. Due to the immense sake we switched towards nanostructures of Bi chalcogenides [83],[84],[85]. The TG-MS profile for all the 3 composites with nanostructured Bi_2X_3 are shown in fig. 5-7 (a) and 5-7 (b). The total weight loss for all the composites was found quite similar to the composites having bulk Bi_2X_3, however, the MS profile showed multiple peaks. This must be due to the presence of kinetic active and inactive part of the composites. The enhancement is clear from fig. 5-7 (c – e) where a comparison of MS profile for bulk and nanostructure-based composites is shown. A shift in the MS peaks to lower temperature can clearly be seen for the composites with nanostructures. It is noteworthy here that the onset temperature for 1st step for all the composites was drastically reduced, which clearly suggested a kinetic enhancement. Table 5-1 also shows a comparison of minimum temperature achieved for the decomposition in bulk and nanostructures of all samples. The lowest onset temperature of 50℃ could be achieved for composite having Bi_2S_3 nanoflowers. In summary, it can be concluded that the addition of bulk Bi_2X_3 destabilize $LiBH_4$ thermodynamically, however a kinetic barrier still exists. A further reduction in the decomposition temperature could be achieved by the kinetic enhancement by the use of nanostructures which can be dispersed throughout the surface more homogeneously and make good contact with $LiBH_4$ and provided better diffusion path for hydrogen liberation.

Table 5-1 Onset desorption temperature of $LiBH_4$ mixed with bulk and nanostructured Bi_2X_3

	Onset temperature (°C)	
	$LiBH_4$ – 50 wt% bulk Bi_2X_3	**$LiBH_4$ – 50 wt% nano Bi_2X_3**
$LiBH_4$ – 50% Bi_2S_3	75	50
$LiBH_4$ – 50% Bi_2Se_3	145	60
$LiBH_4$ – 50% Bi_2Te_3	185	75

5-5 XRD analysis of $LiBH_4$ – 50wt% Bi_2X_3 composites at different decomposition steps

The phase compositions of all three samples i.e. $LiBH_4$ mixed with 50wt% Bi_2S_3, 50wt% Bi_2Se_3 and 50wt% Bi_2Te_3 were investigated by XRD. The XRD profile of $LiBH_4$ - 50% Bi_2S_3, shown in the bottom panel of fig. 5-8 suggests that a mechanochemical reaction between the components of composites took place during milling as evidenced from the presence of Bi peaks in addition to the starting material Bi_2S_3. The peaks corresponding to $LiBH_4$ could not be observed due to low scattering factor of $LiBH_4$ in comparison to the other phases in the composite. From the presence of Bi phase, we expect the formation of Li_2S also however the peaks corresponding to Li_2S was at the same position as of other phases. So, it was difficult to differentiate them, however these were also indexed in the diffractogram. In contrast to $LiBH_4$ – 50wt% Bi_2S_3, the XRD data of $LiBH_4$ – 50wt% Bi_2Se_3 (fig. 5-9, bottom panel) and $LiBH_4$ – 50wt% bulk Bi_2Te_3 (fig. 5-10, bottom panel) confirmed the presence of both counterparts of composites, thus suggesting no reaction between them.

To reveal the reaction mechanism of $LiBH_4$-50wt% bulk Bi_2X_3 composites, structural characterization was performed by collecting the XRD patterns after heating to various temperatures according to TG experiment. Fig. 5-8 shows the XRD patterns for Bi_2S_3 composites, where mainly bismuth peaks were observed for the sample heated up to 220°C after the first step reaction between $LiBH_4$ and Bi_2S_3. The other expected phases i.e. Li_2S and $LiBH_4$ could not be observed probably due to the low scattering factor of $LiBH_4$ and Li_2S in comparison to Bi or due to less crystallinity ratio of these phases in comparison to Bi. However, the presence of $LiBH_4$ could be confirmed from the DTA profile (fig. 5-11) of composite up to 300°C, where the profile during cooling showed the exothermic peaks at 273°C and 102°C corresponding to solidification and phase change of $LiBH_4$ respectively. Further heating up to 340°C didn't change the XRD profile much except the presence of small peaks corresponding to LiBi phase which suggested further decomposition of $LiBH_4$ in a small extent and corresponded to very small weight loss in the temperature range of 270 to 340°C. In the next step of reaction (heated up to 445°C) $LiBH_4$ further reacted with Bi and LiBi to form Li_3Bi which can be clearly seen from the XRD spectra for the sample heated up to 445°C. Further heating to 500°C didn't change the XRD spectra, however, a weight loss was observed in TG profile as well as a MS peak corresponding to H_2 evolution could be seen. This step must be due to the remaining excess $LiBH_4$, which directly decompose in to Li, B and H_2 as reported in literature [86]. It is to be noted here that the weight ratio of $LiBH_4$ and Bi_2X_3 was decided as 50:50 to keep the ratio almost same as that for electrode composite material in our earlier report [58]. However, according to XRD results, less amount of $LiBH_4$

should be added to exclude the third step i.e. direct decomposition of $LiBH_4$, which needs high temperature (>450°C). The expected reaction according to the products (as evidenced from XRD) can be written as:

$$12\ LiBH_4 + Bi_2Se_3 \rightarrow 2Li_3Bi + 3Li_2Se + 12B + 24H_2$$

To examine the above reaction, a new composite with above ratio was prepared in a similar way and the decomposition pathway was evaluated using TG-DTA-MS. The TG-DTA-MS profile (fig. 5-12) showed similar decomposition peaks, however, a significant amount of diborane was obtained during first step reaction around 150°C. Since the diborane evolution has been considered as unwanted due to the loss of reversibility, it was concluded here that excess amount of $LiBH_4$ was necessary to suppress the diborane evolution. This was the reason other composites were continued with the 50:50 weight ratio of $LiBH_4$ and Bi_2X_3 for further studies. Fig. 5-9 shows the XRD patterns for $LiBH_4$-50 wt% bulk Bi_2Se_3 composite at different steps. The XRD pattern after first step desorption (235°C) could be indexed by bismuth (Bi) and lithium selenide (Li_2Se) phases. Near the melting point of $LiBH_4$ (280°C), a very small weight loss was observed, however, no significant change was observed in the XRD profile for the samples heated up to 325°C. Further heating to high temperature gave rise to Li_3Bi phase as observed in the XRD pattern for the sample heated up to 430°C. No further changes in XRD pattern were found on increasing temperature up to 500°C, which again confirmed the decomposition of remaining excess $LiBH_4$. For the understanding of dehydrogenation process of $LiBH_4$-50 wt% bulk Bi_2Te_3, the solid residues at different heating stages were collected to get the XRD pattern and these are shown in fig. 5-10. Bismuth and lithium telluride (Li_2Te) phases were the phases after the first step of dehydrogenation (250°C) that is obvious to observe due to the reaction between $LiBH_4$ and Bi_2Te_3. The heating up to 330°C didn't change the XRD profile at all. On high heating stage i.e. second step desorption (XRD at 425°C), Li_3Bi peaks were detected in addition to Li_2Te, indicating the further reaction between bismuth and unreacted $LiBH_4$. Similar to the case of Bi_2S_3 and Bi_2Se_3 composites, further heating to 500°C releases hydrogen without changing the XRD profile, which again suggested the decomposition of excess $LiBH_4$.

5-6 In-situ TEM observation of $LiBH_4$-nano Bi_2X_3 composites

To confirm the XRD results, in-situ TEM observation were made on $LiBH_4$-nano Bi_2X_3 composites after milling and heating at various temperatures. A SADP (selected area diffraction pattern) technique was used to identify the different phases in as prepared $LiBH_4$-nano Bi_2X_3 composites and the results were shown in fig. 5-13 to 5-18. Marked positions (spots 1 and 2) by red color numbered circles were the selective aperture for TEM analysis for different diffraction patterns. Fig. 5-13 shows the bright field images at different spots with the corresponding diffraction patterns for as prepared samples after milling as well as after heating at different temperatures. The diffraction patterns a, b, c, d and e are corresponding to spot 1 as shown in the image. The phase identification and corresponding d-spacing are summarized in table attached in fig. 5-13 (a) shows the diffraction pattern of $LiBH_4$-50% Bi_2S_3 nanostructures after milling at room temperature. The d-spacing confirmed the presence of Bi_2S_3. However, it was difficult to find $LiBH_4$ due to its instability under the high energy electron beam. In addition to Bi_2S_3, Bi was also observed. The finding is in line with the XRD results as shown in fig. 5-8, where the presence of Bi and Li_2S was observed in addition to the main phases of $LiBH_4$ and Bi_2S_3. On heating the sample up to 50°C, in-situ

TEM suggested the presence of LiBi and Li_2S in addition to the Bi_2S_3 phase (fig. 5-13 b). The formation of LiBi at this temperature is surprising as this phase was appeared only after ex-situ heating at 340°C. Thus, it was believed that the high energy electron beam transferred the energy to the composite and decompose $LiBH_4$ to form LiBi. It could be confirmed from the in-situ TEM experiment at 150°C (fig. 5-13 d) and 200°C (fig. 5-13 e), where the diffraction pattern could be indexed by LiBi as well as Li_3Bi phases. This Li_3Bi phase could be observed only at beyond 440°C (fig. 5-8) during ex-situ heating. On observing the TEM images (fig. 5-14) and the respective EDS analysis, it was observed that $LiBH_4$ and Bi_2S_3 were mixed completely after milling and it was difficult to distinguish them from the contrast in TEM image. However, with heating, the Bi and S containing species were clustered into small islands within the sea of boron containing species. Since the composites were very sensitive to the electron beam, ex-situ study was performed for the other samples at higher temperature. The samples were heated up to 450°C inside the TEM chamber, however the electron beam was turned off during heating. After heating the sample, the sample was cooled down to RT and the TEM experiments were performed at the same spot.

Fig. 5-15 shows bright field images of TEM corresponding to $LiBH_4$-50% Bi_2Se_3 nanostructures after milling (upper panel) and after heating (lower panel). The diffraction pattern corresponding to spot 1 and 2 are shown in fig. 5-15 a and b respectively (see table attached with fig. 5-15). At spot 1, the diffraction pattern could be indexed to Bi, Li_2Se and Bi_2Se_3. The presence of Bi_2Se_3 as starting material was quite reasonable and in agreement with the XRD results (fig. 5-9), whereas, the presence of Bi and Li_2Se was observed only at micro level, which could be caused due to decomposition by the electron beam during TEM experiment. The diffraction pattern after heating up to 450℃ (measured after cooling down the sample to room temperature) could be indexed by Li_2Se, LiBi and Li_3Bi phases, which confirmed the formation of Li_3Bi and Li_2Se and the decomposition of $LiBH_4$. Similar to the $LiBH_4$-Bi_2S_3 composite, the same tendency of island formation was also observed here (fig. 5-16). The TEM micrographs and corresponding SAED patterns of $LiBH_4$-50% Bi_2Te_3 nanostructures are shown in fig. 5-17. The composite after milling showed the existence of Bi_2Te_3 phase. In addition, Li_2Te phase could also be observed, which suggested the reaction between $LiBH_4$ and Bi_2Te_3. It is in contrast to the XRD finding (fig. 5-10), thus it must be caused by the electron beam during TEM measurement. However, according to the above reaction the expected phase of Bi could not be detected. In TEM bright field images, the dark color part represents the Bi and Te rich phases as confirmed from EDS analysis (fig. 5-18). In the milled sample this dark color part exists as a lump with $LiBH_4$ rich phase on its boundary. On heating the sample to high temperature, $LiBH_4$ started diffusing through Bi_2Te_3 and reacted with it. This reaction turned the initial lump of Bi and Te rich phase into several small island floating in the boron rich phase sea. Thus, the reaction mechanism was found quite similar for all the three composites.

5-7 Discussion and reaction mechanism establishment

On combining the TG, XRD and TEM results for these composites at each step of dehydrogenation, it is clear that the second and third steps are quite similar for each composite. The second step dehydrogenation was resulted from Bi and $LiBH_4$ reaction which promoted Bi → Li_3Bi conversion, whereas the third step dehydrogenation was occurred due to direct decomposition of excess $LiBH_4$. The temperature and weight loss corresponding to first step reaction were found different for all the composites. The first step weight loss for $LiBH_4$ - Bi_2S_3 composite was much larger (~7.2 wt%) than what can be expected due to hydrogen release only. Thus, it can be speculated that there must be some other gaseous species which were lost during the reaction. There are two possibilities which can take place during this reaction: (i) loss of sulphur, as the melting point of sulphur is 115.2℃; (ii) loss of H_2S. Hence, it was difficult to decide the exact reason for this excess weight loss and making it difficult to establish the reaction pathway for $LiBH_4$-Bi_2S_3 composite. So, this composite was kept on hold for a while and the other two composites were taken in to account. On combining TG, XRD and TEM results for the other two composites based on Bi_2Se_3 and Bi_2Te_3, following reactions for each composite can be suggested:

$$30LiBH_4+Bi_2Se_3 \rightarrow 3Li_2Se+2Bi+16LiBH_4+8LiH+14B+24H_2 \quad \text{(1st step)}$$

$$\rightarrow 2Li_3Bi+8LiBH_4+4LiH+8B+18H_2 \quad \text{(2nd step)}$$

$$\rightarrow 8Li+6B+16H_2 \quad \text{(3rd step)}$$

and

$$38LiBH_4+Bi_2Te_3 \rightarrow Li_2Te+2Bi+25LiBH_4+7LiH+12B+22.5H_2 \quad \text{(1st step)}$$

$$\rightarrow 2Li_3Bi+17LiBH_4+2LiH+8B+15H_2 \quad \text{(2nd step)}$$

$$\rightarrow 13LiH+4Li+17B+27.5H_2 \quad \text{(3rd step)}$$

The above reactions are well fitted according to the weight loss as well as XRD results. As per the analogy to these systems, sulphur should also react with $LiBH_4$ to desorb hydrogen from $LiBH_4$ - Bi_2S_3 composite. Sulphur cannot remain in the elemental form thus ruled out the possibility of sulphur loss (first possibility for the larger weight loss in first step as discussed above). Moreover, this was also confirmed visually after opening the TG chamber after first step reaction, where no sign of melting was observed. On the other hand, there is equal possibility of forming H_2S in addition to Li_2S during the reaction of Bi_2S_3 with $LiBH_4$. However, no MS peak for H_2S was observed during first step (fig. 5-1 and fig. 5-12). The absence of H_2S - MS signal might be caused by the decomposition of H_2S in to H_2 and S during the transfer of H_2S gas from TG chamber to MS chamber through capillary, which was kept at 200°C. Since H_2S is unstable gas at high temperature and easy to decompose even at room temperature in presence of metal catalyst [87],[88],[89] the above speculation is quite reasonable to justify larger weight loss according to the following reaction:

$$
\begin{aligned}
24LiBH_4+Bi_2S_3 &\rightarrow 1.2Li_2S+1.8H_2S+2Bi+18.5LiBH_4+3LiH+5.5B+7.5H_2 && \text{(1st step)}\\
&\rightarrow 2Li_3Bi+9.5LiBH_4+3LiH+9B+16.5H_2 && \text{(2nd step)}\\
&\rightarrow 9.5LiH+9.5B+14H_2 && \text{(3rd step)}
\end{aligned}
$$

It is clear from above that hydrogen desorption took place at significantly lower temperature. The onset temperature for all the composites was found less than 100°C, which is quite interesting for hydrogen storage application. On the other hand, it is much lower than the operating temperature of coin cell (this must be the reason of coin cell opening during electrochemical operation) in our previous work [58]. Thus, it can be concluded that such a lower desorption temperature of these composites restricted the potential window and affected the cyclic stability of these electrode materials drastically. To resolve this issue, these composite materials should be operated at lower temperature for which $LiBH_4$ should be replaced by some other electrolytes which are capable to work at lower temperature. It can be achieved by making composite of $LiBH_4$ also, so that the high temperature phase of $LiBH_4$ can be stabilized at room temperature [90]. This will prevent the thermochemical reaction between Bi_2X_3 and $LiBH_4$ during electrochemical operation of coin cell and may enhance the capacity as well as the cyclic stability further.

5-8 Summary

In summary, the present work clarified that nanostructures Bi_2S_3 had not only shown excellent properties for destabilization of $LiBH_4$ at low temperature but also clarified the side reaction appeared during their electrochemical charging-discharging in all-solid-state Li-ion battery. The onset desorption temperature of $LiBH_4$ was thermodynamically lowered down to 75°C by the addition of bulk Bi_2S_3. A further reduction in the onset temperature 50°C could be achieved by the use of Bi_2S_3 nanoflowers due to kinetic enhancement. However, reversibility could be obtained in case of Bi_2Se_3 and Bi_2Te_3 because no other gases except H_2 has been evolved during heating. While in case of Bi_2S_3 other gases like H_2S was suspected to be desorbed during heating process. Considering reversibility, Bi_2Se_3 nanostructures had shown the lowest decomposition temperature 60°C while adding with $LiBH_4$.

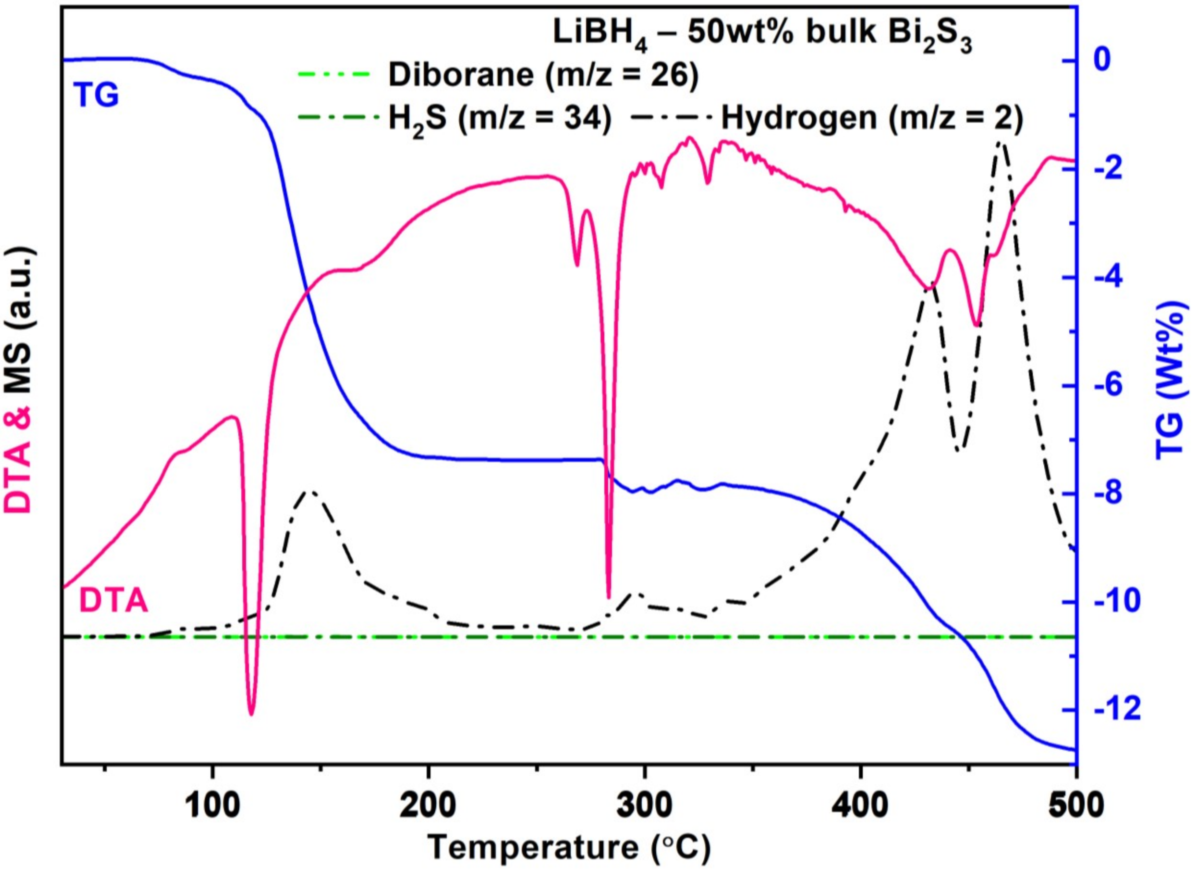

Fig. 5-1: TG-DTA and MS profile of milled LiBH$_4$ – 50wt% bulk Bi$_2$S$_3$

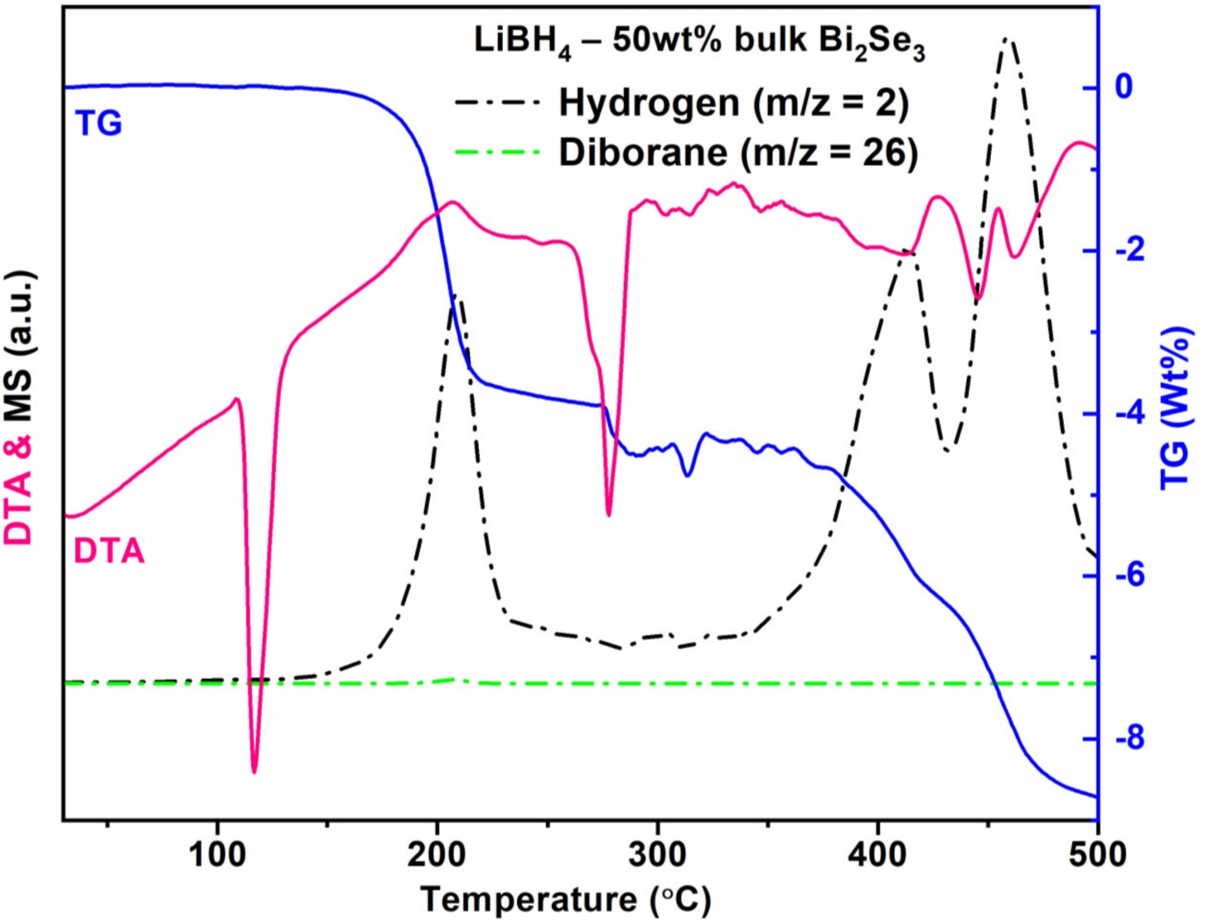

Fig. 5-2: TG-DTA and MS profile of milled LiBH$_4$ – 50wt% bulk Bi$_2$Se$_3$

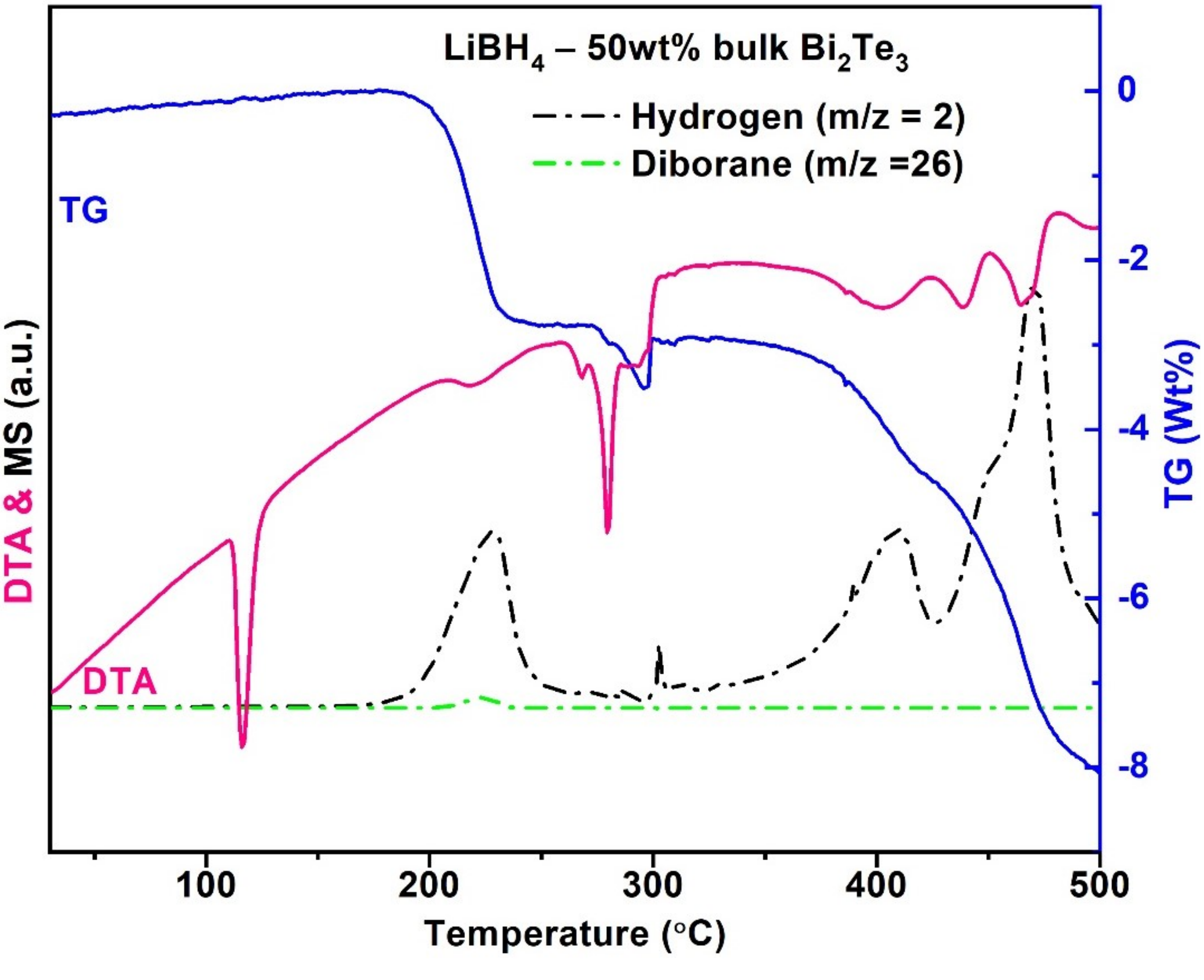

Fig. 5-3: TG-DTA and MS profile of milled LiBH$_4$ – 50wt% bulk Bi$_2$Te$_3$

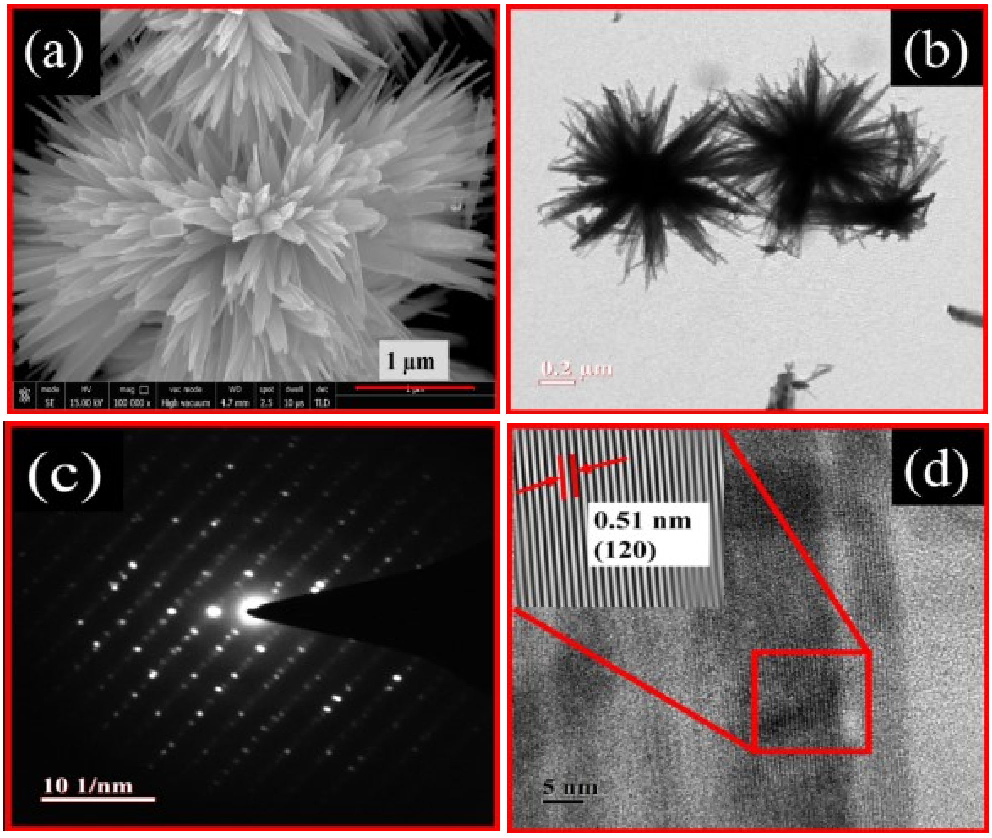

Fig. 5-4: FE-SEM & TEM images of Bi$_2$S$_3$ nanoflowers (a & b), SAED & HRTEM images of nanoflowers (c & d)

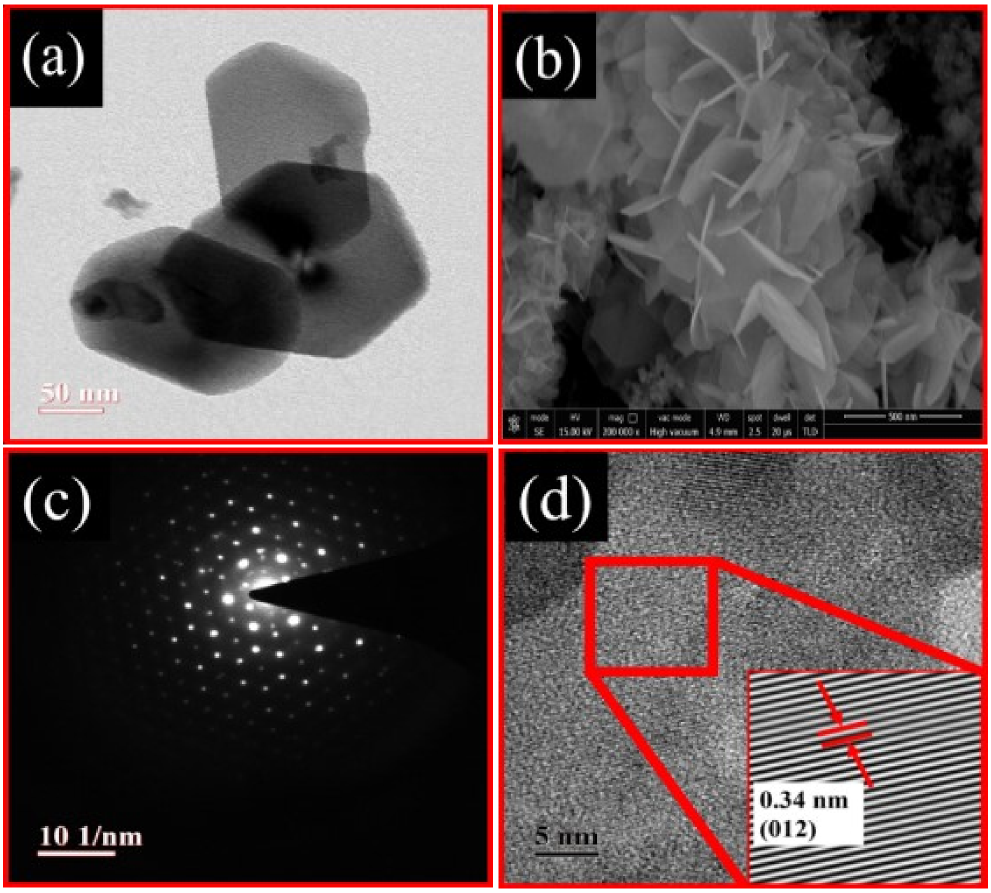

Fig. 5-5: TEM & FE-SEM images of Bi_2Se_3 nanosheets (a & b), SAED & HRTEM images of Bi_2Se_3 nanosheets (c & d)

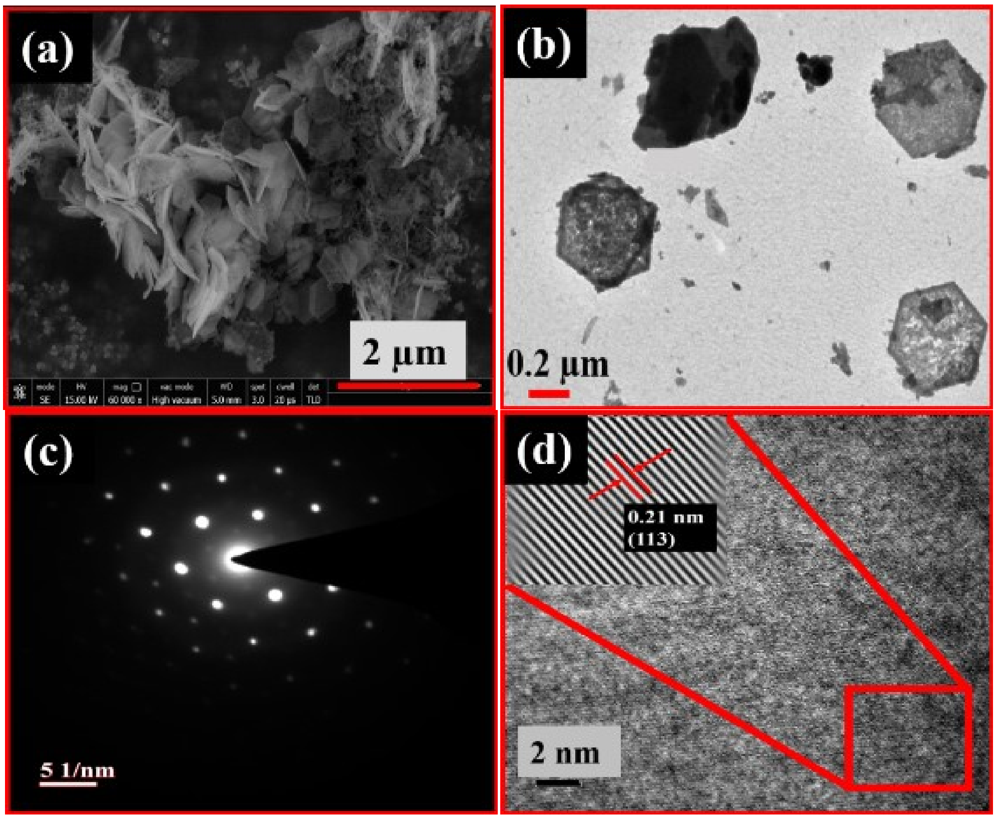

Fig. 5-6: FE-SEM & TEM images of Bi_2Te_3 nanosheets (a & b), SAED & HRTEM images of Bi_2Te_3 nanosheets (c & d)

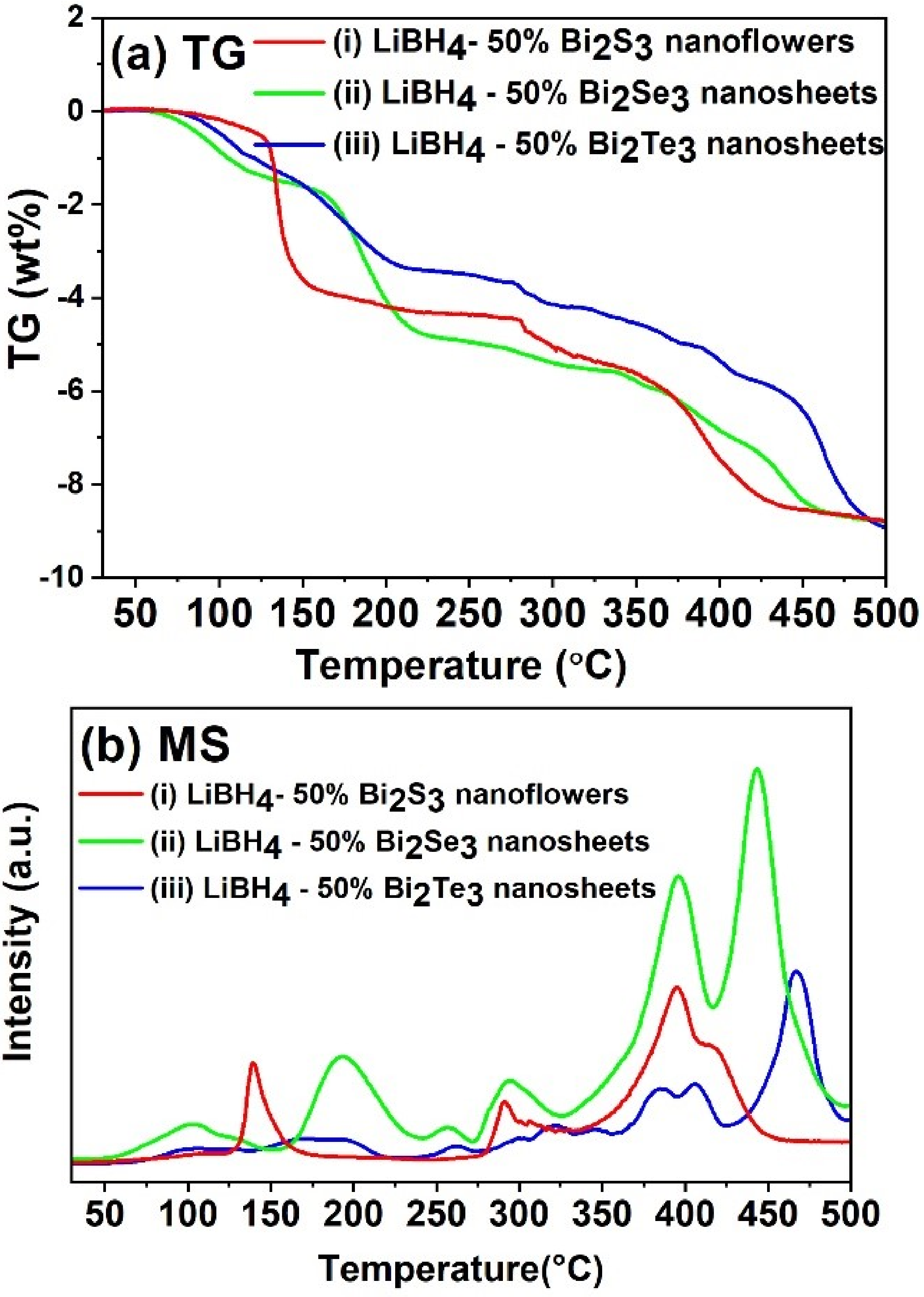

Fig. 5-7: (a) TG and (b) MS profiles of milled samples; (i) $LiBH_4$ – 50 wt% Bi_2S_3 nanoflowers (ii) $LiBH_4$ – 50 wt% Bi_2Se_3 nanosheets (iii) $LiBH_4$ – 50 wt% Bi_2Te_3 nanosheets

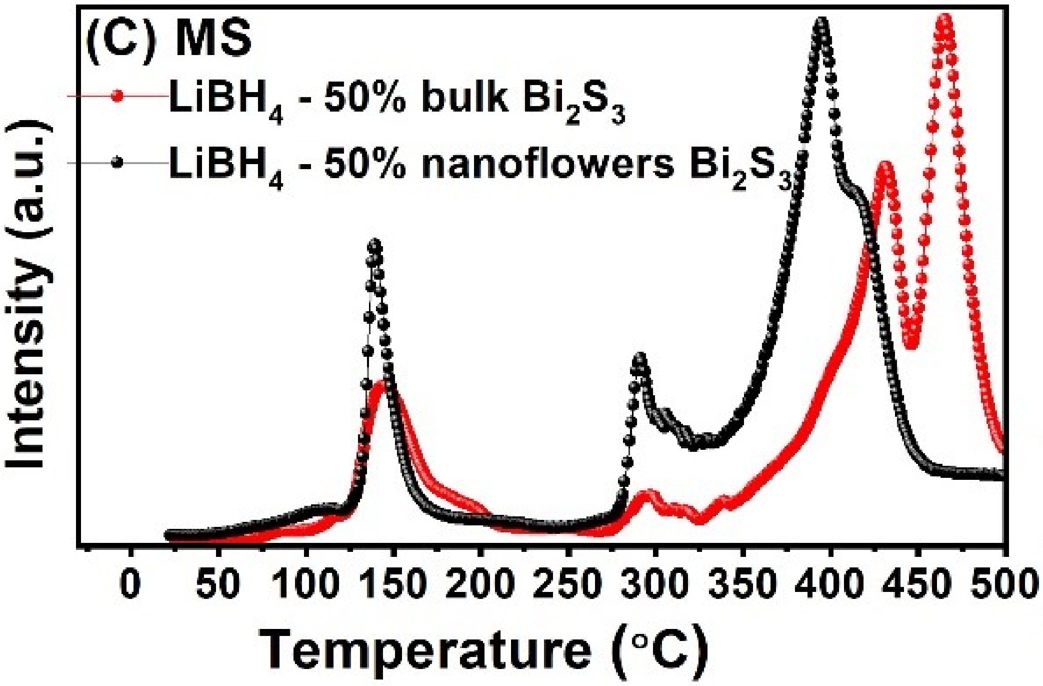

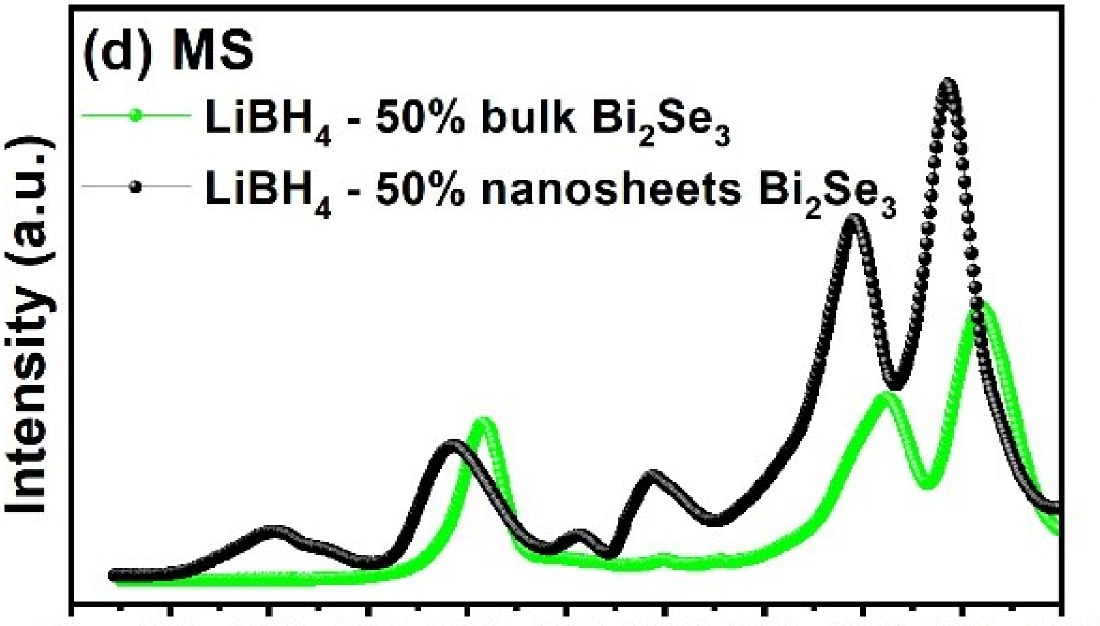

Fig. 5-7: (c) and (d) are MS profile for the comparison of nanostructures and bulk Bi_2S_3 and Bi_2Se_3 samples respectively mixed with $LiBH_4$

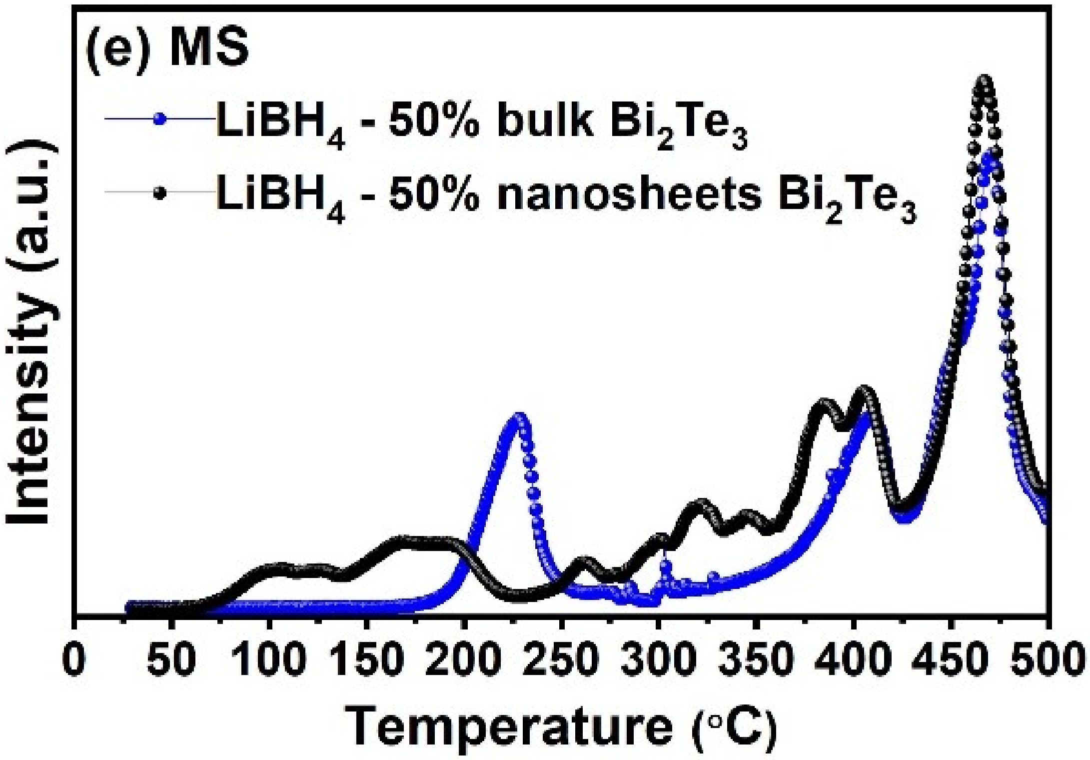

Fig. 5-7: (e) MS profile for the comparison of nanostructures and bulk Bi_2Te_3 mixed with $LiBH_4$

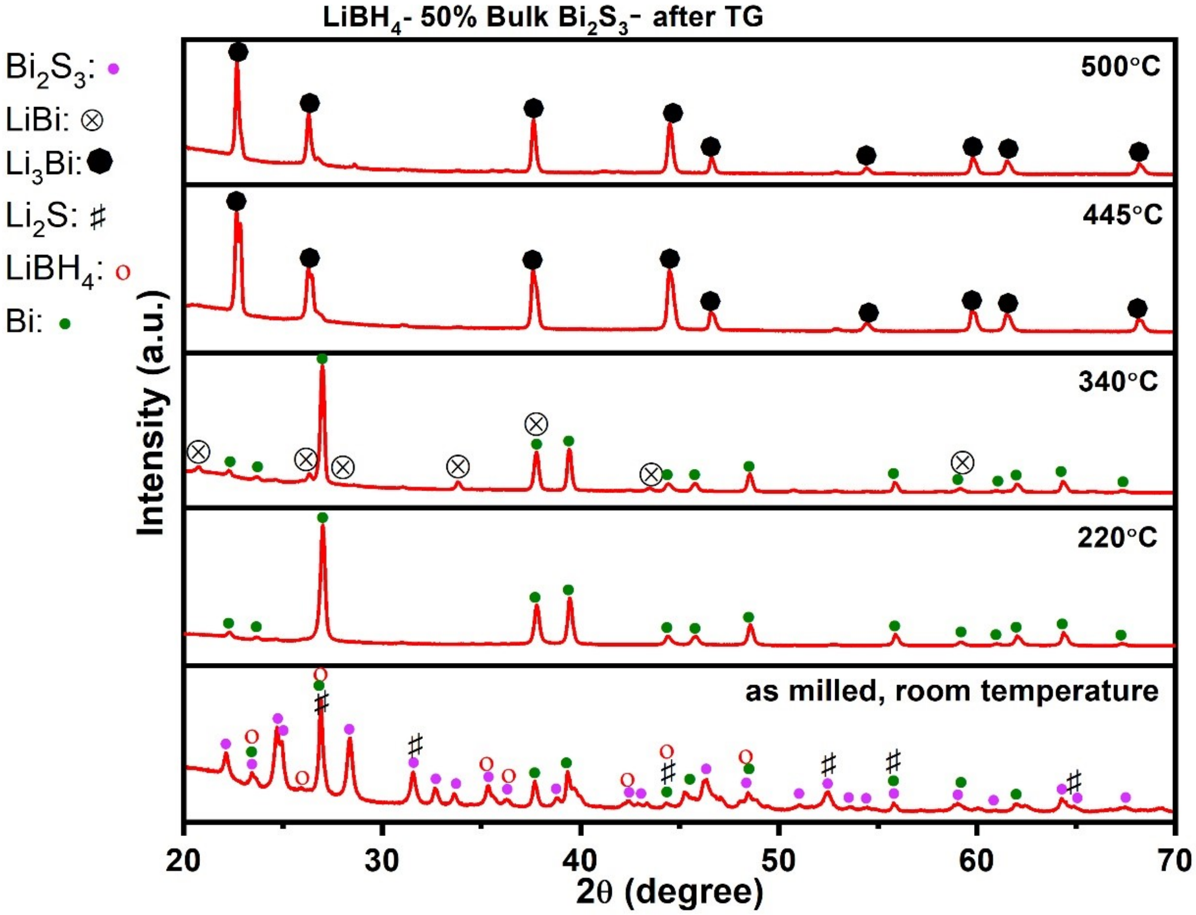

Fig. 5-8: XRD profile of samples after heated to various temperatures with the same heating rate $LiBH_4$ – 50wt% bulk Bi_2S_3

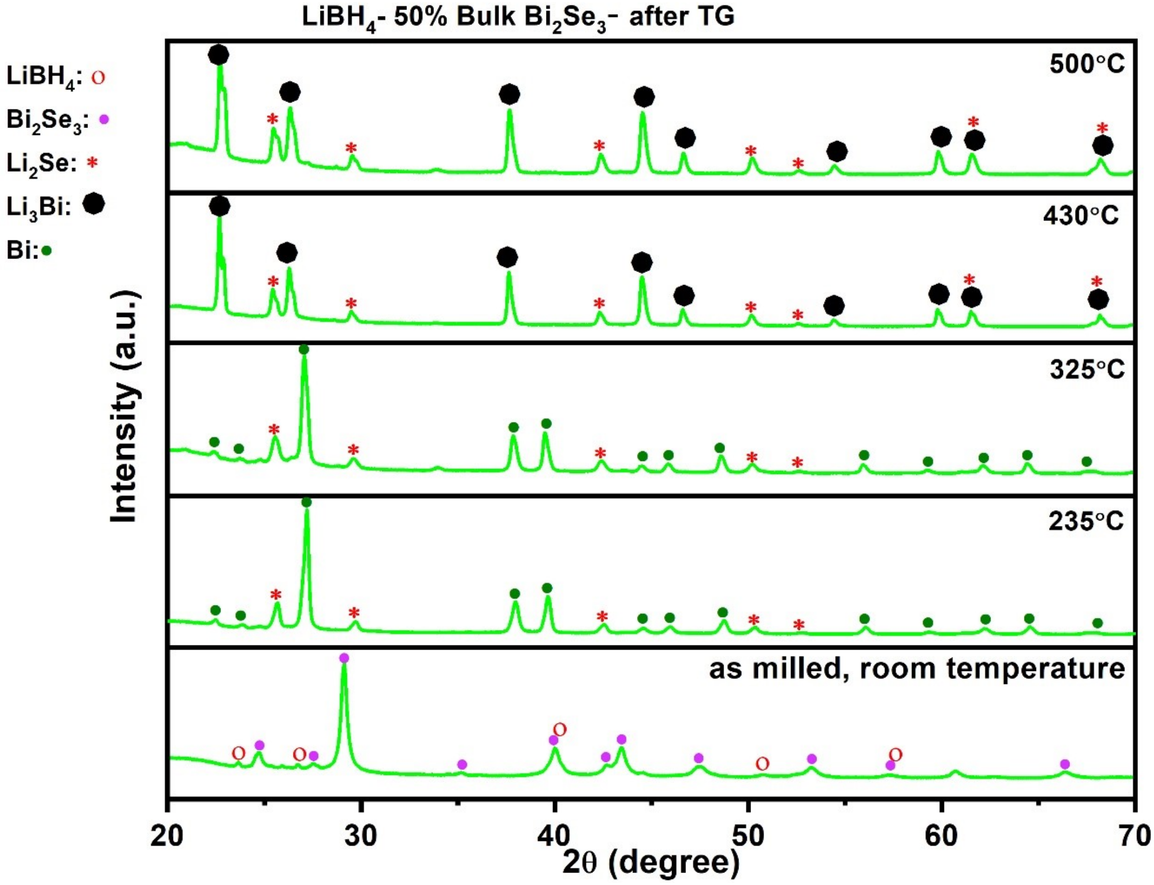

Fig. 5-9: XRD profile of samples after heated to various temperatures with the same heating rate LiBH$_4$ – 50wt% bulk Bi$_2$Se$_3$

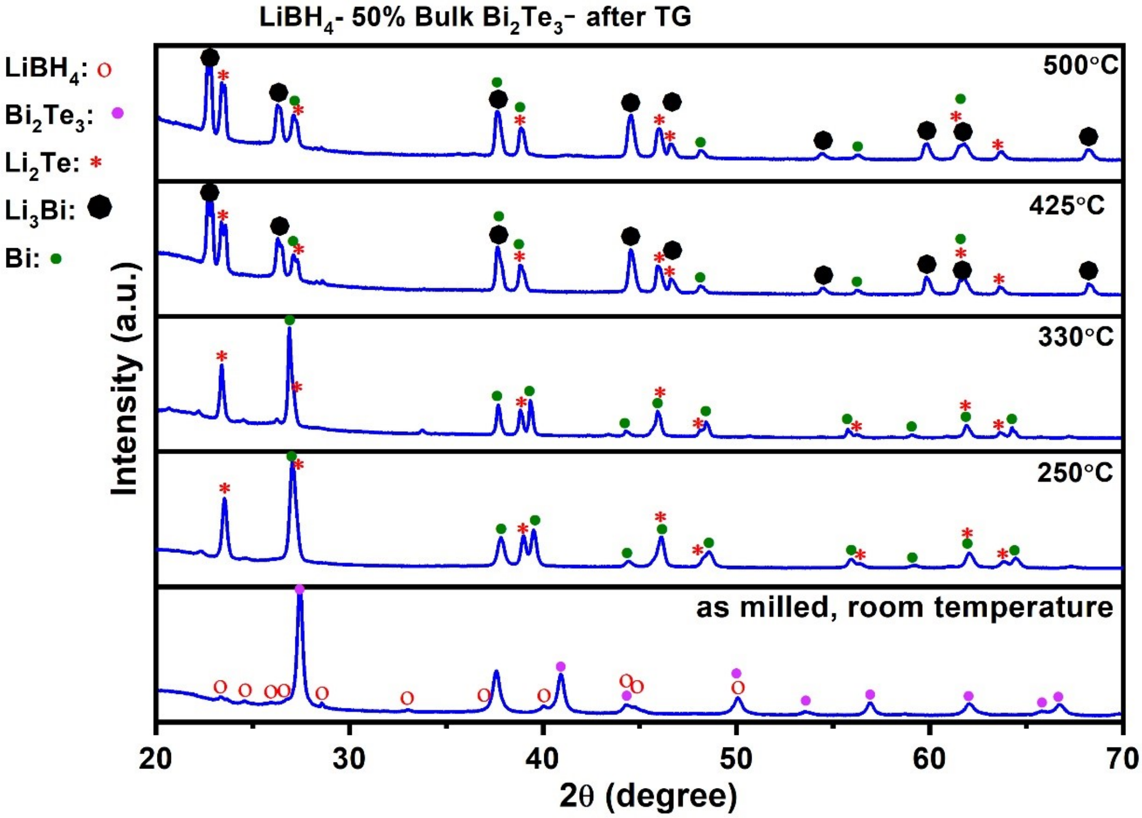

Fig. 5-10: XRD profile of samples after heated to various temperatures with the same heating rate $LiBH_4$-50 wt% bulk Bi_2Te_3

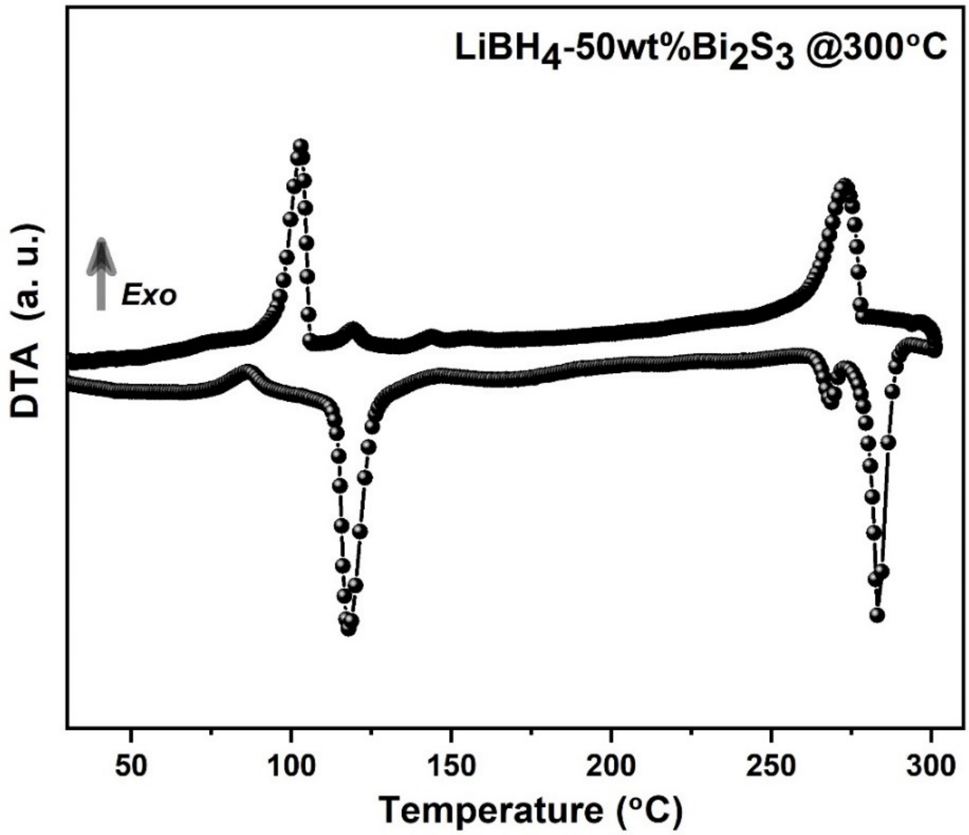

Fig. 5-11: DTA profile of LiBH$_4$-50wt% Bi$_2$S$_3$ composite with heating (downwards; endo) and cooling (upwards; exo) profiles

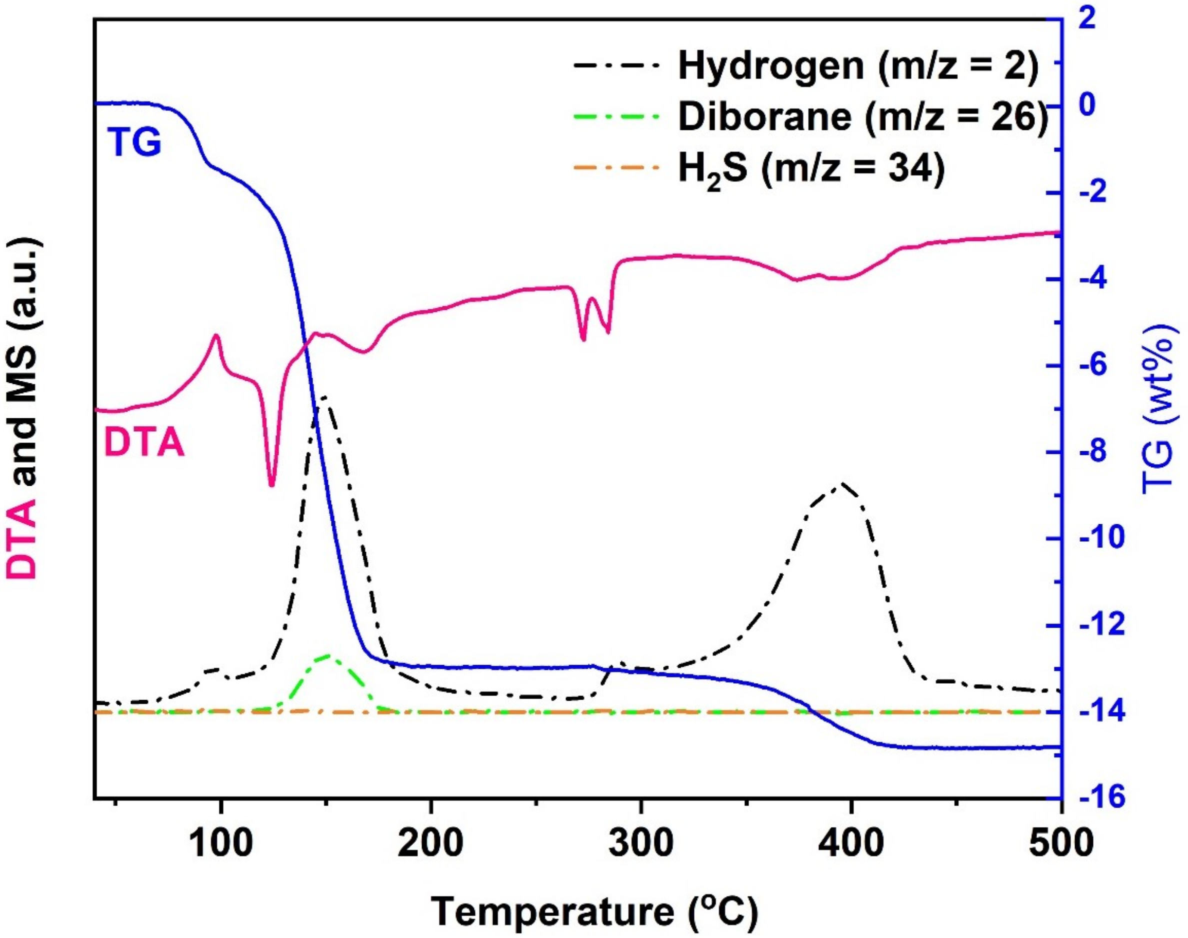

Fig 5-12: TG-DTA and MS profile of $12LiBH_4$- Bi_2S_3 sample

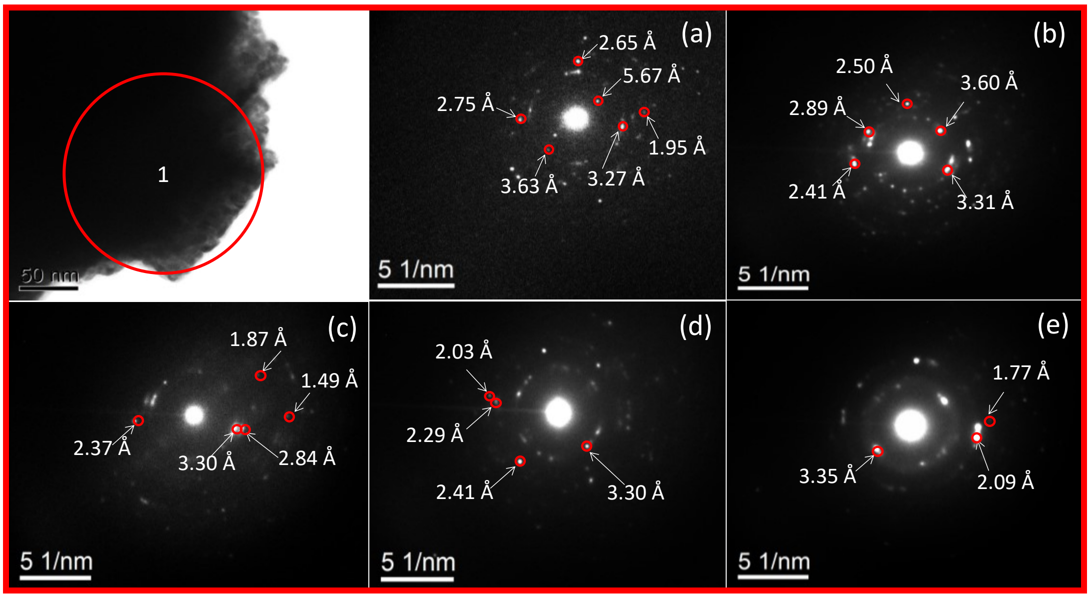

Image indication	Temperature	d-spacing	Phase Identification
(a)	**RT**	**5.67**	**Bi_2S_3**
		3.63	**Bi_2S_3**
		3.27	**Bi**
		2.75	**Bi**
		2.65	**Bi_2S_3**
		1.95	**Bi_2S_3**
(b)	**50°C**	**3.6**	**Bi_2S_3**
		3.31	**Li_2S**
		2.89	**Li_2S**
		2.5	**Bi_2S_3**
		2.41	**LiBi**
(c)	**100°C**	**3.3**	**Li_2S**
		2.84	**Li_2S**
		2.37	**LiBi**
		1.87	**Bi**
		1.49	**Bi**
(d)	**150°C**	**3.3**	**Li_2S**
		2.41	**LiBi**
		2.29	**Bi**
		2.03	**Li_3Bi**
(e)	**200°C**	**3.35**	**Li_3Bi**
		2.09	**LiBi**
		1.77	**LiBi**

Fig. 5-13: TEM images (associated SADP) of $LiBH_4$ - 50% Bi_2S_3 nanostructures (a) after milling at room temperature (b) after heating at 50°C (c) after heating at 100°C (d) after heating at 150°C (e) after heating at 200°C (Image a to image e, measurements are on spot 1)

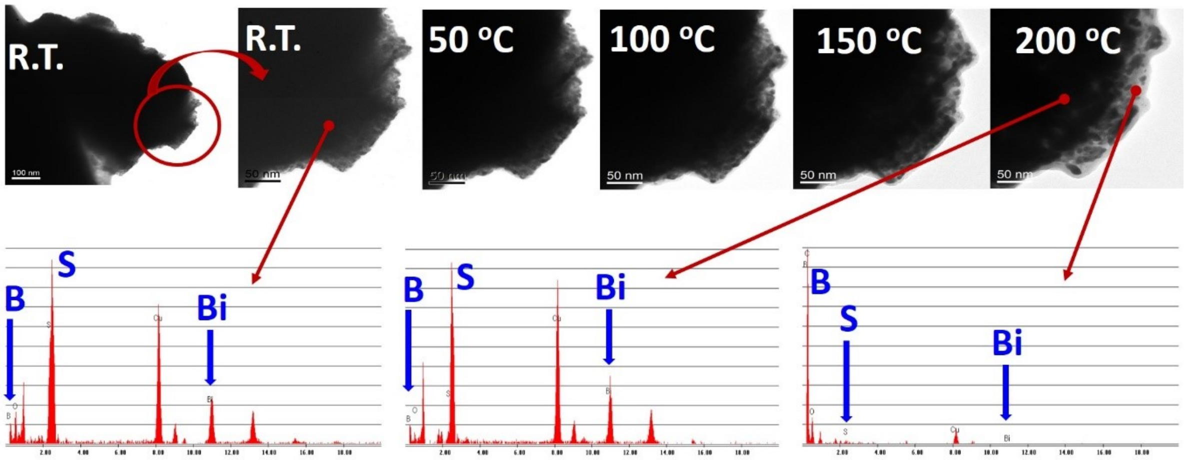

Fig. 5-14: TEM Micrograph of LiBH$_4$-50% Bi$_2$S$_3$ composite after milling and heating at different temperatures. EDS profile was obtained from the position shown by the start point of arrow

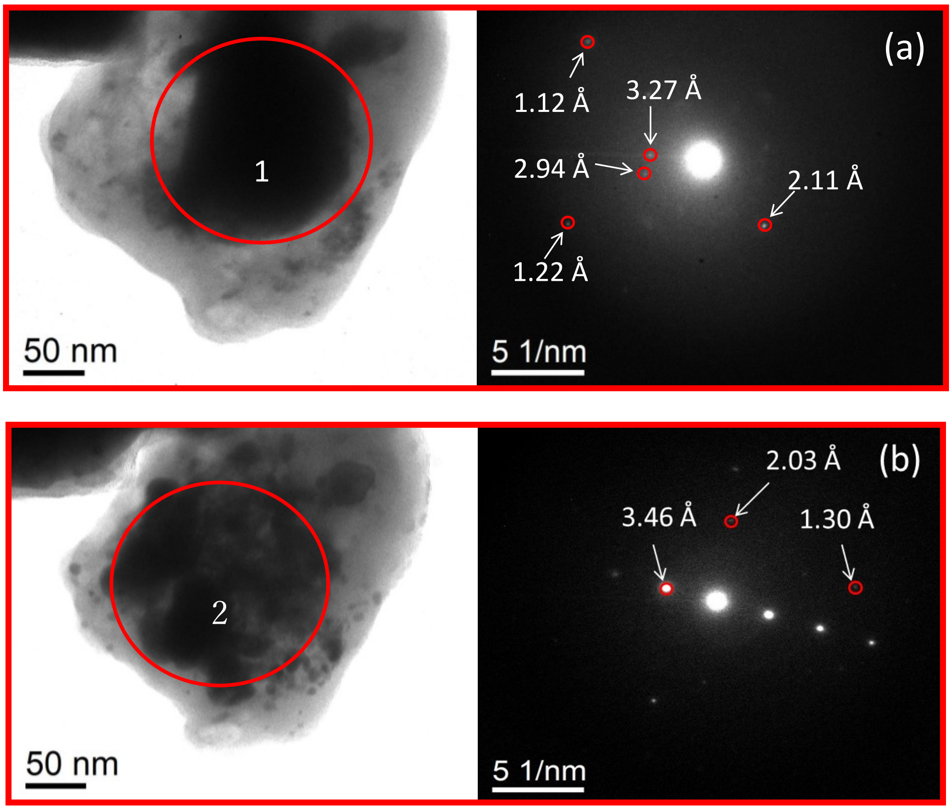

Image indication	Temperature	d-spacing	Phase Identification
(a)	RT	3.27	Bi
		2.94	Bi
		2.11	Li_2Se
		1.22	Li_2Se
		1.12	Bi_2Se_3
(b)	RT after heating	3.46	Li_2Se
		2.03	Li_3Bi
		1.3	LiBi

Fig. 5-15: TEM images (associated SADP) of (a) $LiBH_4$ - 50% Bi_2Se_3 nanostructures at room temperature on spot 1 (b) $LiBH_4$ - 50% Bi_2Se_3 nanostructures at room temperature after heating on spot 2

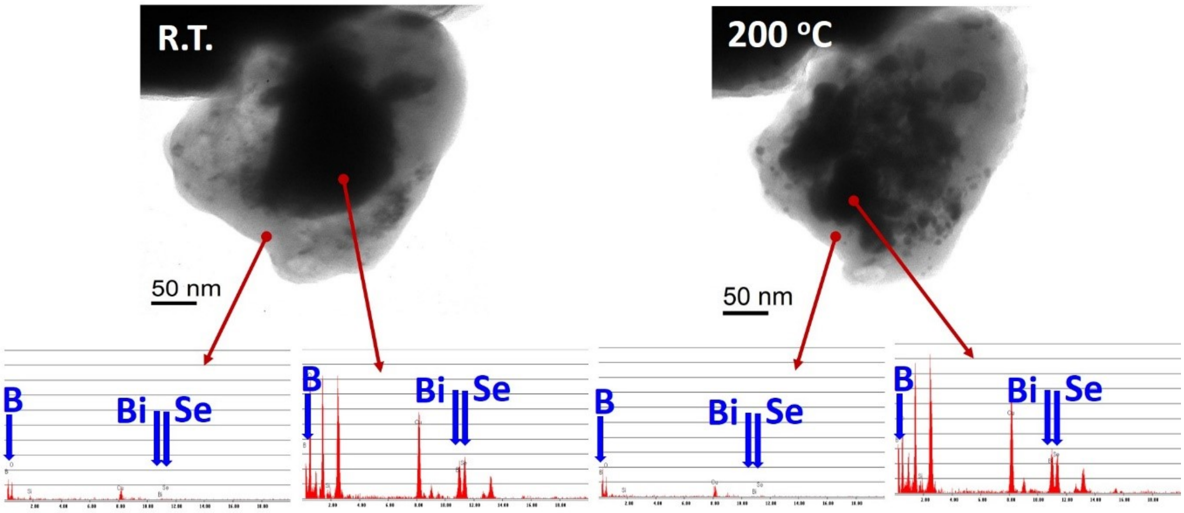

Fig. 5-16: TEM Micrograph of LiBH$_4$-50% Bi$_2$Se$_3$ composite after milling and heating at 450^{o}C. EDS profile was obtained from the position shown by the start point of arrow

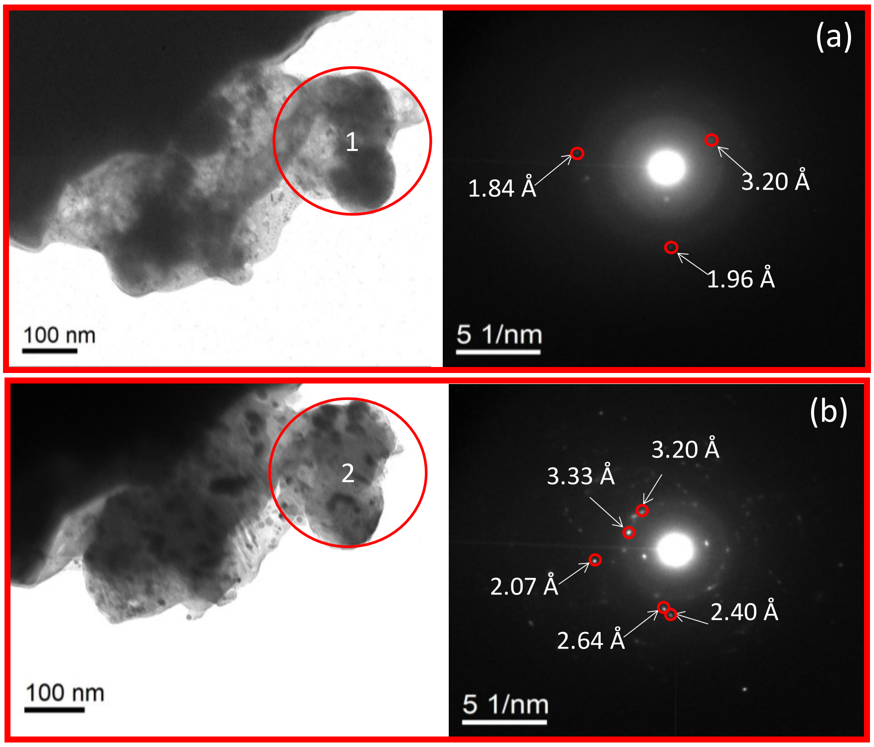

Image indication	**Temperature**	**d-spacing**	**Phase Identification**
(a)	**RT**	**3.2**	**Li_2Te**
		1.96	**Li_2Te**
		1.84	**Bi_2Te_3**
(b)	**RT after heating**	**3.33**	**Li_3Bi**
		3.2	**Li_2Te**
		2.64	**LiBi**
		2.4	**Li_3Bi**
		2.07	**LiBi**

Fig. 5-17: TEM images (associated SADP) of (a) $LiBH_4$ - 50% Bi_2Te_3 nanostructures at room temperature on spot 1 (b) $LiBH_4$ - 50% Bi_2Te_3 nanostructures at room temperature after heating on spot 2

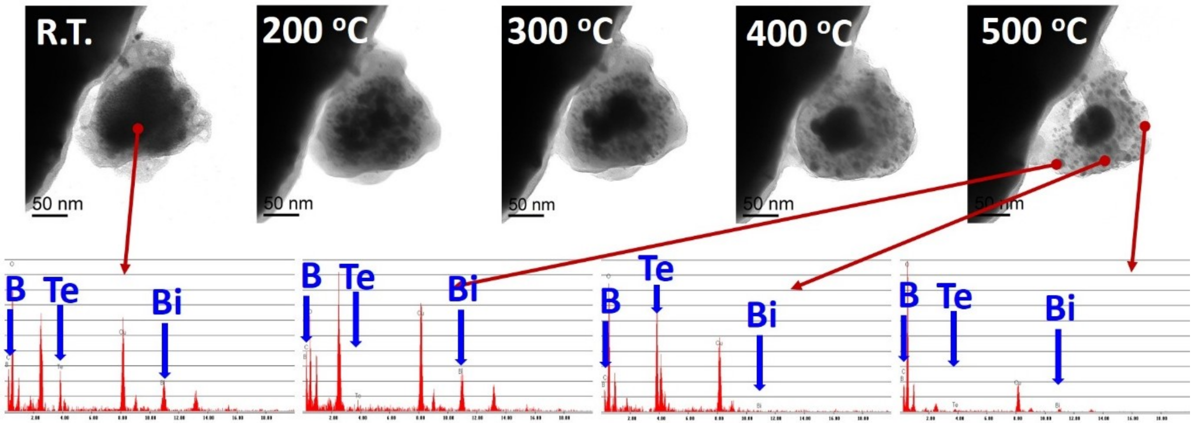

Fig. 5-18: TEM Micrograph of $LiBH_4$-50% Bi_2Te_3 composite after milling and heating at different temperatures. EDS profile was obtained from the position shown by the start point of arrow

Chapter-6

Conclusions and Future work

In this thesis, the thermodynamic and kinetic tuning of $LiBH_4$ and its composite with MgH_2 was achieved by using additives.

The addition of KH to well-known $2LiBH_4$-MgH_2 reduced the decomposition temperature of 1st step reaction, however, no significant effect could be observed for the 2nd major step of decomposition. An interesting phenomenon of eutectic melting through the formation of KBH_4 as an intermediate was observed and a phase diagram was reported herein. The eutectic composition for $x(2LiBH_4\text{-}MgH_2)$ - $(1-x)KH$ was assured to be $x\sim 0.45$ using the combination of differential scanning calorimetry and X-ray diffraction. The eutectic composition was found to melt at ~79°C (T_{min}) which is the lowest melting temperature reported for a complex borohydride-hydride mixture so far. This work suggests the new possibilities to develop more complex hydride/borohydride systems to improve kinetic issues associated with the hydrogen storage applications. Advancement in techniques to decrease the decomposition temperature for on-board applications, while maintaining high hydrogen capacity will be the future road map.

As a second part of this thesis, a thermodynamic alteration of $LiBH_4$ was achieved by the addition of Bi based chalcogenide materials. A systematic study for the decomposition of $LiBH_4$ at low temperature using Bi_2X_3 was performed, which is quite useful not only for the hydrogen storage purpose but also for Li-ion battery application. The formation of Li_2X and Li_3Bi was the thermodynamic driving force for this destabilization. The onset desorption temperature of $LiBH_4$ was thermodynamically lowered down to 75°C by the addition of bulk

Bi_2S_3. A further reduction in the onset temperature could be achieved by the use of Bi_2S_3 nanoflowers due to kinetic enhancement. However, the formation of H_2S during this reaction was crucial in case of Bi_2S_3 addition which caused the loss of sulphur and thus the loss of reversibility. From this point of view, the addition of Bi_2Se_3 nanostructure was found more beneficial which allow the H_2 evolution only (no other gaseous species e.g. B_2H_6) that can be helpful to maintain the reversibility of $LiBH_4$. The reversibility of these system will be investigated in the future work. The establishment of reaction mechanism also enabled us to understand the electrochemical operation of these composites. It is concluded that the high capacity, observed in charging process in our previous work [62],[63] must be due to the thermochemical reaction between $LiBH_4$ and Bi_2X_3 at 120°C (speculated in previous work), which generated the cracks in electrode material and resulted in the capacity decay during within few cycles. This finding directed us to design the composite system in such a way that it can be operated at room temperature to avoid the thermochemical reaction between electrode material and electrolyte.

References

[1] World Energy Consumption Statistics | Enerdata n.d. https://yearbook.enerdata.net/total-energy/world-consumption-statistics.html (accessed June 29, 2020).

[2] EIA projects nearly 50% increase in world energy usage by 2050, led by growth in Asia - Today in Energy - U.S. Energy Information Administration (EIA) n.d. https://www.eia.gov/todayinenergy/detail.php?id=42342 (accessed June 29, 2020).

[3] Jochem E. Reducing CO2 emissions - the West German plan. Energy Policy 1991;19:119–26. doi:10.1016/0301-4215(91)90127-A.

[4] Züttel A. Hydrogen storage methods. Naturwissenschaften 2004;91:157–72. doi:10.1007/s00114-004-0516-x.

[5] Hydropole | The Swiss Hydrogen Association n.d. https://hydropole.ch/en/ (accessed June 23, 2020).

[6] Züttel A, Borgschulte A, Schlapbach L, Chorkendorff I, Suda S. Properties of Hydrogen. Hydrog as a Futur Energy Carr 2008:71–147. doi:doi:10.1002/9783527622894.ch4.

[7] Fukai Y. The Metal-Hydrogen System Basic Bulk Properties. vol. 21. 2005. doi:10.1007/978-3-662-02801-8_1.

[8] Colozza AJ. Hydrogen Storage for Aircraft. 2002.

[9] Züttel A. Materials for hydrogen storage. Mater Today 2003;6:24–33. doi:https://doi.org/10.1016/S1369-7021(03)00922-2.

[10] Schlapbach L, Züttel A. Hydrogen-storage materials for mobile applications. Nature

2001;414:353–8. doi:10.1038/35104634.

[11] Krishna R, Titus E, Salimian M, Okhay O, Rajendran S, Rajkumar A, et al. Hydrogen Storage for Energy Application, 2020. doi:10.5772/51238.

[12] Kurtz J, Ainscough C, Simpson L, Caton M. Hydrogen Storage Needs for Early Motive Fuel Cell Markets 2012:85.

[13] Chen P, Zhu M. Recent progress in hydrogen storage. Mater Today 2008;11:36–43. doi:https://doi.org/10.1016/S1369-7021(08)70251-7.

[14] Andersson J, Grönkvist S. Large-scale storage of hydrogen. Int J Hydrogen Energy 2019;44:11901–19. doi:https://doi.org/10.1016/j.ijhydene.2019.03.063.

[15] Rivard E, Trudeau M, Zaghib K. Hydrogen Storage for Mobility: A Review. Mater 2019;12. doi:10.3390/ma12121973.

[16] Stolten D, Emonts B. Handbook of Hydrogen Storage Efficient Carbon Capture for Coal Power Plants Transition to Renewable Energy Systems Hydrogen Storage Technologies Hydrogen and Fuel Cells. 2016.

[17] Krasae-in S, Stang JH, Neksa P. Development of large-scale hydrogen liquefaction processes from 1898 to 2009. Int J Hydrogen Energy 2010;35:4524–33. doi:https://doi.org/10.1016/j.ijhydene.2010.02.109.

[18] Tamura H. 済無 No Title No Title. J Chem Inf Model 2008;53:287. doi:10.1017/CBO9781107415324.004.

[19] Gkanas EI, Khzouz M. Metal Hydride Hydrogen Compression Systems – Materials, Applications and Numerical Analysis. Hydrog Storage Technol 2018:1–37. doi:doi:10.1002/9781119460572.ch1.

[20] Griessen R, Giebels IAME, Dam B. Hydrogen as a Future Energy Carrier. Weinheim, Germany: Wiley; 2008. doi:10.1002/9783527622894.

[21] Pukazhselvan D, Kumar V, Singh SK. High capacity hydrogen storage: Basic aspects, new developments and milestones. Nano Energy 2012;1:566–89. doi:https://doi.org/10.1016/j.nanoen.2012.05.004.

[22] Züttel A. Hydrogen Storage Materials (Solid) for Fuel Cell Vehicles BT - Encyclopedia of Applied Electrochemistry. In: Kreysa G, Ota K, Savinell RF, editors., New York, NY: Springer New York; 2014, p. 1049–66. doi:10.1007/978-1-4419-6996-5_199.

[23] Bérubé V, Radtke G, Dresselhaus M, Chen G. Size effects on the hydrogen storage properties of nanostructured metal hydrides: A review. Int J Energy Res 2007. doi:10.1002/er.1284.

[24] Song L, Wang S, Jiao C, Si X, Li Z, Liu S, et al. Thermodynamics study of hydrogen storage materials. J Chem Thermodyn 2012;46:86–93. doi:https://doi.org/10.1016/j.jct.2011.06.022.

[25] Jain A, Agarwal S, Ichikawa T. Catalytic Tuning of Sorption Kinetics of Lightweight Hydrides: A Review of the Materials and Mechanism. Catal 2018;8. doi:10.3390/catal8120651.

[26] Jain A, Miyaoka H, Ichikawa T. Destabilization of lithium hydride by the substitution of group 14 elements: A review. Int J Hydrogen Energy 2016;41:5969–78. doi:http://dx.doi.org/10.1016/j.ijhydene.2016.02.069.

[27] Li H-W, Orimo S, Nakamori Y, Miwa K, Ohba N, Towata S, et al. Materials designing

of metal borohydrides: Viewpoints from thermodynamical stabilities. J Alloys Compd 2007;446–447:315–8. doi:https://doi.org/10.1016/j.jallcom.2007.02.156.

[28] Li G, Matsuo M, Takagi S, Chaudhary A-L, Sato T, Dornheim M, et al. Thermodynamic Properties and Reversible Hydrogenation of LiBH4–Mg2FeH6 Composite Materials. Inorganics 2017;5. doi:10.3390/inorganics5040081.

[29] Wang J, Liu T, Wu G, Li W, Liu Y, Araújo CM, et al. Potassium-modified Mg(NH2)2/2 LiH system for hydrogen storage. Angew Chem Int Ed Engl 2009;48:5828–32. doi:10.1002/anie.200805264.

[30] Teng YL, Ichikawa T, Miyaoka H, Kojima Y. Improvement of hydrogen desorption kinetics in the LiH-NH3 system by addition of KH. Chem Commun 2011;47:12227–9. doi:10.1039/c1cc15523g.

[31] Durojaiye T, Goudy A. Desorption kinetics of lithium amide/magnesium hydride systems at constant pressure thermodynamic driving forces. Int J Hydrogen Energy 2012;37:3298–304. doi:https://doi.org/10.1016/j.ijhydene.2011.11.071.

[32] Dong B-X, Wang L, Ge J, Ping C, Teng Y-L, Li Z-W. The effect of KH on enhancing the dehydrogenation properties of the Li-N-H system and its catalytic mechanism. Phys Chem Chem Phys 2018;20:11116–22. doi:10.1039/c8cp00470f.

[33] Walker G. Hydrogen storage technologies. Solid-State Hydrog Storage Mater Chem 2008:3–17. doi:10.1533/9781845694944.1.3.

[34] Department of Energy n.d. https://www.energy.gov/ (accessed June 21, 2020).

[35] Sakintuna B, Lamari-Darkrim F, Hirscher M. Metal hydride materials for solid hydrogen storage: A review. Int J Hydrogen Energy 2007;32:1121–40.

doi:https://doi.org/10.1016/j.ijhydene.2006.11.022.

[36] Jain IP, Lal C, Jain A. Hydrogen storage in Mg: A most promising material. Int J Hydrogen Energy 2010;35:5133–44. doi:https://doi.org/10.1016/j.ijhydene.2009.08.088.

[37] Goto K, Hirata T, Yamamoto I, Nakao W. Suitability Evaluation of LaNi5 as Hydrogen-Storage-Alloy Actuator by In-Situ Displacement Measurement during Hydrogen Pressure Change. Mol 2019;24. doi:10.3390/molecules24132420.

[38] Briki C, de Rango P, Belkhiria S, Dhaou MH, Jemni A. Measurements of expansion of LaNi5 compacted powder during hydrogen absorption/desorption cycles and their influences on the reactor wall. Int J Hydrogen Energy 2019;44:13647–54. doi:https://doi.org/10.1016/j.ijhydene.2019.04.010.

[39] Rusman NAA, Dahari M. A review on the current progress of metal hydrides material for solid-state hydrogen storage applications. Int J Hydrogen Energy 2016;41:12108–26. doi:https://doi.org/10.1016/j.ijhydene.2016.05.244.

[40] Ding Z, Li S, Zhou Y, Chen Z, Yang W, Ma W, et al. LiBH4 for hydrogen storage - New perspectives. Nano Mater Sci 2020;2:109–19. doi:https://doi.org/10.1016/j.nanoms.2019.09.003.

[41] Puszkiel J, Gasnier A, Amica G, Gennari F. Tuning LiBH4 for Hydrogen Storage: Destabilization, Additive, and Nanoconfinement Approaches. Mol 2020;25. doi:10.3390/molecules25010163.

[42] Prachi P, Wagh MM, Aneesh G. A Review on Solid State Hydrogen Storage Material. Adv Energy Power 2016. doi:10.13189/aep.2016.040202.

[43] Reilly JJ, Wiswall RH. Reaction of hydrogen with alloys of magnesium and nickel and the formation of Mg2NiH4. Inorg Chem 1968;7:2254–6. doi:10.1021/ic50069a016.

[44] Chen P, Xiong Z, Luo J, Lin J, Tan KL. Interaction of hydrogen with metal nitrides and imides. Nature 2002;420:302–4. doi:10.1038/nature01210.

[45] Ichikawa T, Hanada N, Isobe S, Leng H, Fujii H. Mechanism of Novel Reaction from LiNH2 and LiH to Li2NH and H2 as a Promising Hydrogen Storage System. J Phys Chem B 2004;108:7887–92. doi:10.1021/jp049968y.

[46] Barkhordarian G, Klassen T, Dornheim M, Bormann R. Unexpected kinetic effect of MgB2 in reactive hydride composites containing complex borohydrides. J Alloys Compd 2007;440:L18–21. doi:https://doi.org/10.1016/j.jallcom.2006.09.048.

[47] Vajo JJ, Li W, Liu P. Thermodynamic and kinetic destabilization in LiBH4/Mg2NiH4: promise for borohydride-based hydrogen storage. Chem Commun 2010;46:6687–9. doi:10.1039/C0CC01026J.

[48] Vajo JJ, Skeith SL, Mertens F. Reversible Storage of Hydrogen in Destabilized LiBH4. J Phys Chem B 2005;109:3719–22. doi:10.1021/jp040769o.

[49] Bösenberg U, Doppiu S, Mosegaard L, Barkhordarian G, Eigen N, Borgschulte A, et al. Hydrogen sorption properties of MgH2–LiBH4 composites. Acta Mater 2007;55:3951–8. doi:https://doi.org/10.1016/j.actamat.2007.03.010.

[50] Pinkerton FE, Meyer MS, Meisner GP, Balogh MP, Vajo JJ. Phase Boundaries and Reversibility of LiBH4/MgH2 Hydrogen Storage Material. J Phys Chem C 2007;111:12881–5. doi:10.1021/jp0742867.

[51] Nakagawa T, Ichikawa T, Hanada N, Kojima Y, Fujii H. Thermal analysis on the

Li–Mg–B–H systems. J Alloys Compd 2007;446–447:306–9. doi:https://doi.org/10.1016/j.jallcom.2007.02.097.

[52] Matsuo M, Nakamori Y, Orimo SI, Maekawa H, Takamura H. Lithium superionic conduction in lithium borohydride accompanied by structural transition. Appl Phys Lett 2007;91:224103. doi:10.1063/1.2817934.

[53] Takahashi K, Hattori K, Yamazaki T, Takada K, Matsuo M, Orimo S, et al. All-solid-state lithium battery with LiBH4 solid electrolyte. J Power Sources 2013;226:61–4. doi:https://doi.org/10.1016/j.jpowsour.2012.10.079.

[54] Blanchard D, Nale A, Sveinbjörnsson D, Eggenhuisen TM, Verkuijlen MHW, Suwarno, et al. Nanoconfined LiBH4 as a fast lithium ion conductor. Adv Funct Mater 2015;25:184–92. doi:10.1002/adfm.201402538.

[55] Unemoto A, Yasaku S, Nogami G, Tazawa M, Taniguchi M, Matsuo M, et al. Development of bulk-type all-solid-state lithium-sulfur battery using LiBH4 electrolyte. Appl Phys Lett 2014;105. doi:10.1063/1.4893666.

[56] Lu F, Pang Y, Zhu M, Han F, Yang J, Fang F, et al. A High-Performance Li–B–H Electrolyte for All-Solid-State Li Batteries. Adv Funct Mater 2019;29:1809219. doi:10.1002/adfm.201809219.

[57] Singh R, Kumari P, Rathore RK, Shinzato K, Ichikawa T, Verma AS, et al. LiBH4 as solid electrolyte for Li-ion batteries with Bi2Te3 nanostructured anode. Int J Hydrogen Energy 2018;43:21709–14. doi:https://doi.org/10.1016/j.ijhydene.2018.03.068.

[58] Kumari P, Pal P, Shinzato K, Awasthi K, Ichikawa T, Jain A, et al. Nanostructured Bi2Te3 as anode material as well as a destabilizing agent for LiBH4. Int J Hydrogen

Energy 2019. doi:https://doi.org/10.1016/j.ijhydene.2019.06.175.

[59] Dornheim M. Thermodynamics of Metal Hydrides: Tailoring Reaction Enthalpies of Hydrogen Storage Materials. Thermodyn. - Interact. Stud. - Solids, Liq. Gases, InTech; 2011. doi:10.5772/21662.

[60] Li J, Li B, Shao H, Li W, Lin H. Catalysis and Downsizing in Mg-Based Hydrogen Storage Materials. Catalysts 2018;8:89. doi:10.3390/catal8020089.

[61] Zeng L, Miyaoka H, Ichikawa T, Kojima Y. Superior hydrogen exchange effect in the MgH2-LiBH4 system. J Phys Chem C 2010. doi:10.1021/jp1042443.

[62] Kumari P, Singh R, Awasthi K, Ichikawa T, Kumar M, Jain A. Highly stable nanostructured Bi2Se3 anode material for all solid-state lithium-ion batteries. J Alloys Compd 2020. doi:10.1016/j.jallcom.2020.155403.

[63] Kumari P, Awasthi K, Agarwal S, Ichikawa T, Kumar M, Jain A. Flower-like Bi2S3 nanostructures as highly efficient anodes for all-solid-state lithium-ion batteries. RSC Adv 2019. doi:10.1039/c9ra05055h.

[64] X-ray Powder Diffraction (XRD) n.d. https://serc.carleton.edu/research_education/geochemsheets/techniques/XRD.html (accessed June 23, 2020).

[65] B. D. CULLITY. X-Ray Diffraction Addison-Wesley Metallurgy Series. J Chem Inf Model 1956;53:1689–99. doi:10.1017/CBO9781107415324.004.

[66] Wagner M, Wagner M. Thermal Analysis in Practice. Therm. Anal. Pract., 2017. doi:10.3139/9781569906446.fm.

[67] Dorset DL. Transmission electron microscopy and diffractometry of materials. By B.

Fultz and J. M. Howe. pp. xix + 748pp. Heidelberg: Springer-Verlag, 2001. Price DM 179.00, US $89.95. ISBN 3-540-67841-7. . J Appl Crystallogr 2002. doi:10.1107/s0021889801020532.

[68] Yao H, Isobe S, Wang Y, Hashimoto N, Ohnuki S. Plastic bag method for active sample loading into transmission electron microscope. J Electron Microsc (Tokyo) 2011. doi:10.1093/jmicro/dfr072.

[69] How to Mix Backscattered and Secondary Electron Images n.d. https://www.azom.com/article.aspx?ArticleID=16390 (accessed June 24, 2020).

[70] Electron Interactions n.d. https://serc.carleton.edu/research_education/geochemsheets/electroninteractions.html (accessed June 24, 2020).

[71] Paskevicius M, Ley MB, Sheppard DA, Jensen TR, Buckley CE. Eutectic melting in metal borohydrides. Phys Chem Chem Phys 2013;15:19774–89. doi:10.1039/c3cp53920b.

[72] Roedern E, Hansen BRS, Ley MB, Jensen TR. Effect of Eutectic Melting, Reactive Hydride Composites, and Nanoconfinement on Decomposition and Reversibility of LiBH4-KBH4. J Phys Chem C 2015. doi:10.1021/acs.jpcc.5b09228.

[73] Zavorotynska O, Deledda S, Li G, Matsuo M, Orimo SI, Hauback BC. Isotopic Exchange in Porous and Dense Magnesium Borohydride. Angew Chemie - Int Ed 2015. doi:10.1002/anie.201502699.

[74] Ley MB, Roedern E, Jensen TR. Eutectic melting of LiBH4-KBH4. Phys Chem Chem Phys 2014. doi:10.1039/c4cp03207a.

[75] Lee JY, Ravnsbæk D, Lee YS, Kim Y, Cerenius Y, Shim JH, et al. Decomposition reactions and reversibility of the LiBH4-Ca (BH4)2 composite. J Phys Chem C 2009;113:15080–6. doi:10.1021/jp904400b.

[76] Bardají EG, Zhao-Karger Z, Boucharat N, Nale A, Van Setten MJ, Lohstroh W, et al. LiBH4?Mg(BH4)2: A physical mixture of metal borohydrides as hydrogen storage material. J Phys Chem C 2011;115:6095–101. doi:10.1021/jp110518s.

[77] Liu R, Book D. Mn-based borohydride synthesized by ball-milling KBH4 and MnCl2 for hydrogen storage. Int J Hydrogen Energy 2014;39:2194–200. doi:10.1016/j.ijhydene.2013.11.125.

[78] Journal of Research of the National Bureau of Standards - United States. National Bureau of Standards - Google Books n.d. https://books.google.co.jp/books?hl=en&lr=&id=dRvWAAAAMAAJ&oi=fnd&pg=PA117&ots=B2abENN3Sv&sig=rtzhwSGCEiOObEuci6YiEMUnKFY&redir_esc=y#v=onepage&q&f=false (accessed June 24, 2020).

[79] Zaluska A, Zaluski L, Ström-Olsen JO. Nanocrystalline magnesium for hydrogen storage. J Alloys Compd 1999. doi:10.1016/S0925-8388(99)00073-0.

[80] Callini E, Aguey-Zinsou KF, Ahuja R, Ares JR, Bals S, Biliškov N, et al. Nanostructured materials for solid-state hydrogen storage: A review of the achievement of COST Action MP1103. Int J Hydrogen Energy 2016. doi:10.1016/j.ijhydene.2016.04.025.

[81] Niemann MU, Srinivasan SS, Phani AR, Kumar A, Goswami DY, Stefanakos EK. Nanomaterials for hydrogen storage applications: A review. J Nanomater 2008.

doi:10.1155/2008/950967.

[82] Schneemann A, White JL, Kang S, Jeong S, Wan LF, Cho ES, et al. Nanostructured Metal Hydrides for Hydrogen Storage. Chem Rev 2018. doi:10.1021/acs.chemrev.8b00313.

[83] Ni J, Bi X, Jiang Y, Li L, Lu J. Bismuth chalcogenide compounds Bi2×3 (X=O, S, Se): Applications in electrochemical energy storage. Nano Energy 2017. doi:10.1016/j.nanoen.2017.02.041.

[84] Arabzadeh A, Salimi A. Facile Synthesis of Ultra-wide Two Dimensional Bi $_2$ S $_3$ Nanosheets: Characterizations, Properties and Applications in Hydrogen Peroxide Sensing and Hydrogen Storage. Electroanalysis 2017;29:2027–35. doi:10.1002/elan.201600808.

[85] Mamur H, Bhuiyan MRA, Korkmaz F, Nil M. A review on bismuth telluride (Bi2Te3) nanostructure for thermoelectric applications. Renew Sustain Energy Rev 2018;82:4159–69. doi:10.1016/j.rser.2017.10.112.

[86] Yan Y, Remhof A, Hwang SJ, Li HW, Mauron P, Orimo SI, et al. Pressure and temperature dependence of the decomposition pathway of LiBH 4. Phys Chem Chem Phys 2012;14:6514–9. doi:10.1039/c2cp40131b.

[87] AN S. The Reaction Mechanisms of H2S Decomposition into Hydrogen and Sulfur: Application of Classical and Biological Thermodynamics. J Thermodyn Catal 2017. doi:10.4172/2157-7544.1000186.

[88] Startsev AN, Kruglyakova O V., Chesalov YA, Ruzankin SP, Kravtsov EA, Larina T V., et al. Low temperature catalytic decomposition of hydrogen sulfide into hydrogen

and diatomic gaseous sulfur. Top. Catal., 2013. doi:10.1007/s11244-013-0061-y.

[89] Startsev AN. Diatomic sulfur: a mysterious molecule. J Sulfur Chem 2019. doi:10.1080/17415993.2019.1588273.

[90] Maekawa H, Matsuo M, Takamura H, Ando M, Noda Y, Karahashi T, et al. Halide-stabilized LiBH4, a room-temperature lithium fast-ion conductor. J Am Chem Soc 2009;131:894–5. doi:10.1021/ja807392k.